

Measurement of the *D*-line vector polarizability in ^{87}Rb using tune-out wavelength spectroscopy

Adam James Fallon

Tulsa, Oklahoma

B.S., University of Oklahoma, 2012

B.A., University of Oklahoma, 2012

A Dissertation presented to the Graduate Faculty
of the University of Virginia in Candidacy for the Degree of
Doctor of Philosophy

Department of Physics

UNIVERSITY OF VIRGINIA

June 2020

Abstract

Doctor of Philosophy

Department of Physics
UNIVERSITY OF VIRGINIA

Adam James Fallon

A Bose-condensate atom interferometer is used to measure vector tune-out wavelengths in ^{87}Rb . These are the polarization dependent wavelengths at which the ac electric polarizability equals zero. Precision control of the rotating magnetic bias field is demonstrated. This field is then used to vary the optical polarization in a controlled manner at the 10^{-5} level. This shifts the tune-out wavelength and the measured polarization dependence of the tune-out wavelengths is used to determine the various contributions to the polarizability including that of the core electrons, and notably the higher-lying dipole matrix element “tail” components. These tails are of importance to the theoretical analysis of atomic parity violation and other fundamental physics measurements. We report the first experimental measurement of tail components of the electric polarizability. These are $|t_{1/2}|^2 = 5(4)$ au and $|t_{3/2}|^2 = -4(4)$ au for the $n'J_{1/2}$ and $n'J_{3/2}$ components respectively. Within the experimental uncertainty they are in agreement with the best current estimates of these contributions $|t_{1/2}|^2 = 0.022(22)$ au and $|t_{3/2}|^2 = 0.075(75)$ au. Improvements to the experimental design to improve the experimental precision and place a better constraint on the tail values are discussed.

Acknowledgements

I could not have gotten through this difficult experiment without the unending support of friends and family. I will be forever grateful for the people who believed in me and helped make this happen and I would like to take a moment to thank some of them directly.

Julianne, your support through my many years of graduate school has been essential. I could not have done this without you. We took the leap and moved out to Virginia together to follow my dreams not knowing what to expect. We found a shared love of exploring our surroundings and taking time out of our hectic lives to enjoy life. We have pushed each other to achieve greater heights, and I am excited to see where life takes us next. Thanks for everything. I love you very much.

It's well-established at this point that Cass is a pretty incredible teacher. I want to also point out his almost inexhaustible optimism in the face of an ever more challenging precision experiment. This optimism instilled confidence and helped me realize that at some point we would run out of problems to solve and the experiment would actually work. This thesis is a testament to the fact that we did in fact solve (most) of the major issues we faced, and I'm glad the future of this experiment looks ever more promising.

Bob taught me how to run the experiment effectively. His tips and tricks for getting the most out of our apparatus have been key in my being able to keep it running. He did a really good job of passing on the important but fairly intangible skills needed to run a home-built BEC machine, and I have done my best to pass on this knowledge to help the next generation of graduate students.

Though never on my experiment directly, Eddie has helped me immensely over the years, through helping diagnose and fix problems with the experiment and just being there to chat and bounce ideas off of. I became the senior graduate student in lab just as he took over his experiment, and by teaching and explaining to him the various components of our systems, I developed a better understanding of practical BEC physics. His experiment is far from a carbon-copy of mine but the fundamentals are the same. Together we have refined our experiments by bringing

in more modern opto-mechanical techniques. I look forward to continuing our never-ending discussions on new techniques and technologies.

I want to thank my other labmates over the years as well, particularly Rob, Oat, and Seth. It's been a real pleasure learning from and working with all of you. My first year graduate cohort, especially the likes of Evan, Charles, and Dan, also deserve praise for helping me get through the first few years. It was a long road, and though not all of us made it all the way to the end, I'm glad we managed to have some fun and not entirely lose our minds along the way. The physics department is full of wonderful support staff and I'd especially like to thank Dawn, Peter, and Beth for their help navigating the bureaucratic side of graduate school so I could more easily focus on research. A special thanks is due as well to my Raven Society and Jefferson Fellows friends. It was great getting to spend time outside the lab engaged in interdisciplinary dialogue. The fancy dinners will be missed.

Finally, my parents have always been supportive and have been a key component in making this work possible. This research is the culmination of many years of schooling, and through these long years they have always encouraged and enabled my academic pursuits. Thanks for the unending enthusiasm. Much love.

Table of Contents

Abstract	i
Acknowledgements	ii
Table of Contents	iv
List of Figures	vi
List of Tables	viii
1 Introduction	1
1.1 Dipole matrix elements	2
1.2 Atomic parity violation	5
1.3 Tune-out wavelengths	8
2 Experimental apparatus	19
2.1 Magneto-optical trap	20
2.2 Magnetic trap loading	25
2.3 Evaporative cooling	28
2.4 Time-orbiting potential trap	30
2.5 Waveguide	34
2.6 Interferometry	37
2.7 Absorption imaging	43
3 Polarization control	45
3.1 Non-ideal magnetic waveguide	46
3.2 Magnetic field control	53
3.3 Beam alignment	57
3.4 Optical polarization characterization and control	61
3.5 Pulse timing choices	71
3.6 Timing error	82
3.7 Wavelength dependence	84

4	Tune-out wavelength measurements	91
4.1	General procedure	92
4.2	Theory	96
4.3	Experimental overview	102
4.4	$v = 0.5$ measurement	109
4.5	Polarization improvements	115
5	Conclusion and future work	122
5.1	Impact of results	122
5.2	Experimental improvements	126
5.3	Higher-lying tune-out wavelengths	134
A	Laser system	139
A.1	New MOT setup	140
A.2	Stark setup	143
B	Twitch routines	146
B.1	Full BEC experiments	148
B.2	ADWIN outputs, Subroutines, and Evap.txt	157
	Bibliography	165

List of Figures

1.1	^{87}Rb ground state matrix elements	4
1.2	Running of the weak mixing angle	6
1.3	Scalar polarizability near $5P$ transitions	10
1.4	Tune-out wavelength extrema	12
1.5	Level diagram with polarization dependence	14
1.6	Scalar and vector polarizabilities	16
2.1	Tapered amplifier $2\times$ pass setup	23
2.2	Maxwell-Boltzmann distribution during evaporation	29
2.3	Bragg interferometer timing	39
2.4	Stark interferometer timing	40
2.5	Recombination offset	41
2.6	Interferometer phase output	42
2.7	Imaging optics	44
3.1	CW rf spectroscopy data	53
3.2	Pulsed rf spectroscopy data	55
3.3	B_y trajectory	57
3.4	Schematic of Stark and probe optics	58
3.5	Stark beam and atoms composite	59
3.6	Wave plate polarization optimization	64
3.7	Poincaré sphere	65
3.8	Poincaré pole calculation results	66
3.9	Stark pulse timing optimization	67
3.10	Dark state level diagram	67
3.11	$ \mathcal{E}_\pi ^2$ model and data	68
3.12	Stark beam alignment with bias field	71
3.13	Ideal pulse timing diagram	74
3.14	Result of optical dipole force	75
3.15	Realized pulse timing diagram	81
4.1	Example vector tune-out data	94
4.2	Vector polarizability model	101
4.3	Vector polarizability data	106
4.4	Wave plate optimization	110

4.5	Vector TOW	112
4.6	Vector results	113
5.1	Stark pulse shape	129
5.2	Higher order bias field	132
5.3	Scalar polarizability near $6P$ transitions	137
A.1	MOT laser AOM configuration	141
A.2	Stark laser AOM configuration	144

List of Tables

1.1	Scalar polarizability components	15
2.1	Laser cooling timings	27
2.2	rf evaporation stages	33
2.3	TOP trap ramps	33
3.1	Timing errors from pulse generator	83
4.1	A_{th} and B_{th} components	102
4.2	Vector tune-out error budget	114
4.3	Improvements in integrated intensity	118
4.4	Reduction in dB	121
5.1	$6P$ $\alpha^{(0)}$ contributions	136
A.1	EO logic settings	143
A.2	AOM frequencies	145

Chapter 1

Introduction

Advances in atomic physics over the last century have led to the development of robust theoretical predictive techniques. Until quite recently, much of our knowledge of atomic structure informing these theoretical predictions has primarily been derived from precise spectroscopic measurements of atomic energy levels. While these measurements have led to significant advances in our understanding of the physical world and to numerous technologies upon which the modern world relies heavily, atomic energy levels are just part of the picture. A complimentary and necessary additional consideration is the atomic response to applied fields, in particular electric fields. This response is characterized by the electric polarizability.

The polarizability is fundamental to a number of physical phenomena. Examples include optical trapping [1], van der Waals interactions [2], and decoherence of quantum logic gates [3]. Additionally dipole matrix elements show up in far-reaching analyses such as atomic parity violation [4], which I will describe shortly.

In each of the cases, insufficient knowledge of either the polarizability or the dipole matrix elements included in calculation thereof is an important limitation on theoretical advancement. The work presented in this thesis outlines an experimental effort to make direct measurement of these difficult to access components of the polarizability possible.

This thesis is organized as follows: the remainder of this chapter continues the general motivation and introduces the polarizability in detail. Chapter 2 describes the experimental apparatus. Though it is described elsewhere [5–7], specific aspects of its design are relevant here. Chapter 3 goes over several tools necessary for the successful implementation of the general experimental method, specifically precision measurement and control of optical polarization. Chapter 4 presents the detailed theory of the polarization dependence of the polarizability and discusses the experimental results and several important challenges. It ends in Chapter 5 with the blueprints for several key improvements to the current experimental design and a roadmap for the next steps in the continuing experimental process to measure the higher-lying dipole matrix elements.

1.1 Dipole matrix elements

Dipole matrix elements characterize transition strengths between atomic states via an electromagnetic field and are thus vital when dealing with atom-light interactions as in the examples above. They are defined as $d_{if} = \langle i | \mathbf{d} | f \rangle$ and show up in many different but related atomic phenomena such as in the polarizability

α , atomic lifetimes τ , the Einstein coefficients, the C3 coefficient, and the oscillator strengths f_{if} . In general, the dipole matrix elements are not all well known and typically cannot easily be dealt with in broader, precision calculations and analyses.

The lowest-lying, principal ground state dipole matrix elements however are straightforward to measure in the alkalis. In ^{87}Rb , these are [8]

$$|d_{1/2}| = \langle 5S_{1/2} || \mathbf{d} || 5P_{1/2} \rangle = 4.233(2) \text{ au} \quad (1.1)$$

and

$$|d_{3/2}| = \langle 5S_{1/2} || \mathbf{d} || 5P_{3/2} \rangle = 5.978(4) \text{ au}. \quad (1.2)$$

These principal matrix elements can be measured in a number of ways: through lifetime measurements [9], fluorescence [10], and photo-association spectroscopy [11]. Combined, these results give a reasonable part per thousand accuracy, while leaving significant room for improvement. Unfortunately in many cases, such as those mentioned previously, an infinite sum over all dipole matrix elements is typically present in the theoretical calculations of interest, and higher-lying matrix elements, such as $n' > 5$ for ^{87}Rb , are much more difficult to measure directly with any reasonable precision due to the introduction of multiple potential decay paths.

It is however possible to calculate an individual dipole matrix element with reasonable precision [12]. The lower-lying matrix elements which tend to dominate typical applications are the most straightforward, and reasonable numbers exist for

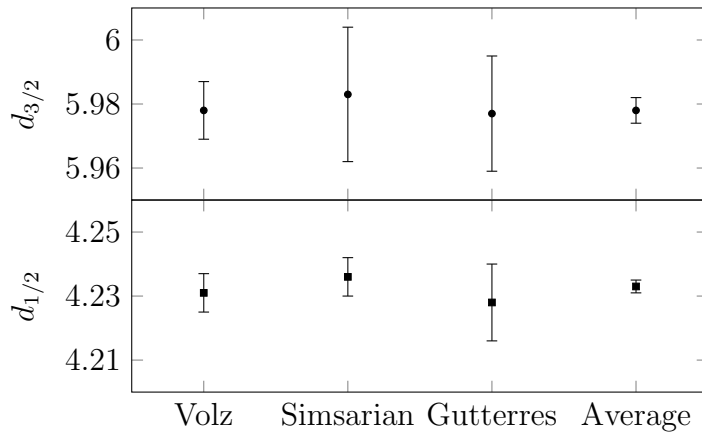


FIGURE 1.1: ^{87}Rb ground state dipole matrix element values. The points show measurements of the $|d_J| = \langle 5P_J || \mathbf{d} || 5S_{1/2} \rangle$ dipole matrix elements, for $J' = 1/2$ (squares) and $J' = 3/2$ (circles). The first three points are measurements by Volz et al. [9], Simsarian et al. [10], and Gutterres et al. [11]. The fourth point is the error-weighted average from the three groups.

^{87}Rb up to $n' = 12$ [8]. The infinite remaining higher-lying dipole matrix elements (e.g. $n' > 12$ in ^{87}Rb) though do not fall off sufficiently fast to be neglected in any calculation with a sum over all states, and become harder to calculate at higher energy as the volume encompassed by the wave function grows. They are commonly lumped into a single term referred to as the “tail” in theoretical calculations. Any value given for this term is typically just an estimate of the contribution of these uncalculated terms. As this is a difficult task, these estimates tend to have 100% uncertainty [13–15].

Through several novel advances in the relatively new measurement technique of tune-out wavelength spectroscopy, the work presented in this thesis describes a push towards the first experimental measurement of these difficult to measure high-lying matrix elements. We expect that the full results to serve as a benchmark for theorists on which to test their calculations techniques to better predict the infinite manifold of dipole matrix elements, not just in ^{87}Rb but also the other

alkalis and beyond.

1.2 Atomic parity violation

I want to briefly touch on atomic parity violation (APV) as an example to better put into context how dipole matrix elements appear in theoretical calculations. Atomic parity violation is a low-energy atomic physics measurement which can place a useful constraint on the Standard Model. By measuring the asymmetry in a dipole-forbidden $S \rightarrow S$ transition, it is possible to extract the weak charge of the neutron. This can be used to find the weak mixing angle θ_W [16], which is one of the free parameters in the Standard Model. The value of the weak mixing angle depends on energy, with different regimes in its running dependent on the mass of various fundamental particles. Its energy dependence and the numerous measurements to constrain it is shown in Fig. 1.2. We can see that θ_W varies little below roughly 100 GeV. In this regime, several fundamentally different experiments can constrain this value at energies spanning two orders of magnitude [17–19].

Atomic parity violation is one of those experiments. The best APV measurement to date was performed in 1997 using a Cs atomic beam apparatus at JILA. The experiment was able to achieve a 0.35% experimental uncertainty [17]. Relating the transition amplitude of this dipole-forbidden transition to the weak mixing angle involves an infinite sum over states of the following form

$$A_{PNC}^{Theory} = \sum_{n'=6}^{\infty} \left(\frac{\langle 7S | \mathbf{d} | n' P_{1/2} \rangle \langle n' P_{1/2} | H_{PNC} | 6S \rangle}{E_{6S} - E_{n' P_{1/2}}} + \frac{\langle 7S | H_{PNC} | n' P_{1/2} \rangle \langle n' P_{1/2} | \mathbf{d} | 6S \rangle}{E_{7S} - E_{n' P_{1/2}}} \right). \quad (1.3)$$

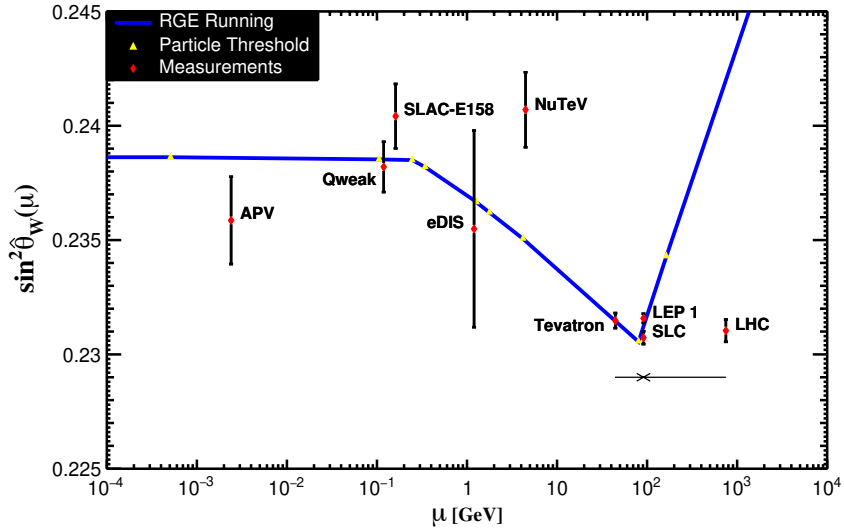


FIGURE 1.2: Shown here is the running of the weak mixing angle θ_W . Of particular interest are the three lowest energy measurements, APV, Qweak, and SLAC-E158, which constrain θ_W at low energies, but currently are in some disagreement. Better understanding of high-lying dipole matrix elements can help reduce the APV uncertainty. The figure is taken from the 2018 Particle Data Group’s update [20].

A_{PNC} is the parity nonconservation amplitude. The parity non-conserving terms in the sum, $\langle n'P_{1/2}|H_{PNC}|6S\rangle$, are straightforward to calculate directly. The difficulty in this analysis lies instead in the dipole matrix elements $|\mathbf{d}_{if}| = \langle i||\mathbf{d}||f\rangle$ where there is insufficient theoretical or experimental constraint on the values as the sum tends to infinity. As of this writing, the best theoretical values for this sum introduces an uncertainty on the order of the experimental uncertainty, at 0.4%, and even through significant refinement of the calculation techniques, actual reduction in this analysis-derived uncertainty has progressed slowly over the past decade [13–15]. This is a testament to the difficulty inherent in this problem. As much as 80% of the uncertainty from the analysis is from the higher-lying tail contribution, which have effectively preempted any motivation for a new APV

measurement using recent advances in the field.

Recent measurements including Möller at SLAC [18] and QWeak [19] at JLAB, have driven down uncertainties on θ_W in the intermediate energy regime. Since these experiments constrain the weak mixing angle in a similar region to APV where the running of the weak mixing angle is flat, it is worthwhile to consider how to improve upon the APV number to continue giving a competitive independent measurement, particularly as the other experiments in the low energy regime have thus far been unable to reach their design precisions leaving further room for improvement across the low energy regime. It is worth noting also that these measurements show some disagreement.

Reducing the various uncertainties might help give insight into why this disagreement is present. Without even the need for a new experimental measurement, there is nearly a factor of two to gain through driving down the theoretical uncertainty introduced by the APV analysis. The bulk of this dissertation lays out a roadmap to doing just that through the use of precision measurements of dipole matrix elements using the ac Stark effect and related tune-out wavelengths. We further hope to motivate new APV measurements once the uncertainty in the analysis is reduced to take advantage of improvements in atomic physics techniques that have emerged in the past two decades.

1.3 Tune-out wavelengths

A significant motivation for the work presented in this thesis is in the need for either experimental measurements or improved theoretical calculations of the dipole matrix elements. We seek to develop and implement an experimental program to measure the matrix elements needed for the atomic parity violation and other analyses using our ^{87}Rb Bose-condensate atom-interferometer. Though the APV measurement of Wood et. al. [17] was done using Cs for improved sensitivity, we hope that our work will serve as a benchmark for theoretical calculation techniques needed to estimate the higher-lying and tail contributions.

One way to measure the dipole matrix elements is through measurements of the Stark effect [21], an energy shift due to an applied electric field. This shift is expressed as

$$U = -\frac{1}{2}\alpha(\omega)\langle\mathcal{E}^2\rangle. \quad (1.4)$$

This energy shift is proportional to the electric polarizability α , and the square of the electric field $\langle\mathcal{E}^2\rangle$. Notably, the matrix elements of interest are contained in α . Being a second order perturbative effect, α takes the form

$$\alpha_i(\omega) = \frac{1}{\hbar} \sum_f \frac{2\omega_{if}}{\omega_{if}^2 - \omega^2} |d_{if}|^2. \quad (1.5)$$

The sum is over all final states with the subscripts i and f denoting the initial and final states respectively. The matrix elements are defined as usual as $|d_{if}| = \langle i|\mathbf{d}|f\rangle$. Through the choice of initial state i , the matrix elements needed

in the APV analysis can be represented in the sum, though our initial implementation will focus on the ground state matrix elements $|\mathbf{d}_f| = \langle 5S_{1/2} || \mathbf{d} || f \rangle$. The transition frequencies between states i and f are given by ω_{if} , and ω is the oscillation frequency of the electric field.

Precision measurements of the dc Stark effect have been done [22, 23], but they lack the ability to fully separate out the individual matrix elements of interest. The use of an oscillating electric field $\mathcal{E} = \mathcal{E}(t)$ makes use of the ac Stark effect and allows taking advantage of the different frequency dependences of the various terms in α . This separation of terms is crucial in being able to determine the individual dipole matrix elements, though there are significant drawbacks to ac Stark measurements that must be overcome. Unlike in a dc Stark measurement where an electric field constant in time can readily be calibrated, *in situ* intensity calibration of an oscillating electric field such as from a laser is difficult to do with any reasonable precision making direct ac Stark shift measurements ill-suited for measuring dipole matrix elements [24]. Fortunately an alternative experimental technique exists.

If we look at Fig. 1.3 showing the polarizability between the D_1 and D_2 lines, we can see that there is a frequency ω where $\alpha(\omega) = 0$. As long as $U \propto I$, then if $\alpha(\omega_0) = 0$ for some ω_0 , it follows that $U(\omega_0) = 0$ for any intensity I , thereby getting around the intensity calibration issue in direct measurements of the Stark shift. Zeroes in the ac electric polarizability are known as tune-out wavelengths. The locations of tune-out wavelengths are dependent essentially upon ratios of the dipole matrix elements for the relevant states. This can be seen for example if one

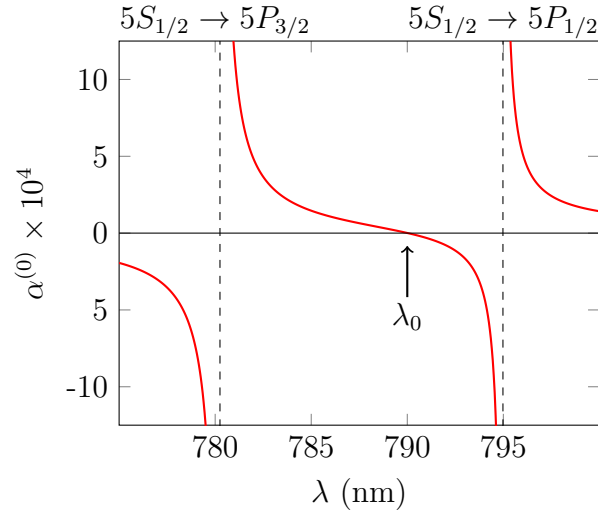


FIGURE 1.3: Pictured here is the scalar polarizability near the $5S_{1/2}$ to $5P_{1/2}$ and $5P_{3/2}$ transitions. The tune-out wavelength near 790 nm is marked as λ_0 .

only considers the lowest lying contributions in Eq. (1.5). If it were possible then to measure all tune-out wavelengths, we could relate the higher-lying dipole matrix elements to the better known principal matrix elements. This is not feasible in practice, but a finite number of tune-out wavelength measurements can still give useful constraints. This thesis will develop this idea further and work through some of the specific information about the various contributions we eventually hope to extract from these measurements.

We can rewrite α to separate contributions from the core and valence electrons. Equation (1.5) contains a sum over all possible excitations, including those of the core electrons, which we can be combined into a single term for the core polarizability α_c because the core excitations happen at much higher frequencies deep in the ultra-violet [25]. There is a slight overestimate in doing this due to the presence of the valence electron preventing some excitations through the Pauli exclusion principal, therefore a correction to α_c is needed. This is referred to

as the core-valence interaction and is denoted by α_{cv} . These are both calculable in the random-phase approximation [26] to give reasonable values, and there is a recent experimental measurement of the core polarizability in ^{87}Rb [27]. The polarizability becomes

$$\alpha_i(\omega) = \frac{1}{\hbar} \sum_{n', J'} \frac{2\omega_{if}}{\omega_{if}^2 - \omega^2} |d_{if}|^2 + \alpha_c + \alpha_{cv} \quad (1.6)$$

where i and f now denote the valence states with the sum over $n' \geq 5$ and $J' = 1/2$ and $3/2$. The frequency dependence of $\alpha_c + \alpha_{cv}$ is not explicitly shown here but it can be determined to reasonable precision [28].

Tune-out wavelengths have significant dependence on the optical polarization of the applied light field in spin-polarized systems such as ours. This dependence introduces complexity into our tune-out wavelength measurements as we need to precisely characterize the polarization to account for its effect. We can see this dependence by decomposing the polarizability, α , into its spherical irreducible tensor components. We can then re-express the interaction energy using Eq. 1.4 as

$$U = -\frac{\langle \mathcal{E}^2 \rangle}{2} \left\{ \alpha^{(0)} - \frac{1}{2} S_3 \cos \theta \frac{m_F}{F} \alpha^{(1)} + \left(\frac{3 \cos^2 \xi - 1}{2} \right) \frac{3m_F^2 - F(F+1)}{F(2F+1)} \alpha^{(2)} \right\}. \quad (1.7)$$

Here, $\alpha^{(0)}$ is the polarization independent scalar polarizability. The vector polarizability $\alpha^{(1)}$ depends on the amount of circular polarization with $S_3 = \langle E_t^2 \rangle - \langle E_r^2 \rangle$ being the fourth Stokes parameter. It varies from ± 1 for left and right hand circular polarization respectively and is 0 for linearly polarized light. The orientation of the Stark laser comes in through $\cos \theta = \hat{k} \cdot \hat{b}$ which accounts for the

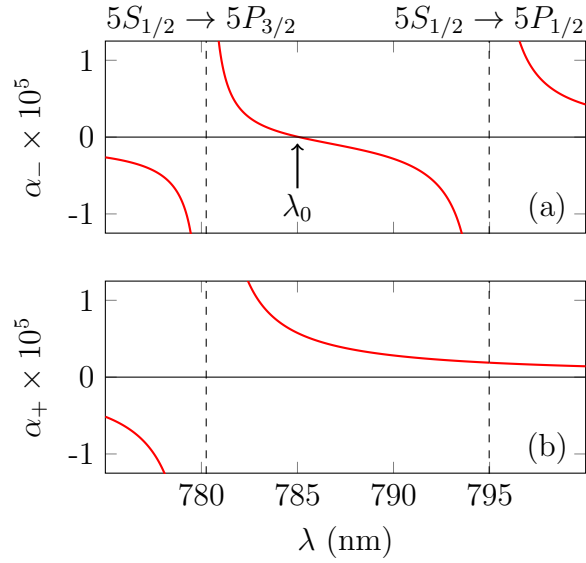


FIGURE 1.4: Pictured are the extreme examples of how the tune-out wavelength varies with the amount of vector polarizability using atoms spin polarized in the $|F, m_F\rangle = |2, 2\rangle$ state. (a) shows the case with fully σ^- light ($S_3 = 1$). The tune-out wavelength is shifted to near 785 nm. (b) has fully σ^+ light ($S_3 = -1$) where the zero crossing occurs on resonance.

alignment of the Stark beam with respect to the quantization axis pointing in \hat{b} . The tensor polarizability $\alpha^{(2)}$ characterizes the response to the orientation of the light's polarization vector \hat{e} through $\cos \xi = \hat{e} \cdot \hat{b}$. Additionally, Eq. (1.7) depends on the atomic hyperfine structure through the hyperfine level F and magnetic sub-level m_F terms in the coefficient and in the spherical tensor components $\alpha^{(i)}$ themselves.

The scalar and vector components are of similar magnitude and are both large compared to the tensor component. We can see in Fig. 1.4(b) that in our spin-polarized atomic system the vector polarizability is sufficiently large to eliminate the tune-out wavelength altogether for a particular optical polarization. This occurs because there is no coupling to the D_1 manifold for σ^+ -polarized light and thus no cancellation of terms.

The tensor component on the other hand is small. Its contribution accounts for the difference in the polarizability of linearly polarized light made up of either equal parts σ^+ and σ^- or π and is smaller than the scalar polarizability by a factor of roughly $\Delta\omega_{HF}/\Delta\omega_F \approx 10^{-4}$ for the hyperfine and fine structure splittings respectively. This is due to the three polarization components coupling to different magnetic sub-levels. While it appears in the analysis of our scalar polarizability measurement [8], the tensor polarizability $\alpha^{(2)}$ will be absent in the rest of this section and in the discussion and analysis to come due to its small overall contribution and our neglecting most of the hyperfine structure in this initial measurement involving a nonzero vector polarizability. As the experimental uncertainty of the vector tune-out wavelength measurement presented here is reduced, it will be necessary to bring $\alpha^{(2)}$ and hyperfine structure back into the full analysis. Fortunately the framework for doing so is already well established [29, 30].

The scalar tune-out wavelength where $\alpha^{(0)} = 0$ has been measured previously in several atomic species. Our previous measurement is currently the most precise [8]. The methods we will develop through the course of this thesis are similar to what was employed in that measurement. Other measurements typically use either $m = 0$ atoms [32] or a thermal mixture [33] to avoid the difficulty of carefully controlling the optical polarization by removing any dependence on $\alpha^{(1)}$ and $\alpha^{(2)}$ leaving just the polarization independent scalar term. Table 1.1 shows the individual contributions to the scalar polarizability which cancel at the tune-out wavelength.

The scalar tune-out wavelengths near the $6P$ states have also been measured

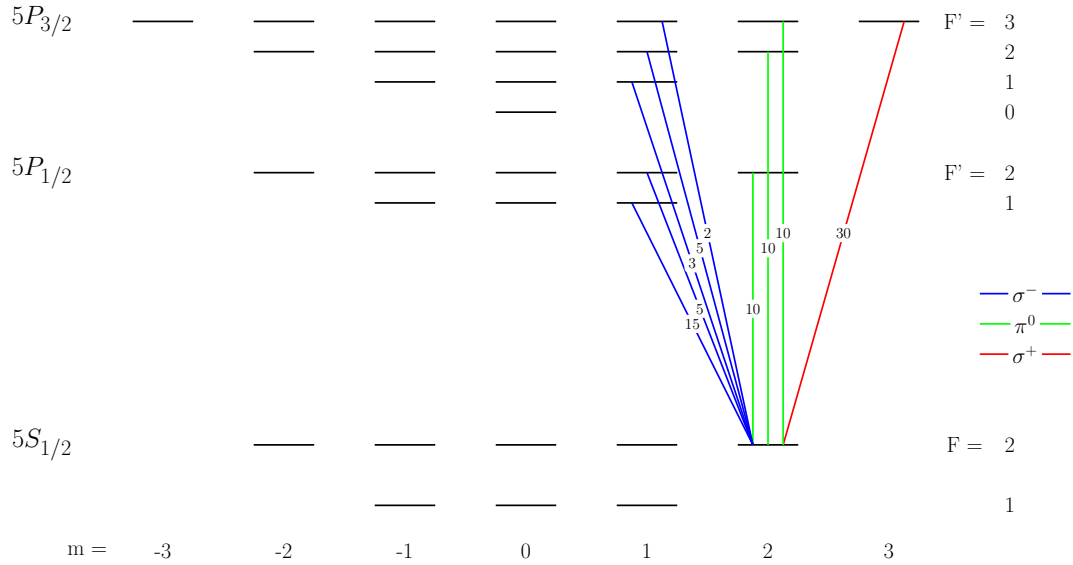


FIGURE 1.5: Dipole matrix elements expressed as multiples of $30 \times \langle J = 1/2 || \mathbf{d} || J = 1/2 \rangle$ [31]. This figure gives a sense of the polarization dependence of the tune-out wavelength, where the polarization components couple differently to the available states. For our spin-polarized atoms, where $\alpha(\omega_0) = 0$ depends on the specific optical polarization. We will put this to use in measuring $\alpha^{(1)}$.

in ^{87}Rb [34]. They improved the experimental precision of the dipole matrix elements for those states to an order of magnitude better than the best theoretical values [12]. Beyond just a new way to measure dipole matrix elements, tune-out wavelengths have also proven useful in applications such as state or species specific optical trapping and manipulation [36–39] and rotation sensing [40].

Of particular interest in this work is $\alpha^{(1)}$, the vector polarizability, which has a different frequency response and its inclusion allows the separation of $n'P_{1/2}$ and $n'P_{3/2}$ contributions. Tune-out wavelength measurements involving this component are only possible in spin-polarized systems such as ours, and our apparatus is well suited for these measurements. The frequency dependence of the scalar and vector polarizabilities are seen in Fig. 1.6. Written explicitly and neglecting

Source	Matrix value	$\alpha^{(0)}$
$5P_{1/2}$	4.233(2)	-8233.6
$5P_{3/2}$	5.978(4)	8222.9
$6P_{1/2}$	0.3235(9)	0.451(3)
$6P_{3/2}$	0.5230(8)	1.173(4)
$7P_{1/2}$	0.115(3)	0.044(2)
$7P_{3/2}$	0.202(4)	0.135(6)
$8P_{1/2}$	0.060(2)	0.011(1)
$8P_{3/2}$	0.111(3)	0.037(2)
$9P_{1/2}$	0.037(3)	0.004(1)
$9P_{3/2}$	0.073(5)	0.015(2)
$10P_{1/2}$	0.026(2)	0.002
$10P_{3/2}$	0.053(4)	0.008(1)
$11P_{1/2}$	0.020(1)	0.001
$11P_{3/2}$	0.040(3)	0.004(1)
$12P_{1/2}$	0.016(1)	0.001
$12P_{3/2}$	0.033(2)	0.003
α_c	-	9.063(7)
$\alpha_{cv}^{(0)}$	-	-0.37(4)
$\alpha_{cv}^{(1)}$	-	-0.04(4)
$ t_{1/2} ^2$	-	0.022(22)
$ t_{3/2} ^2$	-	0.075(75)
Total	-	0.001

TABLE 1.1: Scalar polarizability components calculated at 790.02568 nm to show the scalar tune-out wavelength. The $6P$ matrix elements are taken from Ref. [34]. All other discrete matrix elements including the tails $|t_{J'}|^2$ are described in Refs. [8, 35]. The core contributions are taken from Refs. [12, 27, 28].

hyperfine structure, $\alpha^{(0)}$ and $\alpha^{(1)}$ take the forms

$$\alpha^{(0)} = \frac{1}{3\hbar} \sum_{n', J'} |d_{if}|^2 \frac{\omega_{if}}{\omega_{if}^2 - \omega^2} + \alpha_c + \alpha_{cv}^{(0)} \quad (1.8)$$

and

$$\alpha^{(1)} = \frac{1}{3\hbar} \sum_{n', J'} (3J' - 7/2) |d_{if}|^2 \frac{\omega}{\omega_{if}^2 - \omega^2} + \alpha_{cv}^{(1)}. \quad (1.9)$$

The sums are over n' and J' as before. The contribution from the core, α_c , has

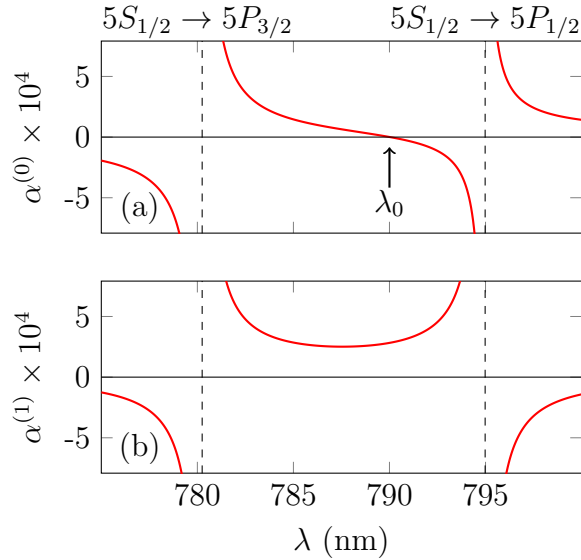


FIGURE 1.6: Comparison of scalar and vector polarizabilities near the the D_1 and D_2 lines. The vector polarizability has no zero crossing. The introduction of a non-zero vector polarizability results in a shifted tune-out wavelength. Both are in atomic units.

no vector component due to its spin-less, spherically symmetric nature. The core-valence correction, $\alpha_{cv} = \alpha_{cv}^{(0)} + \alpha_{cv}^{(1)}$, can have both scalar and vector components. No direct experimental evidence yet exists for $\alpha_{cv}^{(1)}$, but by combining measurements of the scalar and vector polarizabilities, this term as well as the currently inaccessible higher-lying dipole matrix elements will be accessible via tune-out wavelength spectroscopy [28].

From Eq. (1.3), we can see that only the $n'P_{1/2}$ higher-lying tail contributions specifically are needed for the APV analysis, and from Eqs. (1.8) and (1.9) it is evident that the contributions to the scalar polarizability from the matrix elements of the $n'P_{1/2}$ and $n'P_{3/2}$ states come in together via a sum. So while allowing a potentially useful estimate of the two tail contributions together, scalar tune-out wavelength measurements alone do not remove the need for an imprecise estimate of the higher-lying states in the APV analysis. What measurements involving

the vector polarizability contribute is the ability to separate out the $n'P_{1/2}$ and $n'P_{3/2}$ tail contributions due to the J' contributions having different coefficients. Therefore, by combining measurements of scalar and vector tune-out wavelengths it should be possible to determine the $n'P_{1/2}$ and $n'P_{3/2}$ tail contributions individually.

The basic premise for making a measurement of $\alpha^{(1)}$ involves precisely controlling optical polarization of the Stark light, particularly the fourth Stokes parameter S_3 , and measuring the shifted tune-out wavelength. Much of the work in this thesis is focused on developing the polarization control techniques. Figure 1.4 shows the two extremes of the available tuning range between the D_1 and D_2 lines, taking the tune-out wavelength from near 785 nm to the D_1 resonance at 795 nm.

We will work through a more complete model of the tune-out wavelength's polarization dependence in Chapter 4 which we will use to extract information on the higher-lying dipole matrix elements. It is worth specifically mentioning here though that the tail contributions have not been measured experimentally before, so the work presented here will give the first experimental constraint on these terms. We will see that numerous improvements will be necessary, but that this general method of tune-out wavelength spectroscopy shows promise.

Additional measurements near the $6P$ and $7P$ resonances however will be required to fully extract the tail contributions as uncertainties on the core-valence terms are of similar size to those of the tails. Measurements at different wavelengths will allow separation of the core-valence and tail terms and drive down

uncertainties on all of them. It is then that we expect this work to have an impact as a benchmark for theoretical calculations and possibly begin to drive down the analysis-derived uncertainty in the APV results.

Chapter 2

Experimental apparatus

In this chapter I will outline the procedures we use to create a Bose-condensate atom interferometer. At this point in time these procedures are quite well defined and have been put into practice in this lab relatively unchanged for more than a decade. We start with the main workhorse of many atomic physics laboratories, the magneto-optical trap. We then load the atoms into a tightly confining purely magnetic trap where the condensate is produced. Through the use of an off-resonant standing wave, we can split the condensate into multiple packets traveling along different trajectories, the “arms” of our interferometer. The packets achieve macroscopic separations allowing us to probe them independently. This results in a controllable differential phase shift between the packets which we can read out upon recombination. We will use this interferometer to measure the tune-out wavelengths described in Chapter 4.

We will start this discussion with a brief overview of the various stages in Bose-Einstein condensate (BEC) production. A more detailed discussion can be found in Ref. [5].

2.1 Magneto-optical trap

Our experiments are done in a vacuum chamber. A rubidium vapor is supplied by a pair of getter-dispensers run in series at 2.6 A. We have two separate sets of these getters to limit how often we need to break vacuum in order to replace them. With conservative usage, they can last for several years. Rubidium atoms in this thermal background vapor are initially trapped and cooled by a magneto-optical trap (MOT). Let us build up just the rough mechanism for cooling as MOTs have been a mainstay in atomic physics laboratories for many years now and the techniques involved are well-developed and described in more detail elsewhere [41].

There is a straightforward multi-tiered approach to the basic cooling mechanism in a MOT. We will start with the optical component of a magneto-optical trap. In the reference frame of a moving atom, a laser's frequency will be shifted due to the Doppler effect. If the atom is moving towards the source, the laser will be blue-shifted, i.e. the atom will see the light as having a higher frequency than if it was at rest with respect to the laser source. A red-detuned laser will therefore be shifted closer to resonance for reasonably low velocities. The atom will then be more likely to absorb and scatter photons. As the atom absorbs a photon in the direction of the laser beam and emits it in a random direction, the net force

on the atom is in the opposite direction of the beam. The laser thus exerts a force opposing the atom's movement and acts to slow down the atom. This effect is called Doppler laser cooling [42]. By using three pairs of counter-propagating red-detuned lasers overlapped in space, the atomic motion in all directions can be effectively arrested.

There is a limit to purely optical Doppler cooling. The atoms are eventually cooled enough that the Doppler cooling and recoil heating balance out. The atoms then simply pass through the beam overlap region unimpeded. To overcome this limit and ultimately trap the atoms for further long term study and manipulation, we add a magnetic field. A pair of coils in an anti-Helmholtz configuration creates a dc magnetic spherical quadrupole field with a field zero aligned within the overlap region of the beams. As the atoms move away from the field zero, their energy levels undergo magnetic field-dependent Zeeman shifts. With the correct choice of polarization in each counter-propagating beam, the beam tending to push the atoms back towards the field zero is preferentially brought into resonance. Left- and right-hand circular polarizations are typically used.

We cool on the usual $5S_{1/2} F = 2 \rightarrow 5P_{3/2} F' = 3$ cycling transition with a detuning of 25 MHz. Roughly 1 out of every 250 photons excite the atoms to the $5S_{1/2} F = 2 \rightarrow 5P_{3/2} F' = 2$ state which has a 50% chance to decay into the $F = 1$ ground state. Since this is dark to the cooling light, the atoms need to be brought back in resonance by additional light on the $5S_{1/2} F = 1 \rightarrow 5P_{3/2} F' = 2$ line. This light is typically referred to as the "repump". Little repump light is needed. We typically use up to 5 % of the total optical power. Instead of having a separate

laser locked to the appropriate atomic transition to produce the repump light as is common elsewhere and was previously used on this experiment, the method we use now involves adding sidebands at the repump detuning to the main MOT laser before injecting it into a tapered amplifier (TA). We add the sidebands with a fiber-coupled electro-optic (EO) modulator [43].

One drawback of the specific EO we are using is that it has a relatively low optical power limit. Damage to the EO material begins around 5 mW for near infrared light, and though this damage is not permanent, we need to stay below this power limit for stable operation. Most TAs need more than 10 mW seed light to saturate. To ensure proper saturation of our chip, we devised a way to achieve two passes through the amplifying medium. This allows the use of very low initial seed light well below the damage threshold of the EO, but with enough gain through the first pass to fully saturate the TA on the second pass. The initial idea and feasibility of this method has been shown elsewhere [44–46].

We inject roughly 50 μW of light into the output facet of the TA by coupling the light in through the auxiliary port on the output side of the optical isolator. An isolator with access to all the ports is obviously necessary. The one in this setup uses polarizing beam splitting cubes on both sides of the Faraday rotator. The isolator is aligned such that the usual output port is horizontally polarized for easy access. By sending light vertically polarized into the output rejection port, we are able to send light through the isolator to seed the laser. A half-wave plate is necessary as the input port of the isolator is at 45° . Care is taken to avoid any reflections from reaching the amplifier chip.

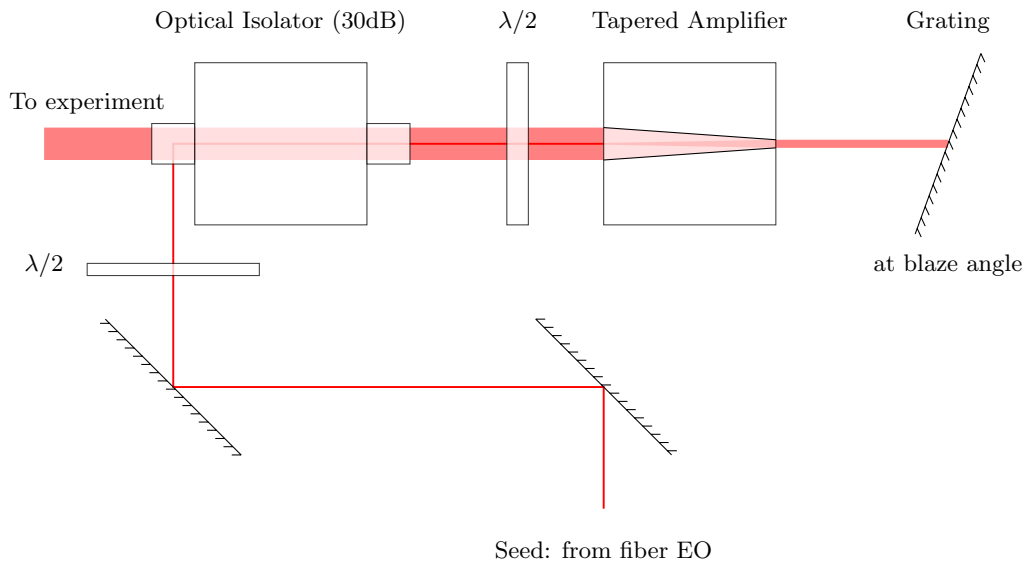


FIGURE 2.1: Optics setup for double pass tapered amplifier system. The seed beam is coupled through output auxiliary port of optical isolator. A grating is aligned at its blaze angle to supply 1st order for feedback for a second pass through the gain medium. This setup allows the use of a low damage threshold electro-optic modulator to generate the repump sidebands on the MOT seed beam.

The first pass through the TA yields around 30 mW optical power. This light is primarily amplified seed light, but some amplified spontaneous emission (ASE) light remains because the first pass is well below saturation. When initially running with just a retro reflection mirror, we found that roughly 1/3 of the light was made up of ASE. This only caused issues during imaging as the our probe light was not fully resonant and thus not fully absorbed. We had no issues creating a MOT or getting a reasonable atom number in the condensate. By replacing the retro mirror with a grating aligned at the blaze angle, we were able to suppress unwanted ASE light to below a few percent, which is a much more reasonable and easily tolerated background level in imaging. Further discussion of the EO and other components in the MOT optical setup can be seen in Appendix A. We can

now continue with the discussion of cooling.

As the atoms are cooled and trapped, the atomic density in the MOT rises. Eventually this makes the center optically thick where the cooling light is unable to penetrate. The central atoms instead begin experiencing multiple photon scattering events where the subsequent photon emissions likely have the wrong polarization. Cooling ceases to be effective. In our trap this occurs at just below 1 mK. To allow the cooling light back into the dense center, we do two things. First, we reduce the amount of repump light so that the atoms spend more time in the dark $5S_{1/2} F = 1$ ground state. Additionally, we increase the detuning from 25 MHz to 50 MHz over 10 ms. With more cooling light penetrating the MOT, the atoms cool to around 400 μ K. Further detuning results in colder atoms, but this is as far as we can detune using our double-pass AOM while ensuring enough light gets through to saturate the TA. This stage is called a compressed-MOT (CMOT). Additionally, atoms cease loading into the trap during this stage, so we can only briefly apply the CMOT. The use of these two configurations in tandem gives us the benefit of both: the quick loading time of the MOT, and the cooler temperature of the CMOT. We cannot remain in the CMOT for too long though as the losses due to background collisions will eventually negate any benefits.

We do one final cooling stage involving the lasers, where we turn off the magnetic field entirely while turning the repump light back up for 10 ms. This creates an optical molasses, a sub-Doppler cooling technique also known by the mechanism causing the cooling, polarization gradient cooling. This will not be discussed in detail here as more thorough descriptions can be found elsewhere

[47]. At the end of these laser cooling stages, we have roughly 2 billion atoms at around 250 μK .

We need to further cool and compress the atoms to create the BEC. After all of these optical cooling stages we're still 8 orders of magnitude from the necessary phase-space density for condensation to occur. We continue the cooling process by switching to a purely magnetic trap to greatly increase the density and transport the atoms into a lower pressure science cell.

2.2 Magnetic trap loading

Neutral atoms were first magnetically trapped in 1985 [48]. This method works when the neutral atom, ^{87}Rb in our case, has a nonzero magnetic moment which interacts with a magnetic field. This interaction energy can be expressed as

$$U = -\vec{\mu} \cdot \vec{B}. \quad (2.1)$$

The magnetic field is a dc spherical quadrupole field described by

$$\mathbf{B}_Q = B'_Q(2z\hat{z} - x\hat{x} - y\hat{y}). \quad (2.2)$$

Additionally, the magnetic moment is $\mu = g_F m_F \mu_B$ given the Landé g-factor g_F , the magnetic hyperfine sub-level m_F , and the Bohr magneton μ_B . The force

due to the magnetic field is then given by

$$\mathbf{F} = g_F m_F \mu_B \nabla |B|. \quad (2.3)$$

This informs our decision about which m sub-level to use. Three ground state m -sublevels are weak field seeking in ^{87}Rb making them magnetically trappable using \mathbf{B}_Q due to the field zero at its center. These are $5S_{1/2} |F, m_F\rangle = |2, 2\rangle$, $|2, 1\rangle$, and $|1, -1\rangle$. The other states are strong field seeking with the exception of the $m = 0$ states which are insensitive to the magnetic field. A design choice in our experimental apparatus pushes us to use $|2, 2\rangle$. This introduces a slight difficulty in that the MOT does not favorably populate this state. If we assume an equal population among the m -sublevels, the 20% population in the correct state would be insufficient. We must then optically pump the atoms into the correct m -sublevel to trap a large enough population to later create the condensate.

To implement optical pumping, we apply σ^+ polarized light to the atoms for 0.5 ms with the large dc quadrupole field turned off. An additional bias coil is turned on during this time to better define the polarization and overcome any background fields which may affect its purity. We choose to optically pump on the non-cycling $5S_{1/2} F = 2$ to $5P_{3/2} F' = 2$ transition, so that when atoms end up in the desired $5S_{1/2} |F, m_F\rangle = |2, 2\rangle$ ground state, they no longer scatter photons. This reduces the optical thickness for the remaining atoms being pumped. At the end of the 0.5 ms we have roughly 60% of the atoms in the desired state.

We then turn on the magnetic trapping field. This is done quickly and the

Cooling/trapping step	Duration (ms)
MOT loading	60000
CMOT (ramp)	10
Molasses	5
Optical pumping	0.5
Magnetic trap capture (ramp)	15
Magnetic trap to full (ramp)	100

TABLE 2.1: Timings of individual steps in cooling from the MOT to being magnetically trapped in the dc spherical quadrupole. Not listed are additional delays necessary for switching bias fields and lasers. The long MOT loading time is primarily for thermal considerations in the dc quadrupole coils and waveguide to ensure run-to-run stability. The MOT is typically fully loaded in 5 to 10 s. The full timing sequences can be seen in Appendix B.

gradient is chosen such that the size of the magnetic trap matches closely the spatial distribution of the atoms after the laser cooling and pumping stages. This was previously determined to be when the gradient is roughly 60 G/cm. The field is then adiabatically ramped to its maximum of 400 G/cm. The field is generated by the same coils used in the MOT, and the increase in field strength increases the atomic density. The process is adiabatic, so the atoms are still 8 orders of magnitude below the necessary phase-space density to create a condensate. Once the atoms are loaded into this purely magnetic trap, we physically transfer the atoms into our lower background pressure science cell by translating the coil assembly on a Parker Motion precision stage. This process takes about 2 s, with time to accelerate and decelerate in a manner to minimize the introduction any of center-of-mass motion.

The MOT chamber and science cell are separated by a roughly 30 cm long tube with a 1 cm diameter with the total distance traversed being approximately 60 cm. This transfer allows the science cell, which is pumped by both an ion

pump and titanium sublimation pump, to maintain a much lower background pressure on the order of 5×10^{-11} torr as compared to the roughly 10^{-9} torr in the MOT chamber. As 3 body collisions with the background thermal vapor are the dominant loss mechanism from the trap, this nearly two orders of magnitude reduction in background pressure greatly increases the atomic lifetime within the traps from three to four seconds in the MOT chamber to > 1 min in the science cell. This is advantageous as the later stages of cooling take roughly 30 s to complete. Longer possible experimental times after the creation of the condensate is also beneficial.

2.3 Evaporative cooling

Once on the science chamber side we begin cooling once again. Loading the atoms into the magnetic trap warmed them to roughly 1 mK. In our trap the critical temperature where the BEC begins to form is around 200 nK. We use evaporative cooling to cool the atoms the rest of the way. Evaporative cooling works by removing hotter than average atoms. The timescale at which these atoms are selectively removed is chosen to allow those that remain to rethermalize at a lower temperature [49]. This process is continued until just a small fraction of atoms remain and the condensate has formed.

We start cooling on the science side with radio-frequency (rf) evaporation. We apply an rf field which drives a $\Delta m_F = 1$ transition for atoms at a particular magnetic field magnitude. The frequency is chosen to be resonant with atoms far

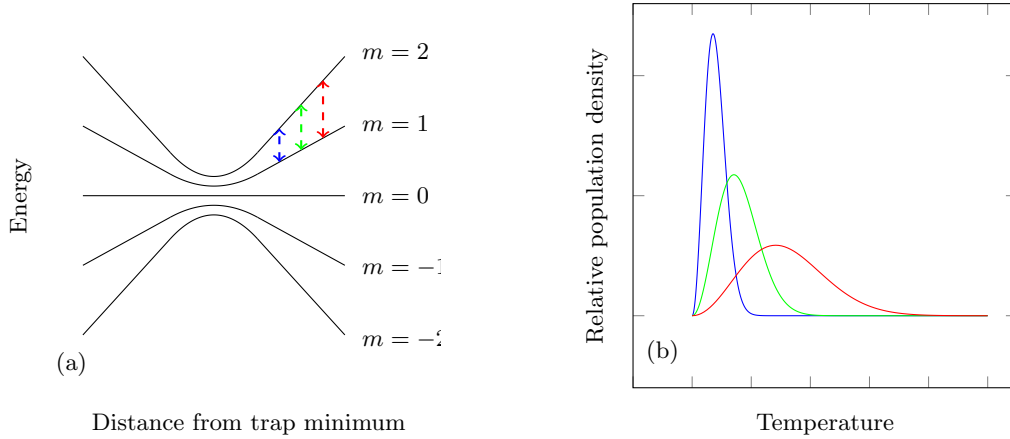


FIGURE 2.2: Cartoon of rf evaporation. By selectively removing the hot atoms and allowing the remaining atoms to rethermalize, the temperature of the remaining atoms is reduced. The avoided crossing at the field zero is achieved by the use of a rotating bias field as outlined in Section 2.4. (a) shows the potential with several rf cuts. (b) shows the normalized Maxwell-Boltzmann distributions following those cuts.

from the trap center where Zeeman shifts are larger. These atoms tend to be the hottest atoms as they are highest in the potential. A snapshot of this process can be seen in Fig. 2.2 where atoms higher in the potential experience a larger Zeeman shift. As atoms are removed and the remaining atoms are subsequently cooled, the rf frequency is swept downward to continue evaporating the hottest remaining atoms. This process works because the dc spherical quadrupole traps only the $m_F \geq 1$ atoms in the $F = 2$ manifold, so after absorbing several rf photons, it is likely that those hot atoms are now in either an untrapped or anti-trapped state. One problem that arises as the atoms cool and begin to spend more time near the trap center is that the m -sublevels are degenerate at the field zero. This degeneracy will need to be dealt with else it becomes a large loss mechanism.

2.4 Time-orbiting potential trap

The atoms' quantization axes are defined by the magnetic field, and only certain m -sublevels are trapped. When coming too close to the field zero, the m -sublevels become degenerate, and the atoms can undergo a spin flip. If the atom ends up in an untrapped or anti-trapped state, it can be lost from the trap without removing excess energy. This becomes the dominant loss mechanism quite quickly and needs to be addressed. This effect is referred to as a Majorana spin-flip [50].

To avoid this loss mechanism, we can move the trap center by applying a separate magnetic bias field. If the applied field is dc, the atoms will simply follow the zero and the Majorana losses will continue at the new, shifted trap center. If however an ac bias is applied at sufficiently high frequency the field zero can be made to move in such a way that the atoms' spins can follow the direction of the bias field but the atoms themselves remain stationary. The range of available frequencies falls between the Larmor frequency of tens of MHz and their center-of-mass motion hundreds of Hz. It is necessary though to use two ac bias fields with a $\pi/2$ phase shift between them to move the field zero in a circle around the atoms. Otherwise, with just a single bias field, the field zero would pass through the atoms every half period and atoms would still undergo the unwanted Majorana spin-flips. This is the foundation of a time-orbiting potential (TOP) trap [51].

There are other ways to remove the field zero, including through the use of field geometry that creates a non-zero field minimum from the beginning [52], or by plugging the hole at the center with a laser tuned to where the atoms are low

field seeking [53]. Our use of the TOP trap solution has additional implications in affecting the optical polarization used in tune-out wavelength measurements, so while a more complicated technique for mitigating Majorana losses, the use of TOP trap is important for our atom interferometry measurements. This will be discussed in detail in Chapter 3.

Let's now take a look at the specifics of this TOP trap and develop a mathematical model for the potential before continuing our discussion on cooling. We use the same dc spherical quadrupole \mathbf{B}_Q as in Eq. (2.2). The full field is

$$\mathbf{B}_{TOP} = \mathbf{B}_0 + \mathbf{B}_Q, \quad (2.4)$$

where \mathbf{B}_0 is the ideal rotating magnetic bias field given by

$$\mathbf{B}_0 = B_0(\sin \Omega t \hat{x} + \cos \Omega t \hat{z}). \quad (2.5)$$

We choose $\Omega_1 = 2\pi \times 12.8$ kHz to fall in the region the atoms cannot physically follow the moving trap minimum but their spins can. \hat{z} is the direction opposing gravity and \hat{y} is the direction in which we do interferometry. We want to calculate the potential created by these fields. This is given simply by the Zeeman effect with the potential $U_{TOP} = g_F m_F \mu_B \langle |\mathbf{B}_{TOP}| \rangle$. Before time averaging, start with the field magnitude.

$$|\mathbf{B}_{TOP}| = \left\{ B_0^2 \left[1 + \frac{B'_Q}{B_0} (-2x \sin \Omega_1 t + 4z \cos \Omega_1 t) + \frac{B_Q'^2}{B_0^2} (x^2 + y^2 + 4z^2) \right] \right\}^{1/2} \quad (2.6)$$

Factoring out a factor of B_0 and Taylor expanding up to 2nd order in the coordinates yields the following

$$|B_{TOP}| \approx B_0 \left\{ 1 + \frac{B'_Q}{B_0} (-x \sin \Omega_1 t + 2z \cos \Omega_1 t) + \frac{B_Q'^2}{2B_0^2} (x^2(1 - \sin^2 \Omega_1 t) + y^2 + 4z^2(1 - \cos^2 \Omega_1 t) - 2xz \sin \Omega_1 t \cos \Omega_1 t) \right\}. \quad (2.7)$$

Taking the time-average of Eq. (2.7) is straightforward. Because our atoms are in $5S_{1/2}|2, 2\rangle$, the potential simplifies to $U_{TOP} = \mu_B \langle |B_{TOP}| \rangle$. Adding in the gravitational potential, we then arrive at

$$U_{TOP} = \mu_B B_0 - mgz + \mu_B \frac{B_Q'^2}{B_0} \left\{ \frac{1}{4} x^2 + \frac{1}{2} y^2 + z^2 \right\}. \quad (2.8)$$

We are left with a harmonic potential with trap frequencies given by

$$\omega_x = \sqrt{\frac{\mu_B B_Q'^2}{2mB_0}}; \quad \omega_y = \sqrt{\frac{\mu_B B_Q'^2}{mB_0}}; \quad \omega_z = \sqrt{\frac{2\mu_B B_Q'^2}{mB_0}}. \quad (2.9)$$

The rotating bias field is turned on rapidly to prevent losses as the field zero traverses the atoms. With the atoms now in a field with a nonzero minimum, we can continue our discussion on evaporation. We use an additional method alongside the radio-frequency method described in the previous section to evaporate the hot atoms. By ramping down the ac bias magnitudes, we can selectively allow the hot atoms near the edge of the trap to undergo Majorana spin flips. This method is commonly referred to as the ‘‘circle of death’’. We lower the bias magnitudes using a series of quasi-exponential linear ramps from a maximum of 21.5 G to 3 G.

rf Stage	f_{Start} (MHz)	f_{Stop} (MHz)	Time Constant (s)	f_{Bottom} (MHz)
1	90	30	6	0
2	30	15	3	0
3	15	12	1.5	0
4	8	2.12	2.75	2.075

TABLE 2.2: rf evaporation timings and frequency ramps. Stages 1 through 3 happen sequentially. The TOP trap is then quickly turned on to 21.5 G before being ramped down to 3 G. Evaporation concludes with stage 4. The discontinuity in rf frequencies between stages 3 and 4 is due to the change in potential from the rotating bias field.

Stage	Time (ms)	Start B_0 (G)	Stop B_0 (G)
TOP On	500	21.5	-
Ramp 1	3000	21.5	15
Ramp 2	6000	15	3

TABLE 2.3: Circle of death bias field ramps. The TOP trap is turned on quickly and left at its maximum 21.5 G for 500 ms. It is then ramped down to 3 G over 9 s in two linear ramps.

We conclude the evaporation stages with a final rf ramp to create the condensate. To summarize the full evaporation process, we started with roughly 2 billion atoms nearly 1 mK and end up with 20000 atoms near 200 nK using a combination of rf and circle of death evaporation stages. The rf evaporation ramps are listed in Table 2.2 and circle of death stages are in Table 2.3. The final rf evaporation stage goes down to 2.12 MHz which is just above the Zeeman splitting between the $m = 1$ and 2 magnetic sublevels.

2.5 Waveguide

After creating the condensate we load the atoms into a much weaker modified TOP trap which reduces atom-atom interactions and improves interferometer performance. This weaker trap will henceforth be referred to as the waveguide. We reduce the strength of the dc spherical quadrupole trap adiabatically to avoid unwanted excitations of the BEC in the trap. As our trap is initially > 100 Hz and it is reduced to just a few Hz, the atoms necessarily pass through 60 Hz. There is a trade off between ensuring adiabaticity and avoiding excitations from being resonant with 60 Hz background fields. The trap frequencies are ramped through 60 Hz at close to 100 Hz/s, so they are reasonably adiabatic and we do not see excessive residual oscillations at the end of the waveguide loading procedure. The crossings occur at different quadrupole magnitudes B'_Q for the trap frequencies in x , y , and z due to their differing dependences on the trap parameters as seen in Eqs. (2.9). Furthermore, we sync the experiment to a 60 Hz signal derived from the AC line in the wall to make any remaining residual oscillations coherent run to run. Residual oscillations in the tighter trap directions are typically difficult to measure due to being quite small, and the oscillation along the weak direction is typically less than the condensate size.

It is in this weaker trap in which we do interferometry. It uses the same rotating bias as in the stronger TOP trap, but a much weaker ac linear quadrupole field to support the atoms against gravity. The coils are contained in a 30 cm

long structure outside the vacuum chamber making the linear quadrupole approximately independent of y ; therefore, the trap is very weak in the y direction. Being independent of y leads to a flat potential along which we can do interferometry with reduced sensitivity to the potential itself [54].

We introduce a small amount of additional confinement in the y direction presently to overcome several limitations of the flat waveguide potential and make interferometric measurements easier. When loaded adiabatically into the flat potential, the atoms are stretched out significantly. This makes imaging more difficult and prone to signal-to-noise issues, and the interferometer becomes more sensitive to misalignment of the optics which can cause the atoms to miss each other when brought back together. The current experiments are not limited by noise in the potential, so simplifying the experimental implementation is desirable.

The waveguide potential is described in detail elsewhere [51, 54] but some of the specifics are necessary within the scope of this work. The potential is generated by the following fields

$$\mathbf{B}_0 = B_0(\sin \Omega_1 t \hat{x} + \cos \Omega_1 t \hat{z}) \quad (2.10)$$

$$\mathbf{B}_1 = B'_1(z\hat{z} - x\hat{x}) \cos \Omega_1 t \quad (2.11)$$

$$\mathbf{B}_2 = B'_2(2y\hat{y} - x\hat{x} - z\hat{z}) \cos \Omega_2 t. \quad (2.12)$$

\mathbf{B}_0 is again the rotating magnetic bias field. The ac linear quadrupole \mathbf{B}_1 supports the atoms against gravity, and \mathbf{B}_2 provides a small amount of additional confinement in the weak direction of the trap. We choose $\Omega_1 \neq \Omega_2$ to avoid unwanted

cross terms, with $\Omega_1 = 2\pi \times 12.8$ kHz and $\Omega_2 = 2\pi \times 1$ kHz. The potential is derived in the same manner as the tighter TOP trap from Section 2.4 by taking the time-average of the magnitude and multiplying by the Bohr magneton μ_B . A reasonable approximation can be found by Taylor expanding the magnitude $|\mathbf{B}|$ and taking the time-average of the result.

$$\langle |\mathbf{B}| \rangle \approx B_0 - \frac{1}{2}B'_1 z + \left(\frac{3B_1'^2}{16B_0} + \frac{B_2'^2}{4B_0} \right) x^2 + \frac{B_2'^2}{B_0} y^2 + \left(\frac{B_1'^2}{16B_0} + \frac{B_2'^2}{4B_0} \right) z^2 \quad (2.13)$$

The result is again a harmonic potential. The trap frequencies are easily found in terms of the individual fields. The fields magnitudes are $B_0 = 21.5$ G, $B'_1 = 30.7$ G/cm, and $B'_2 = 2.5$ G/cm giving trap frequencies of $(\omega_x, \omega_y, \omega_z) = 2\pi \times (5.2, 1.0, 3.0)$ Hz, which are in good agreement with the empirically measured trap frequencies $(\omega_x, \omega_y, \omega_z) = 2\pi \times (5.1, 1.1, 3.3)$ Hz. The small discrepancies are likely due to edge effects from the coils and other non-uniformities in the fields. At $B'_1 = 30.7$ G/cm, the linear quadrupole is set to support only the $m = 2$ atoms against gravity. This ensures a high condensate fraction and will have further implications for the tune-out wavelength measurements which will be discussed in Chapter 3.

2.6 Interferometry

The atomic analogy to an optical beamsplitter is implemented in our interferometer using a series of light pulses which couples via Bragg scattering [55] the zero momentum state $|0\rangle$ with the symmetric superposition of atom packets in the $|\pm 2\hbar k\rangle$ momentum states moving in opposite directions. These pulses are generated by an off-resonant laser which is retro-reflected to form a standing wave that acts as a diffraction grating for the atoms. The atomic beamsplitter is a two photon process with each photon imparting a velocity kick equal to the recoil velocity v_R , which near the D_2 line is $v_R = 5.88$ mm/s. The details of the pulse sequences which generate the atomic beamsplitter can be found in Ref. [56]. I will briefly describe the general process. We start by defining the symmetric superposition of the two momentum states as

$$|S\rangle = \frac{1}{\sqrt{2}} (|2\hbar k\rangle + |-2\hbar k\rangle). \quad (2.14)$$

We can then define a unitary operator U_{split} to represent the splitting pulse sequence mathematically.

$$U_{split}|0\rangle \leftrightarrow |S\rangle \quad (2.15)$$

Using a different sequence of light pulses, it is also possible to create an operation analogous to a mirror.

$$U_{reflect}|\pm 2\hbar k\rangle = |\mp 2\hbar k\rangle \quad (2.16)$$

While the atoms traverse the interferometer path, a phase difference ϕ can

develop between the two packets which we want to measure at the output of the interferometer.

$$|S\rangle \rightarrow |\phi\rangle = \frac{1}{\sqrt{2}} (|2\hbar k\rangle + e^{i\phi}|-2\hbar k\rangle), \quad (2.17)$$

Typically we want the phase difference to be due to some intentional interaction, for example with an external ac electric field applied to just one of the packets as in our tune-out wavelength measurements. Phase noise can be introduced through unwanted variations in either the trapping fields or laser. If the latter are large enough they can wash out the desired interferometer signal.

It is necessary to introduce the antisymmetric superposition of the $|\pm 2\hbar k\rangle$ momentum states to account for this differential phase.

$$|A\rangle = \frac{1}{\sqrt{2}} (|2\hbar k\rangle - |-2\hbar k\rangle) \quad (2.18)$$

It is now possible to rewrite $|\phi\rangle$ in terms of $|S\rangle$ and $|A\rangle$.

$$|\phi\rangle = e^{i\frac{\phi}{2}} \left(\cos \frac{\phi}{2} |S\rangle - i \sin \frac{\phi}{2} |A\rangle \right) \quad (2.19)$$

We recombine using the same splitting operator U_{split} , which transforms $|S\rangle$ to $|0\rangle$ and leaves $|A\rangle$ unchanged.

$$U_{split}|\phi\rangle = \cos \frac{\phi}{2} |0\rangle - i \sin \frac{\phi}{2} |A\rangle \quad (2.20)$$

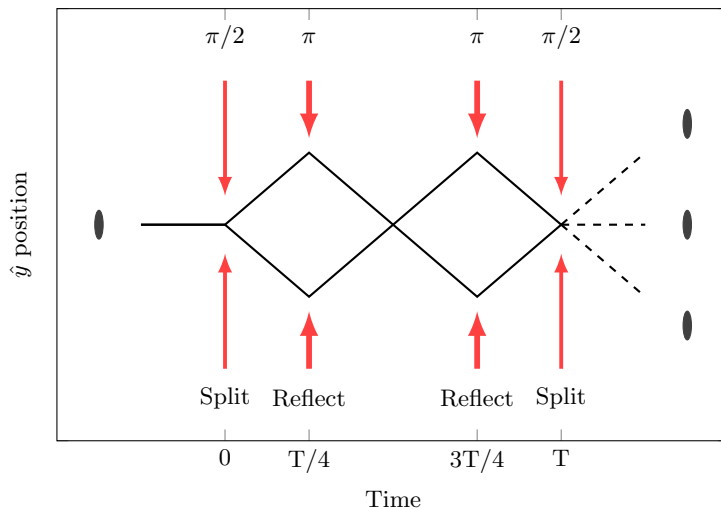


FIGURE 2.3: Here is the timing sequence for the implementation of the interferometer. Splitting and reflection pulses are denoted as $\pi/2$ and π pulses respectively. We use a symmetric trajectory to avoid phase gradients from the magnetic potential degrading interferometer performance.

Here we neglect an overall phase from recombination as it does not affect the interferometer output. We measure the differential interferometric phase by looking at the fraction of atoms that come to rest upon recombination. We refer to this value as N_0/N .

$$\frac{N_0}{N} = |\langle 0 | U_{split} | \phi \rangle|^2 = \cos^2 \frac{\phi}{2} \quad (2.21)$$

The full interferometer is implemented symmetrically. We split the condensate and allow the atoms to propagate for some time $T/4$. We then use the reflect sequence to reverse their velocities. The atoms propagate for $T/2$, with the packets passing through each other. The relatively weak trap limits atom-atom interactions. At time $3T/4$, we again reflect the atoms, and at T we reapply the split sequence to recombine the arms of the interferometer. Finally, we let the packets which did not come back to rest upon recombination separate for 20 ms and measure the output phase via N_0/N .

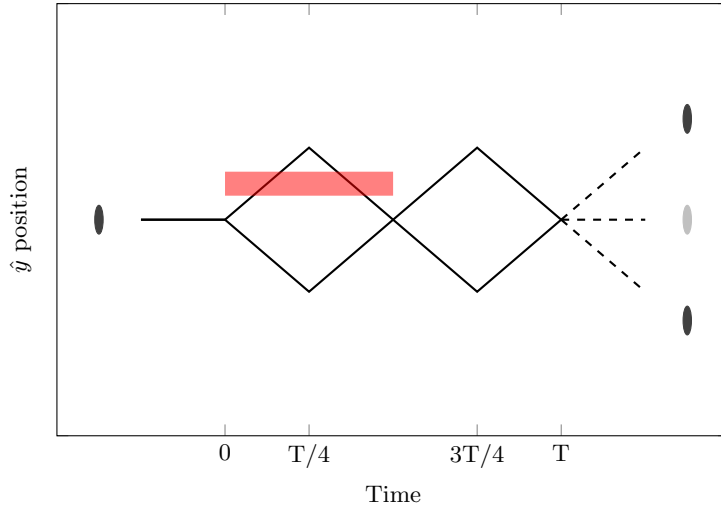


FIGURE 2.4: Pictured is the timing diagram for the tune-out wavelength measurements. The beam is aligned on one packet and turned on for half the interferometer period. The packet traverses the beam twice to double the signal.

We allow the atoms to follow this symmetric path through the interferometer to avoid having unwanted phase gradients develop across the individual packets. If we instead only split, reflected, then recombined the atoms, one side of each packet would spend time higher in the potential as it is not perfectly flat. Additionally, though the atom-atom interactions are low, a phase due to their interactions does accumulate, and atoms on one side of each packet spend more time in the presence of the other packet. Both of these phenomena lead to a nonuniform phase buildup across the packets which will not cancel out upon recombination. As the phase gradient increases, interferometer performance decreases, eventually leading to a fixed output of $N_0/N = 0.5$ regardless of any induced differential phase [54].

Fluctuations during the interferometer, including vibrations in the Bragg retro-reflection mirror affecting the standing wave and variations in the magnetic

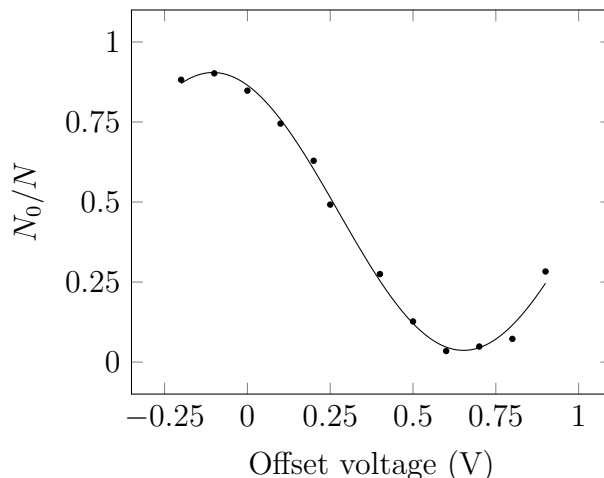


FIGURE 2.5: Phase offset at recombination. We are able to introduce an arbitrary phase difference between the packets upon recombination by adjusting the frequency of the Bragg beam. We typically run with a frequency offset at recombination that gives us $N_0/N = 0.5$ for maximum phase sensitivity. This offset has the added benefit of making the sign of the accumulated phase difference detectable. The offset voltage is applied to the frequency modulation input of the Bragg beam.

potential, also lead to a degradation in interferometer performance as T is increased. Based on empirically measuring the output phase visibility, we have settled on $T = 40$ ms for our typical interferometer. This has the benefit of near unity visibility and a large enough packet separation for use to be able to separately address the two atom packets. Given the recoil velocity of ^{87}Rb , $v_R = 5.88$ mm/s. At 10 ms the packets' maximum separation is $235 \mu\text{m}$. This is roughly five times the size of the condensate. We typically introduce whatever external parameter we seek to measure during the first half of the interferometer and allow the packets to propagate unimpeded during the second half.

Finally, it is possible to write an arbitrary output phase onto the interferometer by changing the location of the nodes and antinodes of the off-resonant standing wave used to create the atomic beamsplitter and mirror analogs. We do

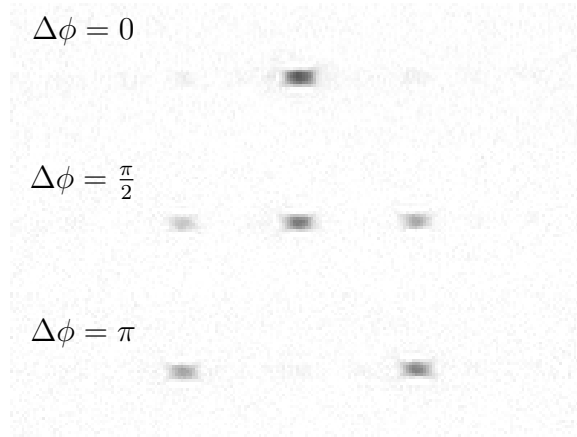


FIGURE 2.6: Selected data from Fig 2.5 showing our ability to add an arbitrary phase shift to the interferometer upon recombination.

this by making small changes to the frequency of the laser generating this standing wave before recombination. The standing wave is created by retro-reflecting the beam after it passes through the chamber. The mirror is roughly 300 mm from the atoms, so given the node spacing of $\lambda/2 = 390$ nm, there are roughly 7.5×10^5 nodes between the atoms and the mirror. That means a fractional change of one part in 7.5×10^5 in frequency between the split and recombination operations is sufficient to cause a 2π change in the interferometric phase. Near 780 nm this is change in laser frequency just 500 MHz. The Toptica DL 100 has a mode-hop free tuning range of 15 GHz, so we can easily sweep out an arbitrary phase. We typically add a $\pi/2$ phase shift to maximize the sensitivity of the interferometer. Additionally this gives us information about the sign of the differential phase, which will prove quite useful in our tune-out wavelength measurements.

2.7 Absorption imaging

We use absorption imaging to detect the number of atoms in the condensate. This works by applying resonant light on the atoms. They absorb some of the probe light and leave a shadow which we image onto a CCD. The spatial extent of this shadow as well as its darkness is used alongside the trap parameters to determine the atom number and temperature. Images of the probe beam's intensity profile are taken with the atoms present and again shortly after the atoms are gone. By normalizing the image with the atoms present to the no atoms image, spatial intensity fluctuations in the probe beam can be removed leaving a clean image. The time between the two images is crucial in determining how clean the resultant image can be.

Our two imaging setups along x and z use different cameras, and the difference in times between images has a noticeable affect on image quality. We use a Princeton Instruments PIXIS 1024 for imaging in the x direction and an Apogee Alta U 8300 in the z direction. Both have been configured for kinetics imaging, which allows for images taken in quick succession. Kinetics imaging works by masking half the CCD. The first image is taken on the open side then it is shifted to the masked side. The second image is subsequently taken and then the full image, containing both images, is read out to the computer. This removes the relatively long download time between images that is necessary when not in kinetics mode. The PI camera can take images with only a 6 ms delay between them when in kinetics mode, whereas the Apogee has a much longer 80 ms delay. The PI camera

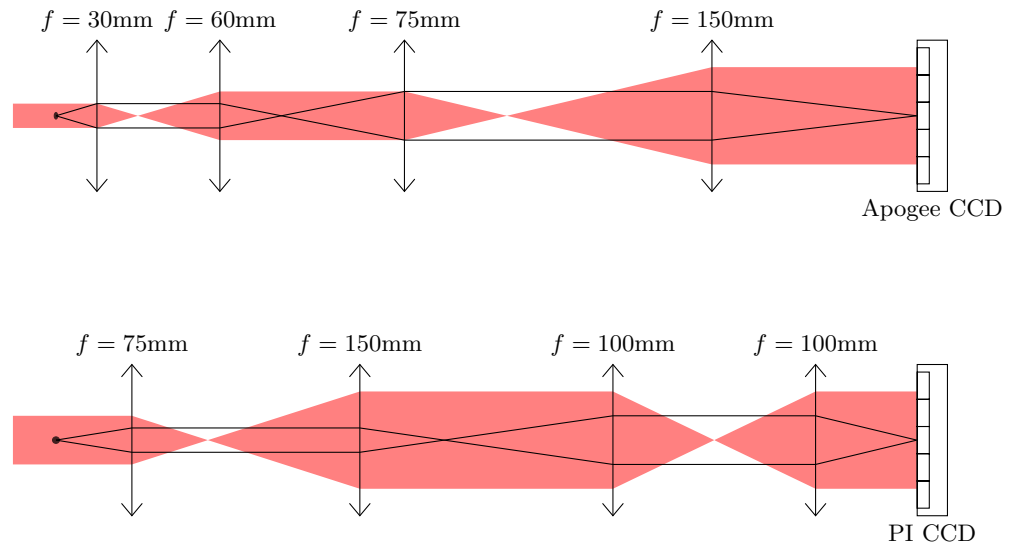


FIGURE 2.7: Pictured is a schematic of the imaging optics for both imaging axes. The black dots are the atoms. The red shaded regions are the probe beam and the black lines are show the atoms' shadow as it passes through the imaging optics. The cameras are quite large and need to be far from the experiment, so multiple telescopes are used to get the image to them. The telescopes are also able to add magnification as necessary. The calibrations are 166 px/mm in the x (side) imaging system and 324 px/mm in the z (vertical) imaging system.

acts as our main camera taking the interferometric data. The Apogee camera is primarily used for alignment of the Stark beam onto the interferometer, so its moderately worse performance is easily tolerated. We take an additional image with the imaging AOM off but the shutter open to account for any leakage light which will affect the images. This background image is subtracted off from both the atoms and no atoms images prior to making the normalized divided image. The image math for this is

$$\text{Divided Image} = \frac{\text{Atoms Image} - \text{Background}}{\text{No Atoms Image} - \text{Background}}. \quad (2.22)$$

Chapter 3

Polarization control

This chapter focuses on developing the techniques necessary for making a measurement of the vector polarizability between the D_1 and D_2 lines in ^{87}Rb . As was detailed in Chapter 1, tune-out measurements are sensitive to the optical polarization of the Stark beam, and in the coming sections we will discuss the specifics of how we both measure and control the optical polarization, a nontrivial task due to the atoms being within a vacuum chamber. Because the atoms are subjected to a continuously rotating magnetic bias field, we must also demonstrate a detailed understanding of the bias field dynamics and our ability to control the field without the benefit of a magnetometer near the atoms.

The techniques presented here should prove useful in other applications as well, particularly in ones that can benefit from the rapid bias field reversal and reduced dependence on environmental fields inherent in TOP traps. Measurements such as parity violation [57], electric dipole moment searches [58], and other

searches for new physics [59] might stand to benefit, and TOP traps have been considered for various types of precision measurements [51, 60–62].

Much of the work presented here appears in Ref. [63] which summarizes our methodologies, but details of the technique which apply specifically to our tune-out wavelength work are expanded here. Sections 3.1 and 3.2 go over the the magnetic field characterization and control. Sections 3.3 through 3.5 go over the measurement of the optical polarization, and finally, Sections 3.6 and 3.7 discuss several current limitations to the polarization control technique.

3.1 Non-ideal magnetic waveguide

As we touched on in Section 2.5, our apparatus uses a modified TOP configuration. As a reminder, the basic trap is formed by a rotating bias field \mathbf{B}_0 and an oscillating linear quadrupole \mathbf{B}_1 . These support the atoms against gravity in the vertical z direction, and they provide approximately harmonic confinement in z and the transverse direction x . An additional spherical quadrupole \mathbf{B}_2 is applied which oscillates at a different frequency and provides adjustable weak confinement in the longitudinal direction y . Again, the trapping potential is given by $\mu\langle|\mathbf{B}_{tot}|\rangle$, where the angle brackets denote a time average and μ is the magnetic moment of the spin state. Our experiments use the $|F, m_F\rangle = |2, 2\rangle$ hyperfine state of ^{87}Rb , so that μ is approximately equal to the Bohr magneton μ_B . In general the time average must be calculated numerically, but if the atoms remain close to the origin, it is accurate to Taylor expand $|\mathbf{B}_{tot}|$ to second order and perform the time average

analytically. Recall Eq. (2.13) where we found

$$\langle |\mathbf{B}| \rangle \approx B_0 - \frac{1}{2}B'_1 z + \left(\frac{3B_1'^2}{16B_0} + \frac{B_2'^2}{4B_0} \right) x^2 + \frac{B_2'^2}{B_0} y^2 + \left(\frac{B_1'^2}{16B_0} + \frac{B_2'^2}{4B_0} \right) z^2. \quad (3.1)$$

Here we assume that Ω_1 and Ω_2 are approximately incommensurate, so that no cross terms survive the time average. Experimentally we use $\Omega_1 = 2\pi \times 12.8$ kHz and $\Omega_2 = 2\pi \times 1$ kHz. Typically we use $B_0 \approx 21.5$ G and we set $B'_1 \approx 30.7$ G/cm such that the linear term in the TOP potential cancels the gravitational potential mgz . In previous iterations of this experimental apparatus the rotating bias field was as high as 24 G, but instabilities due to running the drive electronics near their limits led us to reduce the amplitude. We set $B'_2 \approx 2.5$ G/cm to provide an oscillation frequency $\omega_y \approx 2\pi \times 1$ Hz. The measured ω_x and ω_z confinement frequencies are then approximately $2\pi \times 5.1$ Hz and $2\pi \times 3.3$ Hz, respectively. In comparison, Eq. (2.13) predicts values of 5.2 and 3 Hz. The difference is due to non-uniformity of the bias field B_0 , but this has negligible impact on the work discussed here since it alters the spatial variations of the field but not the field itself at the potential minimum.

A number of other non-idealities do impact the field experienced by the atoms. The rotating bias field components are produced by two separate coils. These coils may not be perfectly orthogonal, their fields may have different amplitudes, and their phase difference may differ from $\pi/2$. In addition a dc background field may be present. All of these effects can introduce time-dependent variations in the

field magnitude and direction at the position of the atoms. The goal here is to characterize and control these effects.

The two components of the bias field are produced by long rectangular coils oriented near $\pm 45^\circ$ from vertical. We express the ideal field components as

$$\mathbf{B}_{0a} = \frac{B_0}{\sqrt{2}} (\hat{x} - \hat{z}) \sin\left(\Omega_1 t - \frac{\pi}{4}\right) \quad (3.2)$$

and

$$\mathbf{B}_{0b} = \frac{B_0}{\sqrt{2}} (\hat{x} + \hat{z}) \sin\left(\Omega_1 t + \frac{\pi}{4}\right) \quad (3.3)$$

where they have the same magnitude B_0 and are $\frac{\pi}{2}$ out of phase with one another.

In reality, the two fields can have different amplitudes which we'll call B_{0a} and B_{0b} .

They might have additional phase offsets ξ_1 and ξ_2 , and their alignment might not be perpendicular. The latter can be dealt with by applying the rotation matrix to their alignment vectors.

$$R(\psi_i) = \begin{pmatrix} \cos \psi_i & -\sin \psi_i \\ \sin \psi_i & \cos \psi_i \end{pmatrix} \approx \begin{pmatrix} 1 & -\psi_i \\ \psi_i & 1 \end{pmatrix} \quad (3.4)$$

for $\psi_i \ll 1$. These complicated but more realistic fields become

$$\mathbf{B}_{0a} \approx \frac{B_{0a}}{\sqrt{2}} R(\psi_1) (\hat{x} - \hat{z}) \sin\left(\Omega_1 t + \frac{\pi}{4} - \xi_1\right) \quad (3.5)$$

and

$$\mathbf{B}_{0b} \approx \frac{B_{0b}}{\sqrt{2}} R(\psi_2) (\hat{x} + \hat{z}) \sin\left(\Omega_1 t - \frac{\pi}{4} + \xi_2\right). \quad (3.6)$$

We expand the sines to separate the dependence on the small variables. The following trigonometric identities are useful.

$$\sin(u \pm v) = \sin u \cos v \mp \cos u \sin v \quad (3.7)$$

$$\cos(u \pm v) = \cos u \cos v \mp \sin u \sin v \quad (3.8)$$

which results in

$$\sin\left(\Omega_1 t - \frac{\pi}{4} + \xi_1\right) \approx \frac{1}{\sqrt{2}} \left((1 + \xi_1) \sin \Omega_1 t - (1 - \xi_1) \cos \Omega_1 t \right) \quad (3.9)$$

and

$$\sin\left(\Omega_1 t + \frac{\pi}{4} + \xi_2\right) \approx \frac{1}{\sqrt{2}} \left((1 - \xi_2) \sin \Omega_1 t + (1 + \xi_2) \cos \Omega_1 t \right). \quad (3.10)$$

We've dropped the 2nd order in ξ_i because $\xi_i \ll 1$. We combine this with the full expressions for the individual bias fields including a small rotation from the ideal orientation to get

$$\mathbf{B}_{0a} = \frac{B_{0a}}{2} \left((1 + \psi_1) \hat{x} - (1 - \psi_1) \hat{z} \right) \left((1 + \xi_1) \sin \Omega_1 t - (1 - \xi_1) \cos \Omega_1 t \right) \quad (3.11)$$

and

$$\mathbf{B}_{0b} = \frac{B_{0b}}{2} \left((1 - \psi_2) \hat{x} + (1 + \psi_2) \hat{z} \right) \left((1 - \xi_2) \sin \Omega_1 t + (1 + \xi_2) \cos \Omega_1 t \right). \quad (3.12)$$

Now we combine the two individual bias fields for the full bias field again dropping the small 2nd order terms.

$$\begin{aligned}
\mathbf{B}_0 &= \mathbf{B}_{0a} + \mathbf{B}_{0b} = \\
&= \left\{ \left(\frac{B_{0a}}{2} + \frac{B_{0b}}{2} \right) \sin \Omega_1 t - \left(\frac{B_{0a}}{2} - \frac{B_{0b}}{2} \right) \cos \Omega_1 t \right. \\
&+ \left(\frac{B_{0a}\xi_1}{2} - \frac{B_{0b}\xi_2}{2} \right) \sin \Omega_1 t + \left(\frac{B_{0a}\xi_1}{2} + \frac{B_{0b}\xi_2}{2} \right) \cos \Omega_1 t \\
&+ \left. \left(\frac{B_{0a}\psi_1}{2} - \frac{B_{0b}\psi_2}{2} \right) \sin \Omega_1 t - \left(\frac{B_{0a}\psi_1}{2} + \frac{B_{0b}\psi_2}{2} \right) \cos \Omega_1 t \right\} \hat{x} \\
&+ \left\{ - \left(\frac{B_{0a}}{2} - \frac{B_{0b}}{2} \right) \sin \Omega_1 t + \left(\frac{B_{0a}}{2} + \frac{B_{0b}}{2} \right) \cos \Omega_1 t \right. \\
&- \left(\frac{B_{0a}\xi_1}{2} + \frac{B_{0b}\xi_2}{2} \right) \sin \Omega_1 t - \left(\frac{B_{0a}\xi_1}{2} - \frac{B_{0b}\xi_2}{2} \right) \cos \Omega_1 t \\
&+ \left. \left(\frac{B_{0a}\psi_1}{2} + \frac{B_{0b}\psi_2}{2} \right) \sin \Omega_1 t - \left(\frac{B_{0a}\psi_1}{2} - \frac{B_{0b}\psi_2}{2} \right) \cos \Omega_1 t \right\} \hat{z}
\end{aligned} \tag{3.13}$$

Here are a few useful definitions to condense the above expression.

$$B_0 \equiv \frac{B_{0a} + B_{0b}}{2} \tag{3.14}$$

$$\Delta \equiv \frac{B_{0a} - B_{0b}}{2B_0} \tag{3.15}$$

We can rewrite B_{0a} and B_{0b} using these.

$$B_{0a} = B_0(1 + \Delta) \tag{3.16}$$

$$B_{0b} = B_0(1 - \Delta) \tag{3.17}$$

We can make further simplifications taking into account that Δ , ξ_i , and ψ_i are all small compared to B_0 .

$$\xi_0 \equiv \frac{B_{0a}\xi_1 + B_{0b}\xi_2}{2B_0} \approx \frac{\xi_1 + \xi_2}{2} \quad (3.18)$$

$$\xi'_0 \equiv \frac{B_{0a}\xi_1 - B_{0b}\xi_2}{2B_0} \approx \frac{\xi_1 - \xi_2}{2} \quad (3.19)$$

$$\psi_0 \equiv \frac{B_{0a}\psi_1 + B_{0b}\psi_2}{2B_0} \approx \frac{\psi_1 + \psi_2}{2} \quad (3.20)$$

$$\psi'_0 \equiv \frac{B_{0a}\psi_1 - B_{0b}\psi_2}{2B_0} \approx \frac{\psi_1 - \psi_2}{2} \quad (3.21)$$

Combined these result in

$$\begin{aligned} \frac{\mathbf{B}_0}{B_0} = & \left[(1 + \xi' + \psi') \sin \Omega_1 t - (\Delta - \xi + \psi) \cos \Omega_1 t \right] \hat{x} \\ & + \left[(1 - \xi' - \psi') \cos \Omega_1 t - (\Delta + \xi - \psi) \sin \Omega_1 t \right] \hat{z}. \end{aligned} \quad (3.22)$$

To this we add the \mathbf{B}_1 quadrupole field from (2.11) and an environmental field $\mathbf{B}_E = B_{Ex}\hat{x} + B_{Ey}\hat{y} + B_{Ez}\hat{z}$ with $|B_{Ei}| \ll B_0$. We then calculate the TOP potential using the same time-averaging procedure as before. We omit the B_2 field since it is an order of magnitude smaller than the B_1 quadrupole. The result is

$$\langle |\mathbf{B}_{tot}| \rangle = B_0 \left\{ 1 + \frac{1}{4}(\Delta - 2\xi + 2\psi)qx + \frac{1}{4}(2 - \xi' - \psi')qz + \frac{3}{16}q^2x^2 + \frac{1}{16}q^2z^2 \right\}, \quad (3.23)$$

with $q \equiv B'_1/B_0$. Here we keep terms to first order in Δ , ψ , ψ' , ξ , ξ' , and B_{Ei}/B_0 , except in the x^2 and z^2 terms where the non-idealities are omitted.

The atoms will be trapped at the minimum of the total potential. Along x the minimum can be found directly as

$$x_0 = -\frac{2(\Delta - 2\xi + 2\psi)}{3q}. \quad (3.24)$$

We take the vertical position z_0 as an independent parameter. We can then express the time-dependent field magnitude at the center, to first order in non-idealities, as

$$|\mathbf{B}_{tot}|(t) = B_0 \left\{ 1 + \frac{1}{2}qz_0 + q_{Ex} \sin \Omega_1 t + q_{Ez} \cos \Omega_1 t + \frac{1}{2}(qz_0 - 2\xi' - 2\psi') \cos 2\Omega_1 t - \frac{2}{3}(\Delta + \xi - \psi) \sin 2\Omega_1 t \right\} \quad (3.25)$$

with $q_{Ei} = B_{Ei}/B_0$. We see that the non-idealities combine to give oscillating contributions to $|\mathbf{B}|$ that have different frequencies and phases. Measuring these different components therefore provides information about the non-idealities, which can then be compensated with the goal of producing a bias field that varies as little as possible. We see that it is not necessary for all the non-ideal parameters to be zero, since the combinations $qz_0 - 2\xi' - 2\psi'$ and $\Delta + \xi - \psi$ appear together. As long as the parameters are adjusted to make $|\mathbf{B}_{tot}|$ constant in time, the net bias field will rotate uniformly as

$$\mathbf{B}_{tot} = B_0 \left(1 + \frac{qz_0}{2} \right) (\hat{x} \sin \Omega_1 t + \hat{z} \cos \Omega_1 t) + B_{Ey} \hat{y}. \quad (3.26)$$

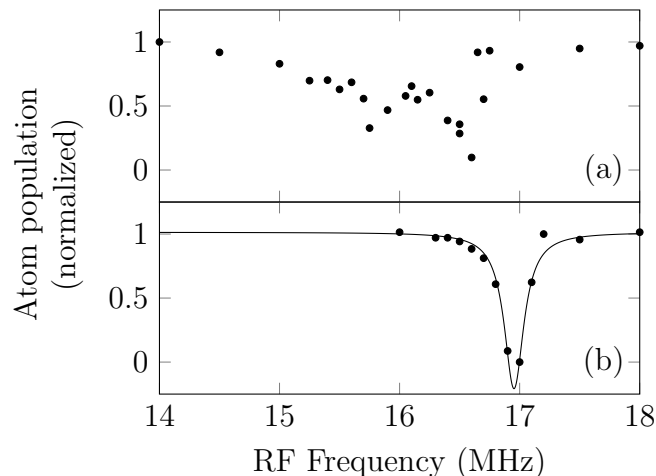


FIGURE 3.1: Radio-frequency spectra of trapped condensate atoms. The vertical axis shows the fraction of atoms remaining in the trap after rf is applied at the indicated frequency. (a) Spectrum obtained using a single long pulse of duration 200 ms. (b) Spectrum obtained using a train of 250 pulses each with $10 \mu\text{s}$ duration. The pulses are synchronized to the 12.8 kHz bias rotation frequency, so that the magnetic field has the same value during each pulse. At the delay time shown, the field magnitude happens to take on nearly its largest value. The curve is a Lorentzian fit.

The amplitude shift due to z_0 is typically unimportant, so we do not attempt to measure or compensate for it.

3.2 Magnetic field control

Information about the magnetic field at the location of the atoms can be obtained by driving the Zeeman transition $m_F = 2 \rightarrow m_F = 1$ using a radio-frequency field. Atoms making the transition are no longer supported against gravity and fall out of the trap. If the atoms form a Bose–Einstein condensate, the thermal broadening of the rf spectrum will be negligible and the character of the spectrum will be determined entirely by the variations in the magnetic field at the trap potential minimum. Figure 3.1(a) shows the spectrum observed when a continuous rf pulse

is applied to an unoptimized trap. The broad and complicated lineshape indicates that the atoms experience considerable variations in the trap field, making the resonant frequency vary over the course of the TOP period.

More detailed information can be obtained by applying a pulsed rf field, with the pulses synchronized to the Ω_1 trap frequency. In this way we obtain a snapshot of the field value at a particular point in the cycle, using the same principle as the stroboscope. Figure 3.1(b) shows the spectrum obtained with a 10 μs pulse duration at a fixed delay with respect to the 80 μs oscillation period. The spectrum is much narrower, with a width close to the 60 kHz transform limit of the pulse. The frequency at which the peak occurs indicates the instantaneous value of the field at that time.

To map out the field amplitude as a function of time, we take a series of spectra such as Fig. 3.1(b) with different time delays between the trap current oscillation and the rf pulses. A typical result is shown in Fig. 3.2(a). We fit such data to a function with the form of Eq. (3.25), where the amplitudes of each term are fit parameters. The solid line in the figure shows the result, which generally fits the data well.

The fitted coefficients indicate how the parameters B_{Ex} , B_{Ez} , q and Δ can be adjusted to make $|\mathbf{B}|$ constant in time. We do not adjust the ψ_i or ξ_i variables. The environmental fields are controlled using a set of bias coils, while q and Δ are set by the quadrupole and bias current amplitudes respectively. Figure 3.2(b) shows a spectral measurement of the field variations after the oscillating components have

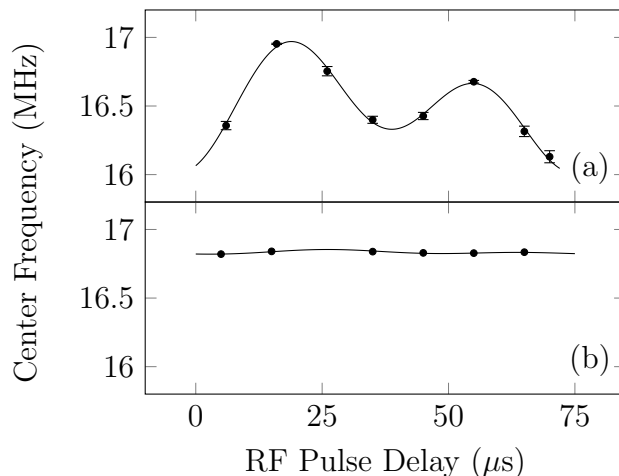


FIGURE 3.2: Time-dependence of the magnetic field magnitude during TOP field oscillation, as measured by the center frequency of spectra such as in Fig. 3.1(b). Error bars are one- σ errors from the fit. Solid curves are fits to the form of Eq. (3.25). (a) Initial variation in a trap using nominal driver current amplitudes. (b) Variation after adjusting the oscillating terms in (3.25) to be zero. The residual oscillation corresponds to field variations of less than 10 mG.

been minimized, showing that the transition frequency remains nearly constant during the bias rotation. Our measurement resolution is 5 mG, and we are able to zero each frequency component to that level. This corresponds to a total rms field variation of about 10 mG.

The rf spectroscopy technique is insensitive to the B_{Ey} component, since it makes only a dc contribution to the field magnitude. However, we want to ensure that the field rotates in the xz plane, so it is necessary to determine and null out the B_{Ey} field as well. A way to achieve this is by applying a dc spherical quadrupole field

$$\mathbf{B}_Q = B'_Q(2z\hat{z} - x\hat{x} - y\hat{y}) \quad (3.27)$$

to the atoms in the TOP trap. We focus on the resulting confinement potential along the y direction, taking $x = z = 0$. Calculation of the time-averaged field

magnitude as in Eq. (3.23) yields

$$\langle |\mathbf{B}| \rangle = B_0 + \frac{B_2'^2}{B_0} y^2 + \frac{B_Q'^2}{2B_0} (y - y_E)^2, \quad (3.28)$$

where $y_E \equiv B_{Ey}/B_Q'$ is the position where the net dc field is zero. The minimum of the resulting potential occurs at position

$$y_0 = y_E \frac{B_Q'^2}{B_Q'^2 + 2B_2'^2} = \frac{B_{Ey} B_Q'}{B_Q'^2 + 2B_2'^2}. \quad (3.29)$$

To find B_{Ey} , we measure the condensate's position while varying B_Q' and fit the results to Eq. (3.29). Typical data are shown in Fig. 3.3(a), along with the fit curve. Figure 3.3(b) shows the values of B_{Ey} obtained from the fit as current through a dc bias coil is varied. The slope of the curve is consistent with the bias coil geometry, and the intercept allows us to determine where B_{Ey} is zero to an accuracy of 7 mG. We used a similar technique observing motion along the z direction, and verified that the trap motion and rf spectroscopy techniques give consistent results for the B_{Ez} component.

The background magnetic fields and rotating bias field show good stability over long timescales without the need for regular adjustments. We observed drifts of less than 10 mG over several months of operation. However, the linear quadrupole amplitude B_1' does drift by about 30 mG/cm over the course of days, making regular adjustments necessary. It is easy to see when B_1' has shifted, because the z position of the atoms changes.

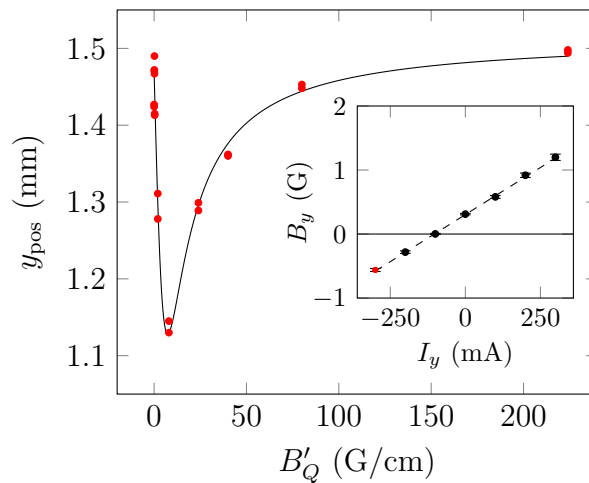


FIGURE 3.3: Using trap motion to determine the B_{Ey} background field. In the main graph, data points are the observed trap positions as the dc gradient B'_Q is slowly varied. The curve is a fit to Eq. (3.29) yielding $B_{Ey} = 0.56(2)$ G. The inset shows measured B_{Ey} values as a function of current I_y through a pair of dc bias coils. The red point corresponds to the data in the main graph.

3.3 Beam alignment

I will briefly discuss the alignment procedure of the Stark beam onto the atoms. There is a minor inconvenience in using a shared optical axis between the Stark beam and imaging axis in that there are different requirements for the spatial profile of the two beams. The imaging probe needs to be collimated at the atoms whereas the Stark beam is focused onto them for maximal phase sensitivity in the tune-out measurements. This is dealt with by including a second lens in the probe beam path before the beam sampler which combines the probe and Stark beams. This lens acts as the first lens in a telescope with the focusing lens for the Stark beam collimating the probe beam. A schematic of this setup can be seen in Fig. 3.4. Polarization maintaining fibers bring both beams to the experiment from a separate laser table.

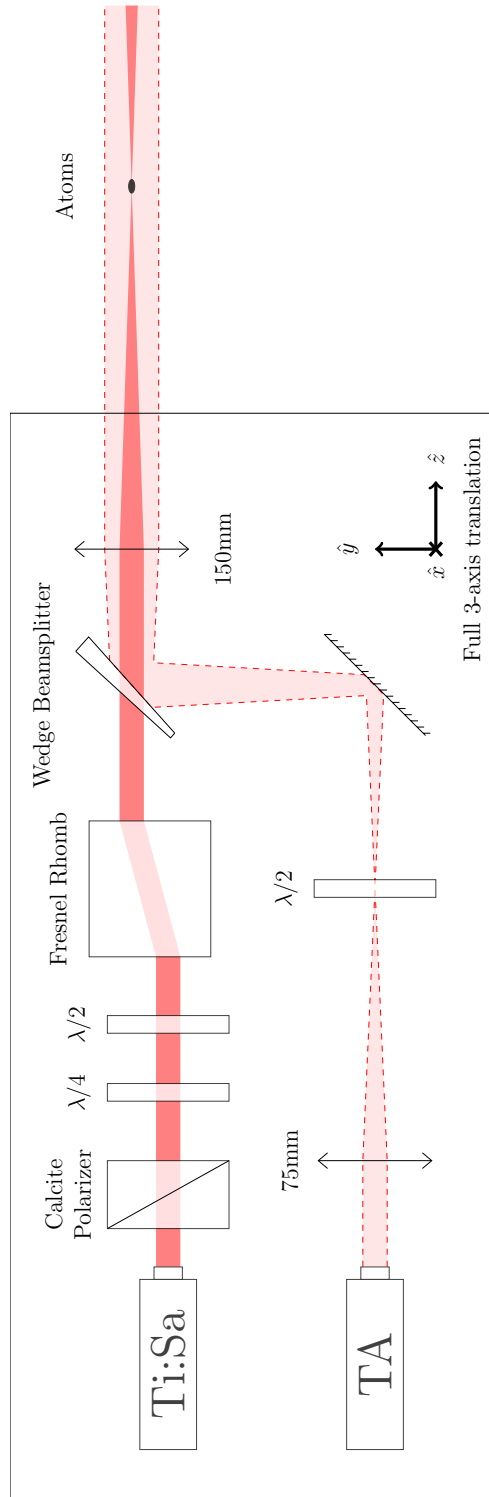


FIGURE 3.4: Pictured are the optics to set the Stark beam polarization and combine it with the imaging probe. These optics are all mounted to a 3 axis translatable stage for quick and easy alignment of the Stark beam on the atoms. Not pictured are three gold steering mirrors. Two are on the stage and one is under the chamber to allow for adjustments of the angle of the Stark beam with respect to the waveguide structure.

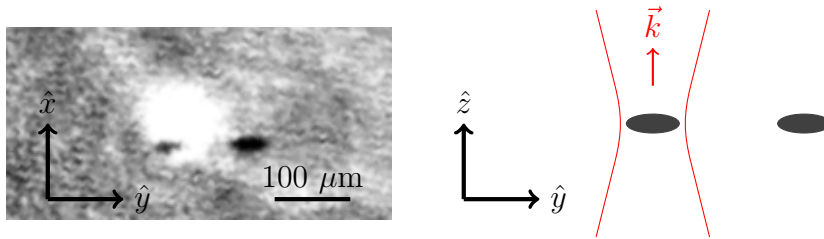


FIGURE 3.5: The image on the left is of the atoms and Stark beam exposed simultaneously. It was taken during the alignment procedure for the interferometer as an example of their relative sizes. The beam is aligned with the location of the atoms 5 ms after splitting, which is at half of their maximum separate. Images of the beam and atoms are not typically taken together as it makes finding the center of each difficult, and the Stark beam can easily saturate the camera. On the right is a general schematic of the beam and interferometer to give further perspective and show our coordinate system explicitly.

These optics are mounted on a translation stage such that the imaging probe and Stark beams are moved in tandem. This prevents large changes to the Stark beam alignment from adversely affecting the probe beam. The translation stage also allows for precise and repeatable alignment of the Stark beam on the atoms. Given the atoms' size of roughly $10 \mu\text{m}$ in their narrowest direction and a beam waist on the Stark beam of $50 \mu\text{m}$, the micrometers on the stage make achieving an initial alignment of better than $10 \mu\text{m}$ easily attainable. This is an improvement in design over the setup used in our scalar polarizability measurements, which lacked the repeatability. Details on that setup as well as the previous work on ensuring run-to-run atom position stability to make this alignment procedure feasible can be seen in Bob Leonard's Thesis [7].

We use two slightly different alignment procedures based on the specific measurement being done. They involve determining the atoms' position and then translating the Stark beam on to them. In both cases, the Stark beam is imaged using the same camera we use with the atoms. It is necessary to significantly

attenuate the beam due to its small beam waist easily saturating and potentially damaging the camera. We add 16 dB attenuation to the output of the Stark AOM drivers, set the analog input to the drivers to only a few percent their maximum, turn the beam on for roughly $4 \mu\text{s}$ when imaging, and finally minimize the beam intensity by rotating a zero-order half-wave plate before a polarizer at the input of the optical fiber.

The two procedures differ only in where the atoms are located when their position is measured. The first procedure is used to measure the polarization of the Stark beam and requires longer interaction times, thus the atoms' position is measured when they are at rest within the trap. The polarization measurement technique will be discussed later in this chapter. The second procedure is used when making tune-out wavelength measurements using the atom interferometer, where only one of the atom packets is exposed to the Stark beam. In this case, the atoms are imaged when they are at half their maximum separation after splitting, roughly $125 \mu\text{m}$. This occurs 5 ms after the splitting sequence. The Stark beam waist is large compared to this distance as it passes through the polarizing optics and vacuum window, so we do not expect any appreciable change in polarization purity between the two positions.

3.4 Optical polarization characterization and control

In addition to having a well-controlled magnetic field, we need to apply a light field with a well known and stable polarization. This is a critical element for our tune-out wavelength studies, and it is important for other precision measurements as well. For our experiments, we need to apply σ^+ polarized light to the atoms with a polarization accuracy better than 10^{-4} .

Two factors make polarization control challenging here. The first is that the bias field at the atoms is rotating, so relative to the quantization axis the light polarization is constantly changing. This can be addressed using the same technique described above for rf spectroscopy, by applying short pulses of light that are synchronous with the magnetic field oscillations. If light polarization $\hat{\mathcal{E}}$ is applied to the atoms, the polarization fidelity can be defined as $F = \langle |\hat{\mathcal{E}}^* \cdot \hat{\sigma}_+|^2 \rangle$, where the angle brackets denote a time average over the direction of the field. We use circularly polarized light travelling along z , with $\hat{\mathcal{E}} = (\hat{x} - i\hat{y})/\sqrt{2}$. The direction of the trap field determines the $\hat{\sigma}_+$ vector as $(\hat{x}' - i\hat{y}')/\sqrt{2}$, for $\hat{x}' = \cos \Omega_1 t \hat{x} + \sin \Omega_1 t \hat{z}$. If the light applied for time $\tau \ll 1/\Omega_1$, centered on $t = 0$, then the time-averaged fidelity is

$$F = 1 - \frac{1}{48} \Omega_1^2 \tau^2. \quad (3.30)$$

For $\Omega_1 = 2\pi \times 12.8$ kHz, this gives a negligible polarization error of 2×10^{-6} at a pulse duration of 120 ns.

The second challenging factor is that optical polarizing elements are not ideal, so the light polarization reaching the atoms will not be perfect. For instance, stress-induced birefringence of the vacuum window introduces polarization errors that are difficult to determine *in situ* [64]. Similarly, waveplate retardances are not exact and can vary with temperature and light wavelength.

The behavior of the polarization can be characterized using the Stokes vector $\mathbf{S} = [S_1, S_2, S_3]$, which can be related to the left- and right-circular polarized electric field components \mathcal{E}_ℓ and \mathcal{E}_r by $S_1 = 2 \operatorname{Re}(\mathcal{E}_r \mathcal{E}_\ell^*)$, $S_2 = -2 \operatorname{Im}(\mathcal{E}_r \mathcal{E}_\ell^*)$ and $S_3 = |\mathcal{E}_r|^2 - |\mathcal{E}_\ell|^2$. The S_0 Stokes parameter is the beam intensity and is here taken to be unity. Further, we normalize $S_1^2 + S_2^2 + S_3^2 = |\mathcal{E}_r|^2 + |\mathcal{E}_\ell|^2 = 1$. When the laser beam passes through a birefringent element with retardance δ and axis at angle α , the effect on \mathbf{S} is given by the Mueller matrix [65]

$$M(\alpha, \delta) = \begin{bmatrix} \cos^2 2\alpha + \sin^2 2\alpha \cos \delta & \cos 2\alpha \sin 2\alpha (1 - \cos \delta) & \sin 2\alpha \sin \delta \\ \cos 2\alpha \sin 2\alpha (1 - \cos \delta) & \cos^2 2\alpha \cos \delta + \sin^2 2\alpha & -\cos 2\alpha \sin \delta \\ -\sin 2\alpha \sin \delta & \cos 2\alpha \sin \delta & \cos \delta \end{bmatrix}, \quad (3.31)$$

such that input \mathbf{S} is transformed to $\mathbf{S}' = M\mathbf{S}$. The fidelity of the output polarization with respect to the initial state is given by

$$F = \frac{1}{2} (1 + \mathbf{S}' \cdot \mathbf{S}). \quad (3.32)$$

In the case of weak birefringence $\delta \ll 1$, the fidelity can be calculated to second order as

$$F \approx 1 - \frac{\delta^2}{4} [(S_1 \sin 2\alpha - S_2 \cos 2\alpha)^2 + S_3^2], \quad (3.33)$$

The error is zero for linearly polarized light aligned to the axis of the retarder, but in general the fidelity decreases by a factor of order δ^2 . A similar error occurs for light passing through a waveplate if δ is interpreted as the birefringence error and \mathbf{S} is the ideal output polarization. We observe typical values of δ to be 5×10^{-2} or greater, which imposes a polarization error on the order of 10^{-3} . It is therefore necessary to correct for these errors.

We prepare the polarization state starting with linear polarization produced by a Glan-Taylor polarizer, with an estimated error below 10^{-5} [66]. The conversion to circular polarization is achieved using a Fresnel rhomb, which is the most stable retarder readily available [67]. Using BK7 glass, the calculated wavelength variation of the retardance is below 10^{-8} rad/nm, and the calculated temperature dependence is about 4×10^{-6} rad/K. We verified experimentally that the retardance of the rhomb is stable at our measurement sensitivity of 10^{-5} .

The retardance of the rhomb is not easily adjustable, so prior to the rhomb we pass the light through two Meadowlark Optics zero-order polymer retarders, one a quarter-wave plate and the other a half-wave plate. Both plates are aligned with their axes close to the incident polarization axis, which limits the sensitivity

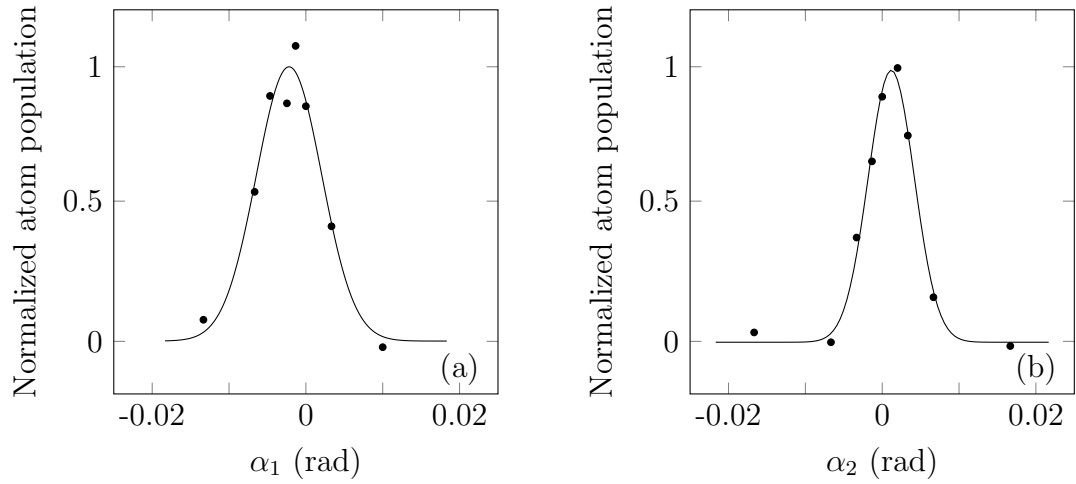


FIGURE 3.6: Data showing optimization of the polarization through changes to (a) the quarter-wave plate and (b) the half-wave plate at 795 nm. The wave plates are set to a precision of better than 10^{-3} rad, which corresponds to a negligible contribution to the current polarization uncertainty.

to retardance errors or drifts. The polarization state exiting the rhomb is then

$$\mathbf{S}_{\text{rhomb}} = \begin{bmatrix} -2\alpha_1 \\ 4\alpha_2 - 2\alpha_1 \\ 1 \end{bmatrix} + O(\alpha^2) \quad (3.34)$$

where α_1 is the angle of the quarter-wave plate and α_2 the angle of the half-wave plate. Any inaccuracies of the rhomb or polarization shifts from subsequent optical elements will give additional small contributions to S_1 and S_2 . We see, however that the two waveplate angles provide sufficient degrees of freedom to compensate for any such contributions, allowing S_1 and S_2 to be tuned to zero. The behavior of the polarizing system can be visualized using the Poincaré sphere, as described in Fig. 3.7.

It is useful to calculate the projection of the light polarization onto the atomic

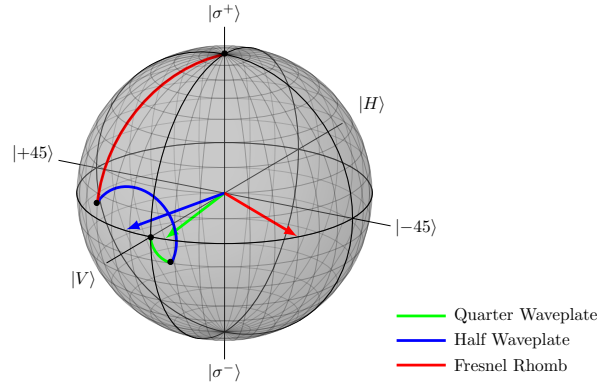


FIGURE 3.7: Poincaré sphere depiction of the polarization control scheme. In the upper diagram, the radial arrows indicate the axis orientation of the two wave plates and the Fresnel rhomb. Deviations from the ideal orientations are exaggerated for clarity. The correspondingly colored traces on the surface show how the Stokes vector evolves as it passes through the elements, starting with vertically polarized light output from the polarizer.

σ^- and π components, in terms of the Stokes parameters and the relative orientation between the laser beam and the magnetic field. The results are

$$|\mathcal{E}_\pi|^2 = \frac{1}{2} (1 + S_1 \cos 2\phi + S_2 \sin 2\phi) \sin^2 \theta \approx \frac{\theta^2}{2} \quad (3.35)$$

$$\begin{aligned} |\mathcal{E}_-|^2 &= \frac{1}{2} (1 - S_3 \cos \theta) - \frac{1}{4} (1 + S_1 \cos 2\phi + S_2 \sin 2\phi) \sin^2 \theta \\ &\approx \frac{S_1^2 + S_2^2}{4}, \end{aligned} \quad (3.36)$$

where the laser beam propagates at polar angles (θ, ϕ) with respect to the field. We see that the π polarization component depends primarily on alignment, while the σ^- term is set by the polarization optics. The polarization error $1 - F$ can be expressed here as $|\mathcal{E}_\pi|^2 + |\mathcal{E}_-|^2$.

This analysis shows that in order to apply pure σ^+ light to the atoms, several conditions must be met. First, the laser beam should be aligned to the z direction of the trap. Second, the laser pulse timing must be set so that the pulse center

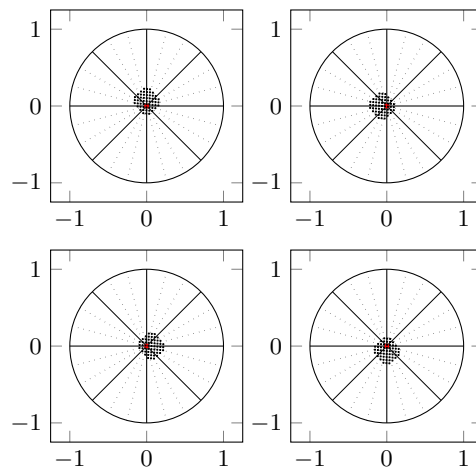


FIGURE 3.8: Results of numerical calculations showing how circular polarization can be achieved despite imperfect wave plates and unknown additional retardance from subsequent optics. The graphs are projections of the Poincaré sphere onto the upper hemisphere, with the red dot showing the σ^+ pole. The grid of black dots represent numerically calculated final polarizations resulting from angular changes spanning ± 5 degrees in the half wave plate and ± 10 degrees in the quarter wave plate. Here the polarization error is modeled as a birefringent element with a retardance of 0.02. The four panes show different orientations of the stray retarder axis. In all cases, the two wave plate angles can be adjusted to compensate for the extra element.

arrives when the trap field points along z . Data showing the timing optimization can be see in Fig. 3.9. Finally, the wave plate angles α_1 and α_2 must be adjusted to compensate for the birefringence of the vacuum window and any other polarization errors. Typical adjustments of the wave plate angles are shown in Fig. 3.6.

In order to set these values precisely, we require a means to characterize the polarization at the location of the atoms. As shown in Fig. 3.10, our ^{87}Rb atoms are trapped in the $|F, m_F\rangle = |2, 2\rangle$ ground state, and we measure the polarization fidelity by tuning the laser to the $5P_{1/2}$ $F = 2$ level. This level has no state with angular momentum projection $m = 3$, so pure σ^+ light does not scatter from the atoms. We can then use the scattering rate as a measure of polarization error, which is very sensitive since scattering even a single photon causes an atom to be

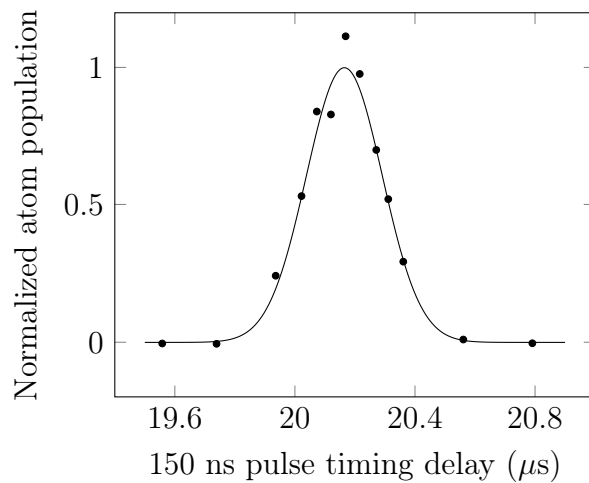


FIGURE 3.9: Data showing optimization of the pulse delay for measuring σ^+ -polarized light. We measure the timing to an uncertainty of 6 ns. Delays are measured using a fast photodiode *in situ* to account for timing offsets in the electronics.

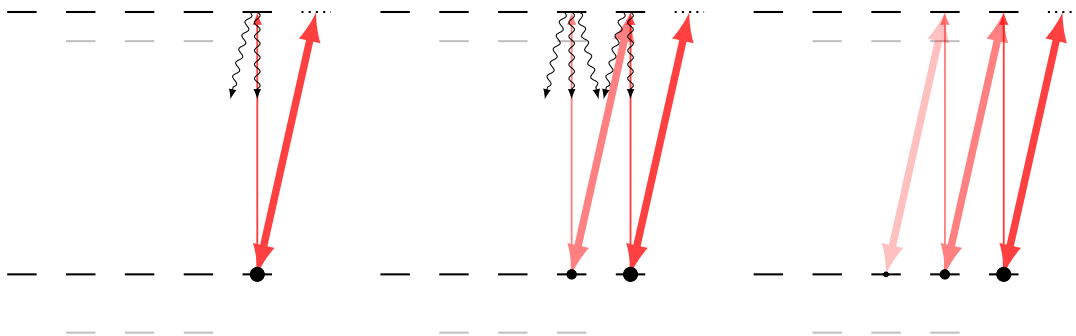


FIGURE 3.10: Level diagrams for polarization testing depicting development of dark state. The atoms are trapped in the $|F, m_F\rangle = |2, 2\rangle$ ground state, where they cannot scatter σ^+ polarized light. Any contamination by π or σ^- light does lead to scattering and loss from the trap; the diagram shows π light for illustration. Because of the scattering, a small population can be temporarily established in the $|F, m_F\rangle = |2, 1\rangle$ state, where the strong excitation to $m'_F = 2$ can destructively interfere with the excitation amplitude from $m_F = 2$. This leads to a suppression of scattering at high optical intensity.

removed from a Bose–Einstein condensate.

To make the measurement, we apply up to 4000 light pulses, each of duration 120 ns and with a period of $2\pi/\Omega_1$. We then measure the fraction of atoms remaining in the trap. We observe the scattering rate for near- σ^+ light to be a complicated function of the total intensity, as seen in Fig. 3.11(a). This is due to

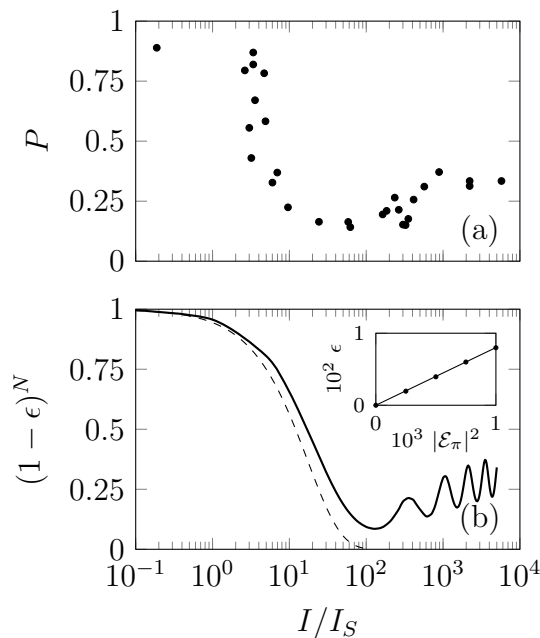


FIGURE 3.11: (a) Experimental measurements of atom loss. Data points show the fraction of atoms P remaining in the trap after 1280 pulses of laser light at the indicated total intensity, relative to the saturation intensity I_S . (b) Numerical calculation of the survival probability after N pulses $(1 - \epsilon)^N$ for $N = 1280$. The solid curve shows the result from the optical Bloch equations for a polarization impurity $\mathcal{E}_\pi = 2 \times 10^{-4}$. The dashed curve shows the behavior that would be expected in the absence of dark-state formation. The inset shows that the loss ϵ depends linearly on the polarization impurity, here calculated at $I = 100I_S$. The slope $d\epsilon/d|\mathcal{E}_\pi|^2$ is approximately 9.5 at the first minimum.

the formation of a dark state. For example, Fig. 3.10 shows a case where a small amount of π light is present. This excites atoms into the $m' = 2$ state, where they can decay to the $m = 1$ ground state and eventually fall out of the trap. However, the atoms do not move significantly during the short laser pulse, so atoms with $m = 1$ undergo a strong excitation to the $m' = 2$ excited state from the σ^+ light. For the proper spin superposition $|\psi\rangle = \sum c_i|m_i\rangle$, the excitation amplitude from $m = 1$ to $m' = 2$ can cancel the amplitude from $m = 2$ to $m' = 2$, leaving the state $|\psi\rangle$ dark.

The trapped atoms experience a Zeeman splitting of about 17 MHz, as seen in

Fig. 3.2. This causes the phases in $|\psi\rangle$ to change in time, so in order to maintain the dark state it is necessary for the optical Rabi frequency of the light to be comparable to the Zeeman splitting. This corresponds to an intensity I of roughly ten times the saturation intensity I_S , which agrees with the measured intensity where the atom loss starts to level out. The Zeeman shift causes substantial dephasing during the $80 \mu\text{s}$ between laser pulses, and measurements confirm that that each pulse has an independent effect on the atoms.

We have analyzed the formation of the dark state by solving the optical Bloch equations for the thirteen relevant atomic states involved [68]. This includes the $F = 2$ ground states, the $F' = 2$ excited states, and the $F = 1$ ground states which can be populated by spontaneous emission. We model the evolution during a single pulse of the light, and determine the fraction of atoms ϵ lost from the initial $m = 2$ state as a function of the intensity components I_i , with $I_\pi, I_- \ll I_+$. Figure 3.11(b) shows how the loss depends on the total intensity, and the shape of the curve agrees reasonably well with the experimental observations. We do not clearly observe the predicted oscillations at high intensity, but it is likely they are washed out by experimental intensity noise. The inset shows that the loss ϵ depends linearly on the polarization impurity.

The formation of the dark state limits the sensitivity of our polarization measurement, since we cannot arbitrarily increase the laser intensity without saturating the loss rate. Instead we experimentally adjust the intensity to locate the value where the loss rate is largest, and then use the Bloch equation model to determine the polarization impurity corresponding to the measured loss. This calibration

depends differently on the π and σ^- components, with the loss rate always being greater for σ^- light. For both polarizations, the loss rate maximum occurs at $I \approx 100I_S$. At that minimum we evaluate the loss per pulse as $\epsilon = \kappa_i |\mathcal{E}_i|^2$, finding $\kappa_\pi \approx 9.5$ and $\kappa_- \approx 18$. To be conservative, we assume that the impurity is all π light to set an upper bound. We are then able to relate the measured atom survival probability $P = (1 - \epsilon)^N$ to the polarization impurity $|\mathcal{E}_\pi|^2$ via

$$|\mathcal{E}_\pi|^2 = \frac{1 - P^{1/N}}{\kappa_\pi}, \quad (3.37)$$

for number of pulses N . For the data of Fig. 3.11(a), we obtain $|\mathcal{E}_\pi|^2 \approx 1.5 \times 10^{-4}$.

Following this procedure, we can optimize the light polarization, pulse timing, and beam direction to minimize the polarization error. For example, Fig. 3.12 shows how the atom loss varies when the delay time of the light pulse is changed. This corresponds to varying the angle between the beam and the rotating field, with $\Delta\theta = \Omega_1 \Delta t$. The polarization error varies like $\theta^2/2$, as expected. The optimum delay time corresponds to the minimum of the curve. After optimizing all parameters in this way, we consistently obtain a loss rate corresponding to $|\mathcal{E}_\pi|^2 = 5 \times 10^{-5}$. Alternatively, if we assume the polarization impurity to be σ^- , we infer $|\mathcal{E}_-|^2 = 3 \times 10^{-5}$.

To confirm this result, we reversed the handedness of the light by rotating the initial polarizer by 90° , and offset the pulse timing by a half-period π/Ω_1 . We then re-optimized the waveplate angles but did not otherwise change the timing or beam pointing direction. We found that the same level of polarization error

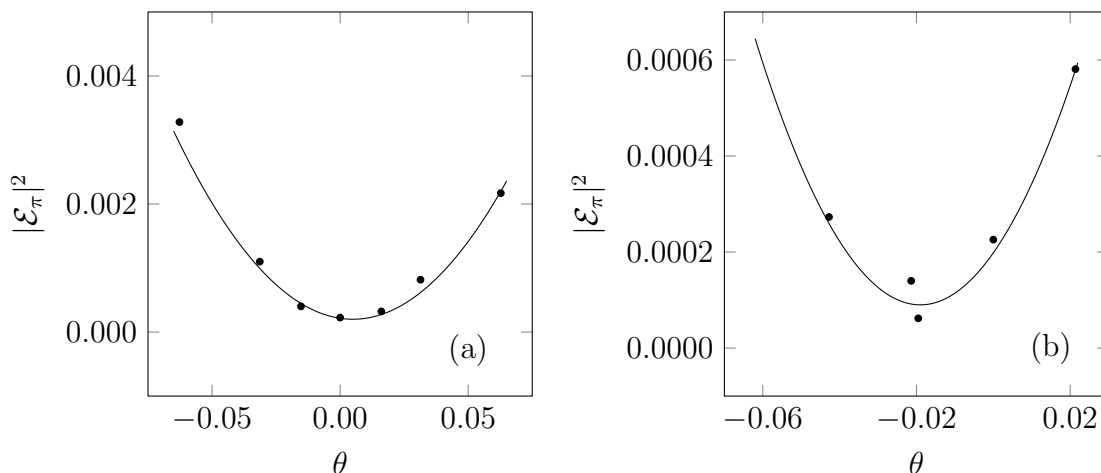


FIGURE 3.12: Dependence of polarization error on beam alignment. (a) Points show the fraction of π polarized light at the atoms, determined as described in the text. The angle θ between the laser beam and the rotating field is varied by adjusting the time t at which the light pulse is centered. The curve is a parabolic fit giving $|\mathcal{E}_\pi|^2 = 0.61(3) \cdot \Omega_1^2 t^2$, in reasonable agreement with the expectation $|\mathcal{E}_\pi|^2 = \theta^2/2$. (b) Similar data where the angle is physically changed using a mirror. The fit gives $|\mathcal{E}_\pi|^2 = 0.29(4) \cdot \Omega_1^2 t^2$.

was obtained. This also verifies the procedures used to zero the B_{Ex} and B_{Ey} environmental field components, since it shows that the bias field does in fact reverse direction after a half period.

3.5 Pulse timing choices

With the optical polarization optimally set and characterized in the lab frame, we can now discuss our method for setting an arbitrary polarization in the atoms' frame. As mentioned before, the effective polarization the atoms experience depends on the relative offset of when we pulse on the Stark light with respect to the instantaneous direction of the rotating bias field. Let us work through how we can use this to control the polarization precisely.

I will go into more detail with regards to the theory and our measurements of the vector polarizability through tune-out wavelength measurements at different polarizations in the next chapter. In the current discussion we just need to be aware of the fact that the tune-out wavelength is polarization dependent, and for our purposes it is dependent almost primarily on the amount of circular polarization in the light. Recall Eq. (1.5) where we expressed the polarizability α in terms of its spherically irreducible tensor components.

$$\alpha = \alpha^{(0)} - v\alpha^{(1)} \quad (3.38)$$

With v defined as

$$v \equiv \frac{1}{2}S_3 \cos \theta, \quad (3.39)$$

where S_3 is the fourth Stokes parameter which explicitly describes the amount of circular polarization, and $\cos \theta = \hat{k} \cdot \hat{b}$. The previous section discussed our control of and ability to measure S_3 . That leaves $\cos \theta$ as the parameter to control the optical polarization by varying when the Stark light is on relative to the time-dependent instantaneous direction of the bias field.

We generate timing pulses which turn the Stark light on and off using a commercial pulse generator (Agilent 81110a) which is triggered externally by a signal derived from the sync output of the function generator (Agilent 33120a) driving the ac linear quadrupole in the waveguide. We control the pulse characteristics by communicating with the pulse generator over GP-IB during each run of the experiment. These pulses are sent to a pair of AOMs which modulate the laser

power. We use two AOMs to increase their extinction ratio from 10^{-3} for a single AOM to close to 10^{-6} . This ensures any residual leakage light does not adversely affect our ability to control the polarization precisely.

Ideally we would like the ability to measure a tune-out wavelength for a particular optical polarization by creating the same effective polarization state using several different pulse configurations to check for possible systematic errors. These errors are primarily due to the background magnetic fields and beam alignment. We can determine how to create these pulse configurations by looking at the phase difference that develops between the two atom packets with one exposed to the Stark light. This phase difference is given by

$$\Delta\phi = \int -\frac{\hbar}{2c\epsilon}\alpha(\omega)I dt. \quad (3.40)$$

At the tune-out wavelength $\Delta\phi = 0$. For this to occur we need $\langle\alpha(\omega)\rangle = 0$. This can be accomplished over two timescales: either instantaneously, where $\alpha(\omega) = 0$, or over the course of a single TOP trap rotation period where $\alpha(\omega)$ time-averages to 0. Our previous scalar tune-out wavelength measurement made use of both, where $\alpha^{(0)} = 0$ and the residual vector polarizability component was time-averaged away over an integer number of TOP trap periods. Here though we are using circularly polarized light to enable us specifically to measure the vector component. To test the validity and precision of this new method, we want to remeasure the scalar tune-out wavelength. This involves ensuring $\int \cos\theta dt = 0$ because we now have $S_3 \neq 0$.

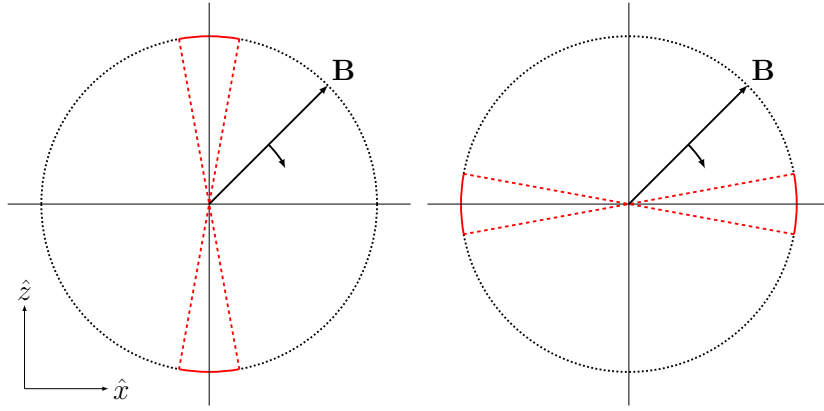


FIGURE 3.13: The two timing diagrams pictured here both produce nominal linearly polarized light as we want to check for systematic effects and verify this polarization control method by comparing with the previous scalar tune-out wavelength near 790 nm. The solid red arcs show when the Stark light would be pulsed on. Here, they are on for two $5 \mu\text{s}$ pulses per TOP trap period, though other pulse widths could be used in principle. The left diagram does so by time averaging equal amounts of σ^+ and σ^- which have opposite sign over the course of a full TOP trap period resulting in $\langle\alpha(\omega)\rangle = 0$. The right diagram shows a configuration that leads to a more instantaneous time-averaging because both components are present at the same time leading to $\alpha(\omega) \approx 0$. Unfortunately due to a relatively large optical dipole force in the case of the former, only the latter can be used in the experiment's present configuration.

Recall Eq. (3.26) from which we get the time dependence of \hat{b} .

$$\hat{b} = \frac{\mathbf{B}_0}{B_0} = \sin \Omega t \hat{x} + \cos \Omega t \hat{z} \quad (3.41)$$

Using this we can find the time dependence of the vector polarizability v

$$v = \frac{1}{2} \int \cos \theta \, dt = \frac{1}{2} \int \hat{k} \cdot \hat{b} \, dt, \quad (3.42)$$

and then by integrating over the pulse duration along with using the fact that the Stark beam is aligned with the rotating bias field such that $\hat{k} \approx \hat{z}$ we are able to



FIGURE 3.14: These images show the effect of the polarization dependent optical dipole force on the atoms. The Stark beam is aligned with the leftmost packet in each image. The three cases shown use in order from top to bottom, σ^+ , $\frac{1}{\sqrt{2}}\pi + \frac{1}{2}(\sigma^+ + \sigma^-)$, and σ^- -polarized light. The laser is tuned near the scalar tune-out wavelength at 790 nm. The unwanted compression and dispersion of the atoms limits our choice of usable timing combinations to achieve a given polarization state. The effect is present in the atoms on the right as well due to a small exposure from the edge of the Stark beam. The integrated exposure in the atoms on the right is less than 1% that of those on the left.

determine the effective polarization based on the timing configuration.

$$v = \frac{1}{2} \int_{t_1}^{t_2} \hat{z} \cdot (\sin \Omega t \hat{x} + \cos \Omega t \hat{z}) dt = \frac{1}{2} \int_{t_1}^{t_2} \cos \Omega t dt. \quad (3.43)$$

It is straightforward from Eq. (3.43) to determine pulse configurations to give the wanted polarization. Figure 3.13 shows two such configurations we used in an attempt to remeasure the scalar tune-out wavelength while looking for systematic biases in our new methodology. Figure 3.13(a) has $\alpha(\omega) = 0$, and Fig. 3.13(b) has $\langle \alpha(\omega) \rangle = 0$. Unfortunately, when attempting a tune-out wavelength measurement using the latter, we observed large unexpected atom loss from the trap which prevented any useful phase measurement.

We would not expect any significant variation in the spontaneous emission

rate due to the significant detuning from resonance, yet in searching for the source of these losses we noticed a dependence on the pulse timings or equivalently the optical polarization. The data first showing this problem were taken near the scalar tune-out wavelength at 790 nm and the effective polarization dependence of these losses can be seen in Fig. 3.14.

An effect related closely to the Stark effect which is similarly dependent on the polarizability is the optical dipole force. It is the likely source of this polarization dependent atom loss. This force is given by [69]

$$\mathbf{F} = \frac{1}{2c\epsilon_0} \alpha(\omega) \nabla I(\mathbf{r}). \quad (3.44)$$

We will see shortly that this is indeed the source of the significant atom loss when $F \neq 0$ due to optical potential heating the condensate. To assess the polarization dependence of this heating, we can look at the impulse J from the optical dipole force applied over the short pulse of Stark light for the pulse timing configurations of interest, and the BEC momentum distribution will be a limit on how large J can be. From these we can estimate the net effect of the optical dipole force and determine the usable pulse configurations.

We start with the beam's characteristics to calculate F . The beam's wavefront is approximated well by a spherical Gaussian, so we can write the intensity I for a laser propagating in the z direction as [70]

$$I(r, z_0) = I_0 \left(\frac{w_0}{w(z)} \right)^2 e^{-\frac{2r^2}{w(z)^2}}, \quad (3.45)$$

where w_0 is the minimum beam waist, $w(z) = w_0 \sqrt{1 + \left(\frac{z}{z_R}\right)^2}$ for the Rayleigh length $z_R = \frac{\pi w_0^2}{\lambda}$, and $I_0 = \frac{2P}{\pi w_0^2}$ is the peak intensity of the beam given a total power P . The Rayleigh length for the beam is on the order of a millimeter. With the condensate size a small fraction of that length and the beam focused on the atoms, we can let $z \approx 0$. We now compute the gradient of the beam intensity using $\nabla = \frac{\partial}{\partial r} \hat{r} + \frac{\partial}{\partial z} \hat{z}$ in cylindrical coordinates. The only non-negligible component is in the r direction, so we will neglect the z direction.

$$\nabla_r I(r, 0) = -\frac{4I_0}{w_0^2} r e^{-\frac{2r^2}{w_0^2}} \quad (3.46)$$

Averaging the intensity gradient over half the condensate size, 0 to L , gives an estimate for the net compression force on the atoms. Integrating over half the condensate can give us a reasonable estimate because during tune-out wavelength measurements, the atoms are moving through the beam anyway and will experience roughly 150 pulses. If the optical dipole force is weak enough that the effect of a single pulse of light is small, there will be little net effect on the atoms after fully passing through the conservative potential. If however the optical dipole force is strong, repeated pulses will cause the atoms to be lost from the condensate before any time-averaging of the optical dipole force can happen.

The estimate for the spatially-averaged intensity gradient is

$$\begin{aligned}\overline{\nabla_r I}(r, 0) &= \frac{1}{L} \int_0^L \nabla I(r, 0) dr = -\frac{4I_0}{w_0^2 L} \int_0^L r e^{-\frac{2r^2}{w_0^2}} dr \\ &\approx -\frac{4PL}{\pi w_0^4}\end{aligned}\quad (3.47)$$

which we can now use in calculating the impulse J .

$$J = \int F(t) dt \approx \frac{1}{2c\epsilon_0} \overline{\nabla_r I}(r, 0) \int \alpha(t) dt \quad (3.48)$$

The general forms of $\alpha^{(0)}$ and $\alpha^{(1)}$ are found in Section 1.3, and we worked out the time dependence of v in earlier in this section. We found $v(t) = \frac{1}{2} \cos \Omega_1 t$ with the optical polarization adequately circularized in the lab frame. Putting these together yields

$$\begin{aligned}J &= -\frac{2PL}{\pi c\epsilon_0 w_0^4} \int_{-\tau/2}^{\tau/2} \left(\alpha^{(0)}(\omega) - \frac{1}{2} \cos \Omega_1 t \alpha^{(1)} \right) dt \\ &= -\frac{2PL}{\pi c\epsilon_0 w_0^4} \left(\alpha^{(0)}(\omega) \tau - \frac{1}{2\Omega_1} \alpha^{(1)}(\omega) \sin \Omega_1 t \Big|_{-\tau/2}^{\tau/2} \right).\end{aligned}\quad (3.49)$$

Two pulse sequences we want to compare both create linearly polarized light. One uses timings such that the polarization is near the equator of the Poincaré sphere and the other uses equal parts σ^+ and σ^- . These two configurations would allow us to assess possible systematics in our polarization control technique by looking at the scalar tune-out wavelength measurement near 790 nm where $\alpha^{(0)}(\omega) = 0$ and seeing whether it shifts between the two sequences. The impulses

from these sequences are

$$|J_{\pm}|_{v=0} \approx \frac{PL\alpha^{(1)}(\omega)}{\pi c\epsilon_0 w_0^4} \tau \quad (3.50)$$

for polarizations near the poles of the Poincaré sphere and

$$|J_{\pi}|_{v=0} = 0 \quad (3.51)$$

near the equator.

We want to compare the nonzero $|J_{\pm}|_{v=0}$ impulse with the BEC momentum distribution Δp_r , which in the xy plane is given by

$$\Delta p_r = \frac{\hbar}{L_r}, \quad (3.52)$$

In the experiment we use $P \approx 100$ mW, $w_0 = 45$ μm , and $\tau = 5$ μs . The condensate size L_r can be estimated using the Thomas-Fermi approximation.

$$L_r = \left(\frac{15Na\hbar^2}{m^2\omega_r^2} \right)^{1/5} \quad (3.53)$$

Here, $N \approx 15000$ is the number of atoms, the scattering length is $a = 5.77$ nm, m the mass, and $\omega_0 = (\omega_x\omega_z)^{1/2} \approx 2\pi \times 4.2$ Hz is the geometric average of the TOP trap oscillation frequencies in the plane of the beam focus. Combining these yields $L \approx 10$ μm . $\alpha^{(1)}(\omega) \approx 24500$ au over the full range of available tune-out wavelengths with variations of only about 3% so it can be taken as a constant in this estimation. Plugging these in yields $|J_{\pm}|_{v=0} \approx 1.2 \times 10^{-28}$ kg·m/s, and

$\Delta p \approx 10^{-29}$ kg·m/s. The order of magnitude difference between the two shows that we can expect a single pulse of σ^\pm -polarized Stark light to have a large effect on the condensate near the scalar tune-out wavelength, therefore our choice of timings to generate a particular polarization are limited to those which have $\alpha(\omega) \approx 0$. We also expect from this timing constraint that there will be an effective maximum pulse width for each particular polarization.

The other relevant polarization and related pulse configuration to consider generates σ^- -polarized light in the atoms' frame. The tune-out wavelength for this polarization is at one extreme of the tuning range near 785 nm. At this tune-out wavelength, $v \approx 0.5$, therefore we have $\alpha^{(0)}(\omega) - 1/2\alpha^{(1)}(\omega) \approx 0$. If we follow through the same calculation we did for near the scalar tune-out wavelength at 790 nm we arrive at

$$|J_+|_{v=1/2} \approx \frac{PL\alpha^{(1)}(\omega)}{\pi c \epsilon_0 w_0^4} \frac{\Omega_1^2 \tau^3}{24}. \quad (3.54)$$

Using the same values from before, we get $|J_+|_{v=1/2} = 8 \times 10^{-31}$ at $\tau = 5 \mu\text{s}$. This is well below Δp_r , and our tune-out wavelength data presented in the next chapter show that indeed there is no unwanted effect on the atoms at this polarization due to the optical dipole force.

Because we are ultimately left with only the pulse timing configurations which have $\alpha(\omega) \approx 0$, we are unable to check directly for systematics such as from nonzero background bias fields using the tune-out wavelength measurements and must settle with using the pulsed rf spectroscopy, trajectory, and polarization measurement techniques outlined in Section 3.2. For the time being, this is likely

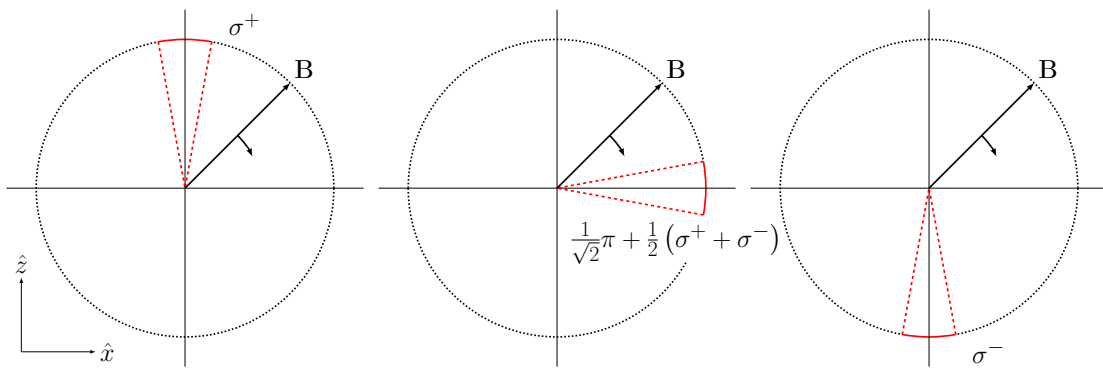


FIGURE 3.15: Here are visualizations for the pulse timings of 3 optical polarization configurations. Each pulse train is synced to the TOP trap with each individual pulse represented by the solid red arcs roughly $5 \mu\text{s}$ long. Pictured are when the magnetic field and k-vector are aligned giving σ^+ -polarized light on the left, when they are perpendicular which gives equal parts σ^+ and σ^- which results in linearly polarized light in the center, and when they are oppositely aligned giving σ^- -polarized light on the right. Other timings between those shown are also used for arbitrarily set elliptical polarizations.

acceptable. This will be touched on further in Section 4.3 when discussing the error budget in our tune-out wavelength measurements. We've settled on using trains of single pulses which are $5 \mu\text{s}$ long for the current measurements. This pulse length does not lead to too large an optical dipole force while maintaining a reasonable rate of phase accumulation within our desired wavelength tuning range.

Finally, we can estimate the maximum pulse width for the timing configuration generating $v \approx 0.5$ using Eq. (3.54). We find $\tau_{max} \approx 12 \mu\text{s}$ gives an impulse roughly equal to the condensate momentum distribution. This shows that there is likely room for potential improvement through the use of a longer pulse, though the longer pulse will change our sensitivity to some of the experimental parameters, primarily the z position. Care therefore needs to be taken in reverifying that everything is optimized and included in the error analysis if longer pulses are used in the future.

3.6 Timing error

A consequence of the large dipole force limiting available pulse configurations for a particular polarization is a larger than anticipated sensitivity to the timing of Stark pulses, particularly when not near the pole of the Poincaré sphere (i.e. near pure σ^+ or σ^-). We would have liked the ability to use several combinations of pulses configurations some with more time-averaging to search for and minimize several systematic errors.

Recall Eq. (3.43) showing $v \approx \frac{1}{2} \cos \Omega_1 t$ for a sufficiently short pulse. The error in the tune-out wavelength due to timing errors goes as

$$d\lambda \approx dv \times 10 \text{ nm} = \frac{1}{2} \Omega_1 dt \sin \Omega_1 t \times 10 \text{ nm}, \quad (3.55)$$

where it is dv multiplied by the 10 nm range in available tune-out wavelengths between the D_1 and D_2 lines. The tune-out wavelength is approximately linear with respect to polarization in this range. Near the poles of the Poincaré sphere, timing errors come in at second order, whereas near the equator, they come in at first order. This has significant implications for the precision at which we can set the different polarizations given the timing accuracy of the Stark beam switching electronics.

The largest timing uncertainty comes from the Agilent 81110A pulse generator. We use a Newport model 1621 fast photodiode to monitor the Stark pulse characteristics and determine v *in situ*. Jitter in the pulse generator's internal

Source	Spec error (ns)	Measured error (ns)	$d\lambda_0 _\pi$ (pm)
5 μ s pulse	5	3	1.2
150 ns pulse	1	2	0.8
Jitter	8	12	4.8
Minimum step size	50	50	20

TABLE 3.1: The specified timing errors are converted from the Agilent 81110A pulse generator specifications using the TOP trap period of 78.125 μ s. The measured timing errors are converted to a tune-out wavelength error using Eq. (3.55).

clock as well as its 3.5 digit resolution introduce uncertainties we need to consider. Table 3.1 contains the manufacturers specifications for the pulse generator and the results of our *in situ* measurements. Included as well are the uncertainties timing errors introduce to the scalar tune-out wavelength. As a result of these uncertainties, we will likely be unable to precisely measure tune-out wavelengths with polarizations not near σ^\pm in the current experimental setup. In the next chapter we will discuss several measurements impacted by this timing error and what can be done to overcome this limitation.

Despite these shortcomings, we will attempt tune-out wavelength measurements at a variety of polarizations. We measure the pulse characteristics in a given tune-out wavelength measurement to calculate the effective polarization and determine the timing error. These pulse measurements account for variations in the timing response of the pulse generator. The largest variation is the 50 ns finite step size, which would result in a large systematic bias if ignored. Additionally, the pulses exhibit an asymmetric profile as can be see in Fig. 5.1. The intensity varies by a few percent over the 5 μ s pulse. This is a large enough effect to significantly bias tune-out wavelength measurements for some polarizations, so a correction

must be applied. By integrating the pulse and finding its center of mass, we find that a 28(4) ns correction is needed. This asymmetry is likely due to temperature and capacitive effects in the AOMs which generate the pulses. A different switching setup using an EOM might overcome this issue without the need for a timing correction. That prospect will be discussed further in Section 5.2.

3.7 Wavelength dependence

There is one final note to make regarding the purity and stability of the optical polarization of the Stark beam. With the unwanted polarization components reduced to $|\mathcal{E}_\pi|^2 + |\mathcal{E}_-|^2 = 5 \times 10^{-5}$ at the D_1 resonance, we must consider the wavelength dependence of the polarizing and nominally non-polarizing optics as we will attempt to measure tune-out wavelengths spanning 785 nm - 795 nm.

The optics with the largest unaccounted for effect on the polarization are three gold mirrors used to steer the beam and periscope it down to table level. There are large phase changes for S and P polarizations upon reflection, and these phases vary with wavelength. The reason these mirrors are necessary in the current experimental apparatus is that the large dc magnetic quadrupole coils used to transport the atoms from the MOT side of the apparatus to the science side limit optical access. The other optics affect the polarization through the index of refraction. In N-BK7 there is a negligible change over the 10 nm tuning range [64].

To look into the effect of the mirrors on our tune-out measurements, we start with a simple model of a single mirror between crossed polarizers. By tuning the wavelength over our range of interest and looking at the extinction ratio, we can measure the difference in phase shift between the two polarization components directly. We align the polarizers near $\pm 45^\circ$ for maximum phase sensitivity. Start by considering the theoretical phase shift based on the mirror's properties. We will define the Jones vectors for the polarization components as

$$|H\rangle = \begin{pmatrix} 1 \\ 0 \end{pmatrix} \quad (3.56)$$

and

$$|V\rangle = \begin{pmatrix} 0 \\ 1 \end{pmatrix}. \quad (3.57)$$

The Jones matrices for a linear polarizer at $\pm 45^\circ$ is given by

$$U_{\pm 45^\circ} = \frac{1}{2} \begin{pmatrix} 1 & \pm 1 \\ \pm 1 & 1 \end{pmatrix}. \quad (3.58)$$

The mirror is also not perfectly reflecting, but we will start by just considering changes in phase to get a qualitative picture of the wavelength dependence. We will add back in the non-unity reflectances later in this section. The mirror's Jones matrix is

$$U_m = \begin{pmatrix} 1 & 0 \\ 0 & e^{i\phi} \end{pmatrix}, \quad (3.59)$$

neglecting any overall common phase. The second linear polarizer is aligned at 90° from the first polarizer and the extinction ratio is measured at the output. The change in the polarization purity $|\mathcal{E}_{45^\circ}|^2$ as the wavelength is varied is then

$$d|\mathcal{E}_{45^\circ}|^2 = |\langle V|U_m U_{45}|H\rangle|^2 = \sin^2 \frac{1}{2} (\phi - \phi_0) \quad (3.60)$$

for $\phi =$ mirror phase at λ , and $\phi_0 =$ mirror phase at 795 nm.

We compare this to the experimental setup where a less well-known but nearly circular polarization state is incident on the three mirrors. The circular polarization Jones vectors are defined as usual as

$$|LCP\rangle = \frac{1}{\sqrt{2}} \begin{pmatrix} 1 \\ i \end{pmatrix} \quad (3.61)$$

and

$$|RCP\rangle = \frac{1}{\sqrt{2}} \begin{pmatrix} 1 \\ -i \end{pmatrix} \quad (3.62)$$

Let U_0 be the matrix describing the three mirrors at 795 nm and $U_1(\lambda)$ is the matrix at some other wavelength λ . We have

$$|LCP\rangle = U_0|\psi_0\rangle, \quad (3.63)$$

where $|\psi_0\rangle$ is the input state we set at 795 nm. We then want to know what happens at 785 nm. Let $|\psi_1\rangle$ be the output state.

$$|\psi_1(\lambda)\rangle = U_1(\lambda)|\psi_0\rangle \quad (3.64)$$

We can then write

$$|\psi_0\rangle = U_0^{-1}|LCP\rangle, \quad (3.65)$$

which leads to

$$|\psi_1(\lambda)\rangle = U_1(\lambda)U_0^{-1}|LCP\rangle. \quad (3.66)$$

We have models for U_0 and U_1 and can work out the purity $|\mathcal{E}_-|^2$ for $|\psi_1(\lambda)\rangle$.

As we are just considering the effect of the mirrors on the polarization, U_0 is given by

$$U_0 = \begin{pmatrix} 1 & 0 \\ 0 & e^{3i\phi_0} \end{pmatrix}, \quad (3.67)$$

whose inverse is

$$U_0^{-1} = \begin{pmatrix} 1 & 0 \\ 0 & e^{-3i\phi_0} \end{pmatrix}, \quad (3.68)$$

Similarly the mirrors at λ give

$$U_1 = \begin{pmatrix} 1 & 0 \\ 0 & e^{3i\phi} \end{pmatrix}. \quad (3.69)$$

Putting all of this together yields

$$|\psi_1(\lambda)\rangle = \begin{pmatrix} 1 & 0 \\ 0 & e^{3i(\phi-\phi_0)} \end{pmatrix} |LCP\rangle, \quad (3.70)$$

which results in a change in the polarization purity of

$$d|\mathcal{E}_-|^2 = |\langle RCP|\psi_1\rangle|^2 = \sin^2 \frac{1}{2}(3(\phi - \phi_0)) \quad (3.71)$$

Again ϕ = the change in phase difference between S and P upon reflection at λ , and ϕ_0 = is at 795 nm. We can see that Eqs. (3.60) and (3.71) are identical in form differing only in the total phase due to the three mirrors in the experimental setup versus one in the test setup. This means that the simple model can be used effectively to estimate the wavelength dependent change in the polarization due to the mirrors.

This calculation can be repeated with non-unity reflectances $R_i = |r_i|^2$, where r_S and r_P are the the reflectance amplitudes for S and P polarizations respectively.

The Jones matrix for the three mirrors becomes

$$U_0 = \begin{pmatrix} r_s(\lambda)^3 & 0 \\ 0 & r_p(\lambda)^3 e^{3i\phi(\lambda)} \end{pmatrix}. \quad (3.72)$$

For the reflectances r_s and r_p . The rest of the derivation is the same as above.

The result is

$$d|\mathcal{E}_-|^2 = \frac{1}{4}(a^6 + b^6 - 2a^3b^3 \cos(3(\phi - \phi_0))) \quad (3.73)$$

where $a = r_s(785 \text{ nm})/r_s(795 \text{ nm})$ and $b = r_p(785 \text{ nm})/r_p(795 \text{ nm})$. The simple model of a single mirror between crossed polarizers can be shown to have the same form. We can therefore measure the change in polarization purity in a more accessible and simple setup to assess the polarization dependence of the mirrors in the actual experimental setup. We empirically measured $d|\mathcal{E}_{45^\circ}|^2 = 5 \times 10^{-4}$ over 10 nm in the experimental setup. This is more than an order of magnitude higher than the polarization purity $|\mathcal{E}_-|^2$ at 795 nm. When we compare this to the change in polarization using the phase and reflectance variations from the mirrors' datasheets, we find $d|\mathcal{E}_{45^\circ}|^2 = 2 \times 10^{-5}$ [71, 72]. Though this is significantly smaller than what we measured, it is too high to tolerate in the experiment.

A possible explanation for this difference in estimated versus measured change in polarization is that correcting for the relatively large $\sim \pi/6$ phase difference between S and P due to the mirrors leads to a larger variation in polarization than is estimated here. Using the wave plates to correct for this phase means they are further from their fast and slow axes than they would otherwise be when correcting for just the smaller phase shifts from the Fresnel rhomb and chamber window. The polarization purity is then more sensitive to the wave plate wavelength dependences. Their retardances scale with wavelength as

$$\delta_{\lambda/4} = \frac{\pi \lambda_0}{2 \lambda} \quad (3.74)$$

and

$$\delta_{\lambda/2} = \pi \frac{\lambda_0}{\lambda} \quad (3.75)$$

given their design wavelength λ_0 . The variation in retardance over 10 nm is at the few percent level. While this is tolerable if the wave plates are within a few degrees of their fast or slow axes, this large change in retardance quickly leads to excessive polarization variations as the angles increase.

We tested the polarization components independently of the full experimental setup to estimate their performance. We found that when making corrections for smaller birefringences on the order of the chamber at below the 10^{-3} level, the polarization purity remained stable to better than 10^{-5} over 10 nm. Therefore in the absence of the mirrors, it is likely that the full optical setup will not exhibit the large variations we currently see.

The imperfect nature of the mirrors and the increase in wavelength sensitivity makes precision measurements of tune-out wavelengths spanning the full 10 nm tuning range difficult in the current experimental implementation. In the next chapter we will discuss the tune-out wavelength measurements themselves as well as our efforts to overcome these significant polarization variations across the available tuning range. I will also discuss in Section 5.2 updates to the optics and beam alignment infrastructure for use in future iterations of this experiment which will remove the need for these mirrors and make the polarization more stable.

Chapter 4

Tune-out wavelength measurements

In this chapter we will discuss the preliminary results of a vector polarizability measurement implemented in our atom interferometer. Section 3.5 detailed our ability to nearly arbitrarily set the optical polarization by using circularly polarized light and varying the relative timing of the Stark interrogation beam and the rotating bias field in the TOP trap. We will put this to use to measure how the tune-out wavelength depends on the polarization. As mentioned in Chapter 1, what we really hope to get out of these measurements is access to previously unmeasurable contributions to the polarizability. These include individual higher-lying dipole matrix elements which are infeasible to measure due to complicated decay paths. There is also the “tail” from the sum to the continuum, and finally the core contribution α_c .

The tail contributions are not fully accessible from this work at the level of precision needed for the atomic parity violation analysis. Tune-out wavelength

measurements near the $6P$ states will be necessary as well before the experimental precision can approach that of the current theoretical estimates for the tail and core-valence contributions. Despite this limitation, the results presented here do represent the first experimental constraint on the separated $n'P_{1/2}$ and $n'P_{3/2}$ tail contributions and as such begin informing these difficult theoretical estimates. Future tune-out wavelength measurements and improvements to the experimental design will refine our understanding of these contributions further.

The first two sections in this chapter present the general procedure for measuring tune-out wavelengths and the theory behind the vector tune-out wavelength measurement. Section 4.3 discusses the first measurements of the vector polarizability at various polarizations, and Section 4.4 goes over a measurement using an improved experimental design to overcome several significant systematic limitations. This chapter ends by discussing further improvements in the experimental design. I will discuss our work towards improving the experimental precision and realizing the $6P$ measurements in Chapter 5.

4.1 General procedure

We find tune-out wavelengths by measuring the polarizability at several wavelengths near to and on both sides the tune-out wavelength using our BEC-based atom interferometer. As $\alpha(\omega) = 0$ at the tune-out wavelength, we simply look for where the effect of the Stark beam on the interferometric phase becomes independent of its intensity. The fixed-wavelength polarizability measurements are

themselves done over a range of Stark beam intensities where we measure the accumulated differential phase in the interferometer. The intensity is controlled through amplitude modulation of AOMs in the beam path. The phase difference that develops in the interferometer as a function of intensity is given by

$$\Delta\phi = \int -\frac{1}{2c\epsilon\hbar}\alpha(\omega)I dt. \quad (4.1)$$

As mentioned in Section 2.6, we measure this differential phase by looking at the ratio of atoms that come to rest upon recombination. Recall Eq. (2.21) where they are related by

$$\frac{N_0}{N} = \cos^2 \frac{\Delta\phi}{2}, \quad (4.2)$$

for the number of atoms at rest N_0 and the total number of atoms N . We are able to set the interferometer output to be $N'_0/N = 0.5$ in the absence of any additional phase shift by varying the frequency of the Bragg light slightly between the split and recombination pulse sequences. This is done to improve the interferometer sensitivity. N'_0 is the number of atoms at rest with this additional phase offset.

We look specifically at the rate at which this phase develops as we vary the intensity $d\phi/dI$ to find the tune-out wavelength. This provides several measurements at each wavelength and helps verify that the interferometer is working and that phase output from the interferometer is reasonable. Phase gradients and excessive phase accumulation can “wash out” the interferometer signal by leading to a fixed $N_0/N = 0.5$ output independent of intensity. This occurs because the

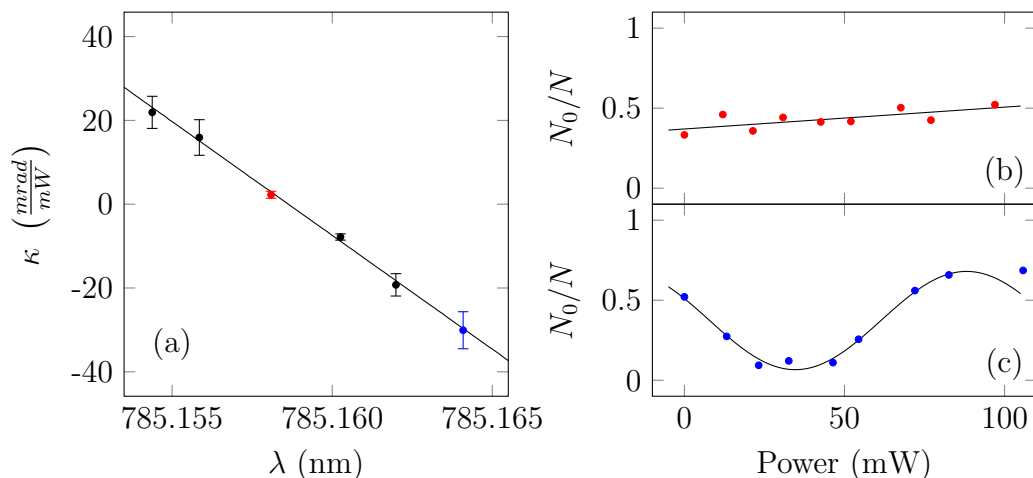


FIGURE 4.1: Sample data showing a typical tune-out wavelength measurement at $v \approx 0.5$. Subfigure (a) shows the full measurement, where κ is measured at different wavelengths near the tune-out wavelength. Subfigures (b) and (c) are two of those individual fixed-wavelength measurements.

phase gradients can destroy the coherence in the interferometer. As this mimics the signal we expect at the tune-out wavelength, we need to avoid this situation. Verifying that the interferometer signal is intensity dependent when not at the tune-out wavelength ensures that the measurement is valid.

To maximize the signal, we want the highest possible intensity, which can be achieved by focusing the Stark beam to a tight waist. However, if the focus is too small, then the measurement becomes unstable because the relative position of the atoms and laser drifts due to thermal expansion as the apparatus temperature varies. Temperature variations due to heat dissipation from the large dc spherical quadrupole and waveguide are a concern but can be dealt with by using a stable repetition rate and keeping the temperature constant in the waveguide by supplying a dc current of 8 A through the coils when not running. The atoms also undergo oscillations after loading into the waveguide due to either non-adiabatic loading or excitations from the 60 Hz background as the trap passes through resonance

with it, though these oscillations are typically coherent run-to-run.

We are most sensitive to alignment stability in the x direction as the atoms travel along y and the Rayleigh length of the beam along z is large compared to the condensate size. A detailed discussion on our efforts to stabilize the atom packet positions can be found in Bob Leonard's Thesis [7]. We choose a beam waist slightly larger than the condensate size of $25 \mu\text{m}$ in the x -direction to keep the atoms near the peak in intensity and avoid fluctuations in the interferometric signal due to the small positional variations on the order of $10 \mu\text{m}$. The beam waist is typically 30 to $50 \mu\text{m}$.

The Stark light is applied for the first 20 ms of the 40 ms interferometer. During this time, one of the atom packets traverses the beam twice, first as it passes through after initially being split at the start of the interferometer cycle and again after the reflect pulse reverses the packets' velocities. As the atoms pass through each other halfway through the interferometer cycle, the Stark beam is blocked so that the other atom packet is not exposed.

We use an AOM to vary the total optical power, so it is useful to rewrite Eq. (4.1) as the product of the total power in the Stark beam P and a parameter which characterizes the linear response of the phase which we will call κ .

$$\Delta\phi(\omega) = \kappa(\omega)P \tag{4.3}$$

Being proportional to the polarizability means $\kappa(\omega_0) = 0$ at the tune-out wavelength. We can express κ in the low power limit as

$$\kappa(\omega) = 2 \frac{d}{dP} \left(\frac{N'_0}{N} \right) \Big|_{P=0}. \quad (4.4)$$

We measure $\kappa(\omega)$ by taking the least squares linear fit of phase data at five to six different wavelengths near the tune-out wavelength per tune-out wavelength measurement. We then fit the slopes from those measurements and interpolate to find the tune-out wavelength where the slope would be zero. Figure 4.1 shows the data that go into a tune-out wavelength measurement. We are able to take one to three of these tune-out measurements in a single day limited primarily by our relatively low repetition rate of just one BEC production cycle every 110 s and the need to periodically remeasure and adjust the optical polarization and beam position relative to the atoms. The overall procedure for scalar and vector polarizability measurements differ slightly but both follow the general methodology outlined here. I will discuss in more detail the vector tune-out wavelength measurements in the next section. The scalar tune-out wavelength procedure can be seen in detail in Ref. [7].

4.2 Theory

We will start by expanding upon the theory first presented in Chapter 1 to develop the framework about which we will interpret the results and assess the success of

these initial vector polarizability measurements. Recall Eq. (1.5) which quantifies the energy shift due to the polarizability in terms of specific polarization dependent components. Our atoms in the $5S_{1/2}|F, m_F\rangle = |2, 2\rangle$ ground state and $v \equiv \frac{1}{2}S_3 \cos \theta$ can vary from $-1/2$ to $1/2$. α becomes

$$\alpha = \alpha^{(0)} - v \alpha^{(1)}, \quad (4.5)$$

where as before,

$$\alpha^{(0)} = \frac{1}{3\hbar} \sum_{n', J'} |d_{if}|^2 \frac{\omega}{\omega_{if}^2 - \omega^2} + \alpha_c + \alpha_{cv}^{(0)} \quad (4.6)$$

and

$$\alpha^{(1)} = \frac{1}{3\hbar} \sum_{n', J'} \left(3J' - \frac{7}{2}\right) |d_{if}|^2 \frac{\omega_{if}}{\omega_{if}^2 - \omega^2} + \alpha_{cv}^{(1)}. \quad (4.7)$$

The sums are over the valence states with $n' \geq 5$ and $J' = \frac{1}{2}, \frac{3}{2}$, and $|d_{if}| = |\langle i || \mathbf{d} || f \rangle|$ are the reduced dipole matrix elements. The core-valence correction can be expanded into its spherical tensor components $\alpha_{cv} = \alpha_{cv}^{(0)} + \alpha_{cv}^{(1)}$ [12], because whereas the core contribution is comprised of a symmetric closed shell and thus cannot have an asymmetric vector component, there is no such symmetry involving the single valence electron.

We can first consider the simplest case where α is comprised of just the two lowest terms in the sum, and the Stark laser is near the scalar tune-out wavelength at 790 nm. These lowest terms dominated the scalar polarizability measurement and will similarly dominate this vector polarizability measurement due to their large magnitudes and proximity to the Stark light. Let ω_J be the D_J transition

frequencies, and $\Delta = \omega_{3/2} - \omega_{1/2}$. Neglecting the higher-order terms and using the approximation $\omega \approx \omega_{1/2} \approx \omega_{3/2}$, we can write

$$\alpha \approx \frac{1}{6} \left(\frac{|d_1|^2(1-2v)}{\omega_{1/2} - \omega} + \frac{|d_2|^2(1+v)}{\omega_{3/2} - \omega} \right). \quad (4.8)$$

If we approximate the ratio of the dipole matrix elements as $R \approx 2$, we easily find where this equals zero and are left with a linear approximation as a function of the polarization parameter v .

$$\omega_a = \omega_{1/2} + \frac{1}{3}\Delta + \frac{2}{3}v\Delta \quad (4.9)$$

This simplest case hides the weaker but interesting dependence on the other terms in the polarizability but will be a useful benchmark for quantifying those terms later in the analysis particularly when looking at the divergence from this linear approximation. To develop a more detailed approximation, we can rewrite α by separating out the lowest lying elements from the previous approximation. Additionally it is worthwhile to normalize to a particular dipole matrix element. The obvious choice is that of the lowest-lying D_1 state.

$$\alpha \approx \frac{1}{3}|d_1|^2 \left(F(\omega) + A - Bv + \delta R \frac{\omega_{3/2} - v\omega}{\omega_{3/2}^2 - \omega^2} \right) \quad (4.10)$$

F contains the lowest lying states under the assumption $R = |d_{3/2}|^2/|d_{1/2}|^2 = 2$. F is the largest contributor to α for tune-out wavelength measurements between

the D_1 and D_2 lines.

$$F(\omega) = \frac{\omega_{1/2} + 2v\omega}{\omega_{1/2}^2 - \omega^2} + \frac{2(\omega_{3/2} - v\omega)}{\omega_{3/2}^2 - \omega^2} \quad (4.11)$$

The higher order states in the scalar and vector polarizability sums as well as their respective core contributions are in A and B .

$$A = \frac{1}{|d_1|^2} \left(3\alpha_c + 3\alpha_{cv}^{(0)} + \sum_{n',J'} |d_{if}|^2 \frac{\omega_{if}}{\omega_{if}^2 - \omega^2} \right) \quad (4.12)$$

and

$$B = \frac{1}{|d_1|^2} \left(3\alpha_{cv}^{(1)} + \sum_{n',J'} |d_{if}|^2 \left(3J' - \frac{7}{2} \right) \frac{\omega}{\omega_{if}^2 - \omega^2} \right) \quad (4.13)$$

The final term in Eq. (4.10) corrects for the ratio of the dipole matrix elements in F not being exactly two where $R = 2 + \delta R$.

We can find an approximate analytic solution for the zero in F through Taylor expansion.

$$\omega_F \approx \omega_{1/2} + \frac{1}{3}\Delta + \frac{2}{3}v\Delta - \frac{1}{9} \frac{\Delta^2}{\omega_{1/2}} (1 + v - 2v^2) \quad (4.14)$$

Combining Eqs. (4.9) and (4.11) lets us make an additional approximation near 790 nm.

$$\frac{\omega_{3/2} - v\omega}{\omega_{3/2}^2 - \omega^2} \approx \frac{3}{4\Delta} \quad (4.15)$$

We want to find an expression for the tune-out wavelength involving all of the contributions. The frequency response is primarily from F , not the smaller terms

involving A , B , and δR , so we want to find some $\omega = \omega_b$ such that

$$F(\omega_b) + A - Bv + \frac{3\delta R}{4\Delta} = 0. \quad (4.16)$$

By Taylor expanding $F(\omega)$ at $\omega_b = \omega_F + d\omega$ we find

$$F(\omega_F + d\omega) \approx F(\omega_F) + d\omega \frac{dF}{d\omega} = d\omega \frac{dF}{d\omega}. \quad (4.17)$$

It follows then that

$$d\omega \frac{dF}{d\omega} + A - Bv + \frac{3\delta R}{4\Delta} \approx 0. \quad (4.18)$$

Therefore, the frequency ω_b at which Eq. (4.16) is satisfied is

$$\omega_b = \omega_F + d\omega = \omega_F - \left(\frac{dF}{d\omega}\right)^{-1} \left(A - vB + \frac{3}{4\Delta}\delta R\right). \quad (4.19)$$

A , B , and δR are all small and we will treat them in first order only. We are left with the following for the frequency of the polarization dependent tune-out wavelength.

$$\omega_b = \omega_{1/2} + \frac{1}{3}\Delta + \frac{2}{3}v\Delta + \frac{\Delta^2}{9} \left(\frac{4}{3} \left(vB - A - \frac{3\delta R}{4\Delta} \right) - \frac{1}{\omega_{1/2}} \right) (1 + v - 2v^2) \quad (4.20)$$

As the wavelength dependence of v is predominantly linear, it is useful to subtract off the linear approximation from Eq. (4.9) to see the subtle higher-order polynomial dependence on the polarization. It is from this nonlinear dependence that we

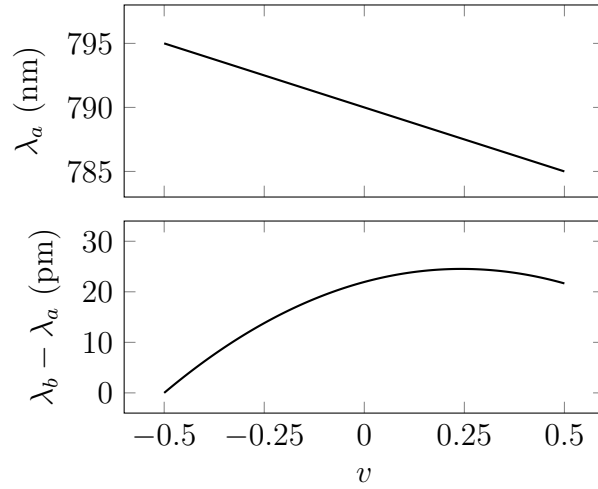


FIGURE 4.2: (Top) The linear approximation of the tune-out wavelength polarization dependence from Eq. (4.9). (Bottom) The full model from Eq. (4.21) with the linear approximation subtracted off. The model uses $A_{th} = 1.565(14)$ au, $B_{th} = 0.014(15)$ au, and $\delta 3R/4\Delta = -5.422$ au.

will be able to extract $A + \frac{3\delta R}{4\Delta}$ and B .

$$\Delta\lambda_{model} = 2\pi c \left(\frac{1}{\omega_b} - \frac{1}{\omega_a} \right) \quad (4.21)$$

The values for the model parameters are $A_{th} = 1.565(14)$ au and $B_{th} = 0.014(15)$ au. These were calculated using discrete dipole matrix elements and $\delta 3R/4\Delta = -5.422$ au from our previous scalar tune-out wavelength measurement [8], and a recent experimental measurement of $\alpha_c = 8.69(4)$ au [27]. A is already well constrained by the scalar polarizability measurement. What we hope to get here is a measurement of B . As we discussed in Section 1.3, the tail contributions come in differently to the sums in the scalar and vector polarizabilities. As A and B contain the higher-lying and small components for the scalar and vector polarizabilities respectively, experimental measurements of both allow the extraction of the terms of interest. The $n'J_{1/2}$ tail is most relevant for the atomic

Source	A	B
$5 < n' \leq 12$	0.105(1)	0.019(2)
α_c	1.517(1)	-
$\alpha_{cv}^{(0)}$	-0.062(7)	-
$\alpha_{cv}^{(1)}$	-	-0.007(7)
$ t_{1/2} ^2$	0.001(1)	-0.002(2)
$ t_{3/2} ^2$	0.004(4)	0.004(4)
Total	1.565(14)	0.014(15)

TABLE 4.1: Components of A and B calculated near the scalar tune-out wavelength at 790 nm.

parity violation analysis, but the others are of interest as well. The core-valence correction for example has not been measured fully either. The next sections will discuss our efforts to implement the first experimental measurement of B .

4.3 Experimental overview

The general procedure for measuring tune-out wavelengths which are shifted due to the nonzero vector polarizability is essentially the same as that of our previous scalar tune-out measurement [8]. The biggest difference is in the use of 5 μ s pulses of Stark light synced to the rotating bias field, instead of having the light on continuously, to eliminate the time-averaging of $\cos \theta$ and give a nonzero vector component. The Stark beam is aligned with one of the atom packets in the interferometer when they are at half their maximum separation. This occurs 5 ms after splitting. By changing the relative offset between the Stark pulse and the rotating bias field we can nearly arbitrarily set the optical polarization. By choice of timing we can shift the tune-out wavelength nearly 2/3 the fine structure splitting from

near 785 nm to the D_1 line at 795 nm. Refer back to Chapter 3 for more details on the polarization control technique.

The tune-out wavelengths are measured by first choosing a fixed timing delay for the Stark pulse relative to the trap bias field to set the polarization. This delay is measured by a fast photodiode *in situ*. We then measure the rate of phase accumulation κ at several fixed wavelengths at a fixed timing delay near to and on both sides of the tune-out wavelength. Some difficulty in initially making the measurements lies in the fact that the polarization dependent tune-out wavelengths span a range of 10 nm and being as little as tens of pm from the tune-out wavelength can easily wash out the interferometer due to rapid phase accumulation and phase gradients. The tune-out wavelength model described in Eq. (4.20) is a good starting point to search for a particular tune-out wavelength given the polarization used. A search of the region with an attenuated Stark beam is done until a reasonable phase begins to develop. We typically use 5% of the total available Stark beam power when searching as it allows for a search region of up to roughly 100 pm around the tune-out wavelength. During the search, it is often necessary to artificially add and remove a $\pi/2$ phase shift to the interferometer output to ensure the interferometer is not washed out. If it is washed out, the output will not change upon adding or removing the offset. Once the tune-out wavelength is found, we return the recombination offset to $\pi/2$ for maximum phase sensitivity and increase the optical power in the Stark beam to make a higher-precision measurement.

We use a Ti:Sa laser as the Stark beam to take advantage of its good spectral

qualities and high power. We are able to have up to roughly 120 mW at the atoms, which represents a relatively low efficiency given the 1 W out of the Ti:Sa. This is due in part to inefficient coupling through the polarization maintaining (PM) fiber which brings the light over from the laser table and three steering mirrors between the fiber output and the atoms which are unfortunately lossy. They will be removed from future iterations of this experiment both for this significant inefficiency and their somewhat detrimental wavelength dependence which was discussed in Section 3.7.

We focus the Stark beam on the atoms using a 45 μm beam waist to increase the intensity. Despite the relatively large peak intensity in excess of 3×10^6 mW/cm² on the atoms, the inefficiencies and reduced duty cycle result in a reduced integrated intensity at $3\times$ smaller than in our previous scalar tune-out wavelength measurement. This has an impact on our statistical uncertainty but can be readily improved by small tweaks to the experimental design which will be discussed near the end of this chapter.

Look back to Fig. 4.1 for example tune-out wavelength data, with both individual fixed wavelength polarizability measurements and a combined vector tune-out wavelength measurement showing where the polarizability vanishes. Twenty vector tune-out wavelength measurements at various polarizations are combined in Fig. 4.3. Included in the figure is the model from Eq. (4.21) using the theoretically derived values for $A + \frac{3\delta R}{4\Delta}$ and B , as well as the fit of the data. The vector data consists of the tune-out wavelength measurements with the linear approximation from Eq. (4.9) subtracted off, and the fit is done using Eq. (4.21) with $A + \frac{3\delta R}{4\Delta}$

and B as free parameters. Using our experimentally measured value for δR from the scalar tune-out wavelength measurement [8], we can then extract A .

Before continuing, it is important to note the large error bars in most of the data. These error bars are primarily due to timing errors from jitter and unknown timing offsets in the pulse generator, and asymmetry in the Stark beam pulse likely due to the AOMs. We discussed the general problem we face with regards to timing in Section 3.6, and as a reminder, we are more sensitive to these timing errors than anticipated due to the limited pulse configurations we can use to set the optical polarization as laid out in Section 3.5. This sensitivity is most extreme when not at the pole of the Poincaré sphere which can be seen in the smaller relative error bars when $v \approx 0.5$ ($v^3 \approx 0.12$ in Fig. 4.3), therefore the fit parameters will be constrained primarily by those data and the others are useful more in a qualitative comparison with the theory.

We also need to discuss several necessary corrections to the measured tune-out wavelengths. The values for A and B derived from theory lack hyperfine structure. We consider here only the ground state hyperfine splitting for the correction, where the $F = 2$ state the atoms are in is shifted 2.563 GHz [73]. The inclusion of the few hundred MHz $5P$ hyperfine splittings will be necessary as the experimental uncertainty is reduced. This will be done through refinement of the model in Eq. (4.20) using techniques laid out in Refs. [29, 30].

Additionally, we use two AOMs in series to control the pulse characteristics when setting the polarization. The use of two AOMs improves the extinction ratio

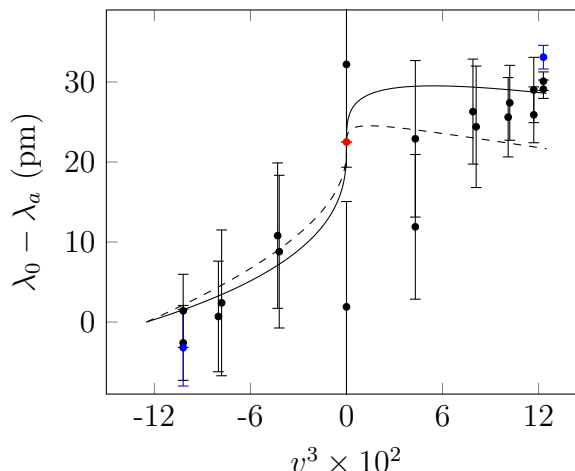


FIGURE 4.3: Example vector tune-out wavelength measurement data. The black points are vector tune-out wavelength measurements at a variety of polarizations. The blue points are done at opposite handedness in the lab frame to check for systematic biases. The red point is the previous scalar tune-out wavelength measurement. The solid line is the experimental fit and the dashed line is theoretical model. The fit yields $A = 1.66(1)_{Expt}(20)_{HF}$ and $B = -5.7(7)_{Expt}(2)_{HF}$ the latter of which differs from theory by about 8σ due to unaccounted for wavelength dependence in the optics.

and prevents excess leakage light from significantly affecting the polarization. Both AOMs shift the frequency 80 MHz for a total of 160 MHz from what the wavelength meter reports. The Stark beam AOM setup can be seen in detail in Appendix A. The total shift is

$$\begin{aligned} d\omega &= d\omega_{HF} + d\omega_{AOM} \\ &= 2\pi \times (2.563 \text{ GHz} - 160 \text{ MHz}) = 2\pi \times 2.403 \text{ GHz}, \end{aligned} \quad (4.22)$$

which is roughly 5 pm across the full tuning range.

We subtract this correction from the measured wavelength before comparing directly with theory. It should be noted that this full correction is only applied to the data measured here. The scalar tune-out result from our previous measurement

only needs the ground state hyperfine correction, as the Zeeman and any AOM shifts were already removed. Further, with this correction lacking the hyperfine structure of the $5P$ states we will need to include an additional uncertainty in A and B of roughly 0.2 au before making the comparison with theory. We arrive at this value for the uncertainty by comparing the theoretical location of the scalar tune-out wavelength with and without the $5P$ hyperfine structure. The scalar tune-out wavelength without the $5P$ hyperfine structure was calculated in Table 1.1 at 790.02568 nm, and its location including the $5P$ hyperfine splittings can be found in Table 4.2 in Ref. [7] which gives 790.03108 nm. The difference in the two is 5.4 pm for a difference from our correction of roughly 0.4 pm. Including the higher-lying hyperfine structure requires reworking the model from Eq. (4.20). While straightforward to do, we will include the associated correction as a rough estimate in the uncertainty here because our experimental precision is currently worse than the shift due to the higher-lying hyperfine structure.

The data in Fig. 4.3 have the correction already applied, and the result of the fit have $A = 1.66(1)_{Expt}(20)_{HF}$ au and $B = -5.7(7)_{Expt}(2)_{HF}$ au given $3\delta R/4\Delta = 5.422$ au. Compare these to the values derived from theory where $A_{th} = 1.565(14)$ au and $B_{th} = 0.014(15)$ au. We see an unfortunately large discrepancy in B compared to theory particularly near $v \approx 0.5$ where the error bars are small enough for the difference to be significant.

This discrepancy can be explained by the wavelength dependent retardances of the polarizing and nominally non-polarizing optics we discussed in Section 3.7. We can make a rough estimate of the effect using the empirical measurement of

the wavelength dependence of the polarization purity outlined in that section. We saw a change in polarization purity of $dv \approx 5 \times 10^{-5}$ over 10 nm, which shifts the tune-out wavelength $\Delta\lambda \approx 5$ pm at $v = 0.5$. This is reasonably consistent with the disagreement between the measurements and theory, but it is unlikely we can make a polarization correction to the data due to the difficulty in precisely determining dv .

It is worth noting that while these data consist of many distinct polarizations spanning $v = -0.5$ to 0.5 , this wide range of measurements is not strictly necessary. Recall Eq. (4.20). Consider that at $v = 0$, the tune-out wavelength is only dependent on $A + \frac{3\delta R}{4\Delta}$ due to B being multiplied by v in the model. Our high-precision measurement of the scalar tune-out wavelength from before already effectively constrains $A + \frac{3\delta R}{4\Delta}$ with less experimental difficulty. We then need only measure the tune-out wavelength at one other polarization to find B . The limitation on useful timing configurations outlined in Section 3.6 leads us to choosing $v = \pm 0.5$. These extrema are least sensitive to timing errors and many of the other experimental parameters such as any dc background magnetic fields. Because the tune-out wavelength for $v = -0.5$ occurs at the D_1 line, spontaneous emission is a significant concern. Therefore $v = 0.5$ is the best choice for the additional polarization to measure. In the next section we will discuss overcoming the remaining large discrepancy with theory via an additional step in the tune-out wavelength measurement procedure.

4.4 $v = 0.5$ measurement

In an effort to correct for the polarization error introduced when $v \neq -0.5$ due to the wavelength dependence of the various optics, we repeat the same general procedure with an additional polarization optimization step. The bluest possible tune-out wavelength occurs when $v = 0.5$, therefore any σ^+ or π components will shift the tune-out wavelength to the red. To minimize any σ^- component, adjustments to the wave plate angles are needed. The wave plate angles α_1 and α_2 as defined in Section 3.4 are not independent of one another, so multiple iterations of optimization are necessary.

For the π component, the alignment of the beam with the bias field needs to be corrected. Optimizing timing and B_y alone are sufficient here as we only care about this polarization and do not need the field uniformity to hold for other polarizations as we did in the previous section. These parameters are reasonably independent due to the geometry of the waveguide. We will be unable to get an absolute measure of the polarization purity as we did using σ^+ light near 795 nm, but can use the precision in setting the four parameters to come up with a reasonable estimate of the final polarization uncertainty.

I was able to complete a single tune-out wavelength measurement using this additional optimization step. For the measurement, the polarization purity was optimized as usual on the D_1 line, to $|\mathcal{E}_\pi|^2 + |\mathcal{E}_-|^2 \approx 1.3 \times 10^{-4}$. Because the polarization is adjusted after the laser is tuned to 785 nm, this is adequate as it gets us reasonably close to the correct polarization.

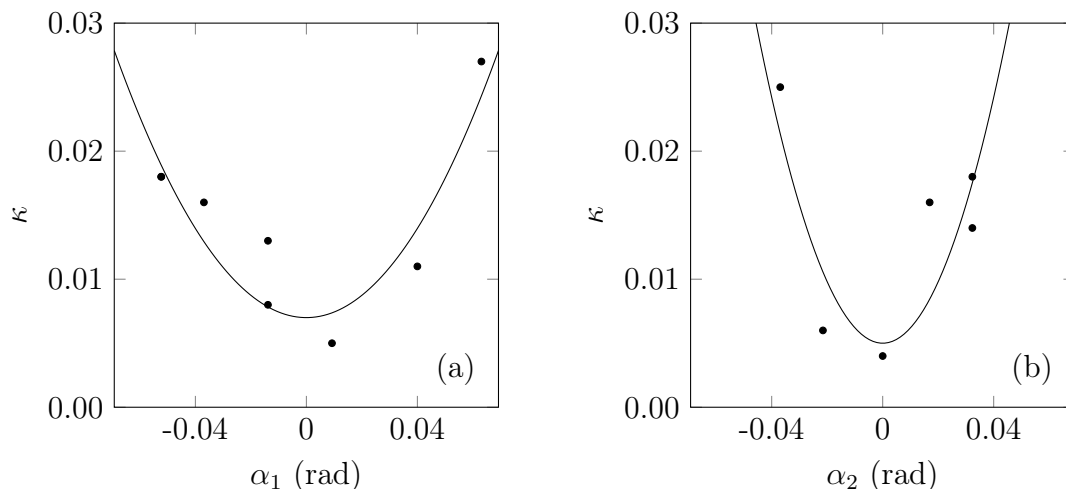


FIGURE 4.4: (a) Quarter- and (b) half-wave plates are optimized at 785 nm after being initially set at 795 nm. Measurements are taken at a 785.15 nm which is roughly 2 pm to the blue of the $\nu = 0.5$ tune-out wavelength. The rate of phase accumulation κ is used to assess the wave plates' alignments. The errors in the fitted minimum angles are 0.003 rad for both wave plates.

The wave plate angle and alignment parameters were optimized by tuning the laser to the blue of the $\nu = 0.5$ tune-out wavelength and measuring the rate of phase accumulation κ while varying the angles and timing independently. κ is minimized when the parameters are optimally set as the tune-out wavelength will be at its bluest. The wavelength chosen was $\lambda \approx 785.15$ nm, roughly 2 pm blue of the tune-out wavelength.

The wave plate angles peaked up at angular changes from where they were initially optimized on the D_1 line of $\Delta\alpha_1 = 0.018$ rad for the quarter-wave plate and $\Delta\alpha_2 = 0.009$ rad for the half-wave plate after two iterations for total polarization variation of

$$dv \approx 2\alpha_1^2 + 4\alpha_2^2 - 4\alpha_1\alpha_2 = 4 \times 10^{-4}. \quad (4.23)$$

These angular changes are qualitatively in agreement with what we would expect from the wavelength dependence of the optics (the mirrors in particular), as the

disagreement between our previous measurements without this final compensation and theory can be explained by a polarization impurity of roughly 10^{-3} .

The polarization error from our ability to set the wave plate angles is also fairly significant in the current measurements. Section 3.4 gives the framework for relating $S_3 = |\mathcal{E}_+|^2 - |\mathcal{E}_-|^2$ to the effective polarization and assessing small changes and errors in the polarizing optics.

$$S_3 \approx (1 - 2|\mathcal{E}_-|^2) \quad (4.24)$$

In terms of the Stokes parameters, $|\mathcal{E}_-|^2$ is expressed as

$$|\mathcal{E}_-|^2 \approx \frac{S_1^2 + S_2^2}{4}, \quad (4.25)$$

where the individual Stokes parameters are related to the quarter- and half-wave plate angles α_1 and α_2 respectively by

$$\mathbf{S} = \begin{bmatrix} -2\alpha_1 \\ 4\alpha_2 - 2\alpha_1 \\ 1 \end{bmatrix}. \quad (4.26)$$

As we are near the axes of the wave plates, the error in $|\mathcal{E}_-|^2$ is

$$d|\mathcal{E}_-|^2 \approx 2d\alpha_1^2 + 4d\alpha_2^2 - 4d\alpha_1 d\alpha_2. \quad (4.27)$$

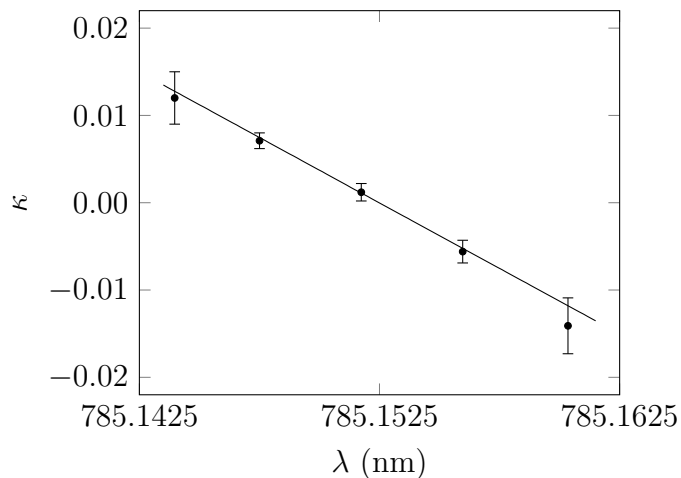


FIGURE 4.5: Vector tune-out wavelength measurement with $v \approx 0.5$ after wave plate angles and pulse timing where optimized at 785 nm.

So far the uncertainties have been about the same for the two wave plates. It follows then that

$$dS_3 = 2d|\mathcal{E}_-|^2 \approx 4d\alpha_1^2. \quad (4.28)$$

We can use Eq. (4.28) to estimate the uncertainty in polarization based on the errors in the optimized wave plate angles. The fitted minimum angles in Fig. 4.4 have errors of $d\beta = 0.002$ rad, so $dS_3 = 1.6 \times 10^{-5}$. If we include the full tuning range of 10 nm over $|\mathcal{E}_-|^2 = 0$ to 1, this polarization uncertainty gives an uncertainty in the tune-out wavelength of 160 fm. On the D_1 line we regularly were able to find the wave plate angles to better than 5×10^{-4} rad, so it is likely the uncertainty in this measurement will drop through more iterative adjustments and an increase in the number of measurements.

When reoptimizing at 785 nm, the timing did not change from where it was previously determined to be. It was not expected to because the disagreement in B was due to the wavelength dependence of the optical polarization. Additionally,

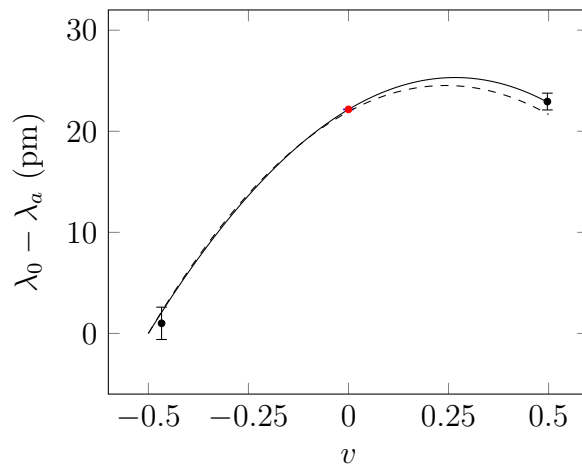


FIGURE 4.6: Vector tune-out wavelength model and data. The black points are $v \approx \pm 0.5$ with the $v \approx 0.5$ point re-optimized at 785 nm to account for the polarization drift. The red point is previous scalar tune-out wavelength measurement. The solid line is the fit where $A = 1.66(1)_{Expt}(20)_{HF}$ and $B = -0.8(7)_{Expt}(2)_{HF}$. The dashed line is the model of $\lambda_b - \lambda_a$ using theoretical values for A_{th} and B_{th} .

the work done to fully symmetrize the rotating bias field as discussed in Section 3.2 ensured we could precisely reverse the polarization from σ^+ on the D_1 line to σ^- used here. An attempt to verify that $B_y = 0$ was done as well, but a small gradient from the bias coils moved the atoms off of the beam. I lacked the time to realign the beam with the atoms for each measurement. Fortunately, B_y is expected to be well-optimized due to the trajectory data and because the field alignment is independent of the laser wavelength. It will however be worth verifying that this parameter is indeed fully optimized in the future.

Following the reoptimization, I remeasured the tune-out wavelength, and it shifted an amount $\Delta\lambda \approx 5$ pm from the previous measurements using the same pulse configuration. This change is consistent with the roughly 6 pm shift we would expect based on the 5.7 au disagreement with theory we saw before. Doing the same wavelength correction of roughly 5 pm as in the previous section yields $A =$

Source	Error	Error (fm)
Statistical	-	800
Polarization	3×10^{-3} rad	160
Tilt	0.12°	10
z position	$3.5 \mu\text{m}$	30
B_x	6 mG	< 1
B_y	10 mG	< 1
B_z	4 mG	10
ΔB_0	17 mG	< 1
5 μs pulse shape	28 ns	< 1
Timing calibration	8 ns	< 1
Wavemeter	0.2 ppm	150
Total	-	830

TABLE 4.2: Vector tune-out wavelength error budget. The experimental errors are from calculations of the change in $\cos\theta$ based on the particular value.

$1.66(1)_{\text{Expt}}(20)_{\text{HF}}$ au and $B = -0.8(7)_{\text{Expt}}(2)_{\text{HF}}$ au for the $v = 0.5$ measurement.

If we compare these to the values derived from theory where $A_{\text{th}} = 1.565(14)$ au and $B_{\text{th}} = 0.014(15)$ au, we see much better agreement than before where A is still within 1σ and B just over that at 1.2σ .

Despite the large uncertainty in B of roughly $40\times$ that of theory, this is first experimental measurement capable of extracting the tail contributions ($n' > 12$) which are needed in the atomic parity violation analysis, so while there is significant room for improvement, this experiment represents an important step towards better understanding these theoretically challenging contributions. In the next chapter, we will work through using the experimentally measured values of A and B to give the first experimental constraints on those terms. Table 4.2 shows the full error budget for B . The largest single contribution is statistical, which can be reduced through additional measurements. Based on the error budget from our previous measurement [8] and the reduced integrated peak intensity here, we

can expect the statistical uncertainty to approach 40 fm after a sufficient number of measurements. My previous data has already shown that statistical errors of around 125 fm at $v = 0.5$ are achievable over a single day of data acquisition. Additionally, the wavelength meter can readily be calibrated and its contribution to the uncertainty made negligible. The remaining largest single contribution is the polarization uncertainty. In the next section, we will work through a few scenarios to reduce this uncertainty in an effort to better design the next implementation of this experiment.

4.5 Polarization improvements

If we could measure the $v = 0.5$ tune-out wavelength to a similar accuracy as our previous scalar tune-out wavelength (32 fm), the experimental uncertainty in B would be $dB = 0.027$ au. We would therefore like to determine what improvements can be done to improve the current experimental uncertainty beyond that level. The statistical uncertainty currently dominates the total uncertainty at 0.6 au. Based on our previous scalar tune-out wavelength measurement [8], we can expect the contribution from the statistical error on B to drop to 0.03 au after a sufficient number of measurements given our reduced integrated intensity. The polarization's contribution to the total uncertainty is currently 0.14 au. Both errors can be reduced through an increase in the integrated intensity. This section will focus on a few improvements aimed at doing just that. We will discuss a few other experimental changes in the next chapter that if implemented should reduce the

total uncertainty significantly further, and allow our experimental precision to reach the level of theory.

As mentioned previously, we currently have a factor of three reduction in integrated intensity of the Stark beam compared to our previous measurement. Let's now explore the polarization uncertainty's dependence on the integrated intensity to see what we can expect with reasonable improvements to the experimental design. The phase difference that develops between the two arms of the interferometer is given by

$$\Delta\phi = -\frac{\hbar}{2c\epsilon}\alpha(\omega)It = -\frac{\hbar}{2c\epsilon}(\alpha^{(0)} - v\alpha^{(1)})It. \quad (4.29)$$

We can look at how the interferometric phase varies with wave plate angle when near a tune-out wavelength to estimate how precisely we can set the wave plate angles. There is a maximum phase difference we can resolve before the interferometer signal washes out. This typically occurs above 2π , though we tend to stay below π to avoid any reduction in visibility from affecting the data. The exact phase we use though is irrelevant in this discussion, as long as we consider fixed maximum phase in determining the uncertainty estimates. At the $v = 0.5$ tune-out wavelength, this phase maximum $\Delta\phi_{max}$ occurs when a wave plate is rotated by some angle β for a given integrated intensity It . At this wavelength, the polarizability is

$$\alpha = \alpha^{(0)} - (1 - 2|\mathcal{E}_-|^2)\alpha^{(1)} = 2|\mathcal{E}_-|^2\alpha^{(1)} \approx 4\beta^2. \quad (4.30)$$

If we plug this into the equation for $\Delta\phi$, we get

$$\Delta\phi_{max} = -\frac{2\hbar\alpha^{(1)}}{c\epsilon}\beta^2 It. \quad (4.31)$$

We can rewrite the expression as

$$\beta^2 It = \frac{4\Delta\phi_{max}c\epsilon}{\hbar\alpha^{(1)}} \equiv \gamma \quad (4.32)$$

with $\gamma = \text{constant}$. Therefore we can see that the maximum adjustment we can make to β scales with integrated intensity as

$$\beta \sim \frac{1}{\sqrt{It}}. \quad (4.33)$$

The center of a parabola can typically be found to a few percent, so the precision we can expect to set the wave plate angles also scales as $1/\sqrt{It}$. We will use this to estimate the effect of any improvements to the experiment.

There are several straightforward improvements that can help reduce the uncertainty in polarization. First, we can increase the intensity. The beam waist at the atoms is larger than in the past. This was done to keep the atoms and beam more easily aligned, but can likely be reduced as long as the overlap is periodically checked while taking data, which is more easily done when the experiment is run with multiple graduate students. Additionally there is significant optical power lost on the beam steering mirrors and the efficiency into the fiber is not great. Adjustments to the optical setups before and after the fiber could increase the

Power (mW)	w_0 (μm)	τ_{max} (μs)	Improvement in $I\tau_{max}$
100	45	12	$2.4\times$
300	37.5	6.8	$5.5\times$
300	30	5	$6.8\times$

TABLE 4.3: Potential improvements in integrated intensity. Close to an order of magnitude increase is possible with minimal changes to the experimental setup. Starting point is $3\times$ less than previous scalar tune-out wavelength measurement.

optical power at the atoms by at least a factor of three.

Another improvement might be in the pulse length. We never fully searched for the optimal pulse length, nor compared the atom loss as a function of the pulse length to what we would expect from theory. In Section 3.5 we calculated an estimate for the maximum pulse width for the timing configuration used to set $v \approx 0.5$, where an increase from the $5 \mu\text{s}$ pulses used in here to as much as $12 \mu\text{s}$ should be possible. The limit on the pulse width is dependent upon the optical dipole force, and if changes are made to the total power, beam waist, or pulse width, we need to account for the increase in the impulse from the Stark beam $|J_+|_{v=1/2}$ and ensure it remains below the BEC momentum distribution.

$$|J_+|_{v=1/2} \approx \frac{PL\alpha^{(1)}(\omega)}{\pi c \epsilon_0 w_0^4} \frac{\Omega_1^2 \tau^3}{24} < 10^{-29} \text{ kg}\cdot\text{m/s} \quad (4.34)$$

As before, P is the total optical power, L is the condensate size, w_0 is the beam waist, Ω_1 is the TOP trap bias field rotation frequency, and τ is the pulse width. In the current configuration, $|J_+|_{v=1/2} \approx 8 \times 10^{-31}$, so an increase of roughly up to roughly $15\times$ is reasonable without expecting significant atom losses. We can

estimate the increase in performance using various configurations easily using

$$|J_+|_{v=1/2} \sim \frac{P\tau^3}{w_0^4}. \quad (4.35)$$

Table 4.3 shows several reasonable improvements that can be made to increase the integrated intensity It over the current experiment.

As our ability to set the wave plate angles is essentially limited by our ability to measure the interferometer phase, the statistical error will decrease with increased intensity in the same way. The measurement discussed here included just a single tune-out wavelength measurement, so a reasonable number of additional measurements will reduce the statistical uncertainty. For the estimate we will use ten measurements and a statistical uncertainty based on the current setup achievable over a single day of 150 fm. This was typical for the other $v \approx 0.5$ measurements compared to the 800 fm statistical uncertainty here. The lower number is more in line with what we saw in the previous scalar tune-out wavelength measurement corrected for the smaller integrated intensity here.

Another significant source of error in Table 4.2 is the variation in atom position. These variations affect the polarization through a nonzero contribution from the linear quadrupole when not at the trap center. Refer back to Chapter 3 to see how the field components vary with position. This additional nonzero field contribution changes the effective width of the $v \approx 0.5$ Stark pulse, and by calculating $\hat{k} \cdot \hat{b}$ directly we can estimate the uncertainty in v due to these variations. Therefore in the present setup there are diminishing returns as the improvements are done

because we are ultimately limited by positional stability in the z direction until the experimental design is changed to accommodate these variations. I am leaving out any potential improvements to this sensitivity in the current estimates, but I will discuss in Section 5.2.3 what can be done to reduce this contribution to the experimental uncertainty.

The final significant contribution to the uncertainty comes from the wavelength meter. It is a Bristol 621A wavelength meter with a specified ± 0.2 ppm accuracy which at 790 nm is 160 fm. It is able to display up to nine significant digits and has a stable reading to eight digits with averaging. We typically average over 10 measurements. In our previous measurement [7], we calibrated the wavelength output using measurements of the D_1 and D_2 atomic transitions in K, Rb, and Cs. This calibration was done periodically while taking data using a saturated absorption spectroscopy setup and vapor cells containing the three elements. We were able to determine a correction to apply to improve on the accuracy to better than 10 fm. This calibration was not done for the present data due to the increased experimental uncertainty, so listed in Table 4.2 is the effect of the specified accuracy. As the improvements we are discussing here are implemented it will be necessary to again calibrate the wavelength meter, so I use the uncertainty in our previous calibration to estimate what we will see here.

Table 4.4 shows the significant contributions to the total error budget estimates for the measurement presented here and the three reasonable improvements considered above. We leave out the additional $5P$ hyperfine contribution discussed in Section 4.3 as it will be removed by expanding the model in Eq. (4.20) as the

Source	dB (au)			
	Current	2.4×	5.5×	6.8×
Statistical	0.68	0.017	0.008	0.006
Polarization	0.14	0.058	0.025	0.021
Tilt	0.009	0.01	0.009	0.009
z position	0.026	0.026	0.026	0.026
B_z	0.009	0.009	0.009	0.009
Wavemeter	0.13	0.004	0.004	0.004
Total	0.71	0.067	0.039	0.036

TABLE 4.4: Estimated experimental error in B due to cumulative improvements of integrated intensity. The specifics of each improvement are detailed in Tab. 4.3. Compared to the uncertainty from theory of $dB_{th} = 0.015$ au, further improvements are still needed.

various improvements are implemented. We estimate then that we can measure B to a precision of $dB = 0.036$ au through several reasonable improvements to the experimental design. This is a factor of two above $dB_{th} = 0.015$ au, but as it will be the only experimental constraint B , the information we get by combining it the measurement of A from the scalar tune-out wavelength result should prove useful in assessing the current theoretical estimates for the difficult to calculate tail and core-valence terms. I will present several more substantial routes for improvement in the next chapter. These have the potential to surpass the theoretical uncertainty, but more specific developmental work will be necessary to choose the path forward.

Chapter 5

Conclusion and future work

Tune-out spectroscopy has opened up a rich field of study and allows access to previously inaccessible components of atomic structure, namely dipole matrix elements. The apparatus used in this experiment still has plenty of room to continue improving. See Chapters 2 and 3 for detailed descriptions of the current setup. This thesis will conclude with a discussion that puts the results from Chapter 4 into a broader perspective through the impact of future improvements to the experiment on its potential contributions to the theoretical analyses that motivate our work.

5.1 Impact of results

Recall our discussion on atomic parity violation (APV) in Chapter 1. The parity nonconservation amplitude A_{PNC} from Eq. (1.3) depends on the $n'P_{1/2}$ dipole

matrix elements. A significant theoretical uncertainty is introduced during the analysis due to insufficient knowledge of the higher-lying matrix elements [13–15]. The largest contribution to this theoretical uncertainty comes from the difficulty in estimating the sum to infinity “tail” from the matrix elements not discretely calculated. Measurements of tune-out wavelengths offer a potential path to reduce these uncertainties.

The contributions to the scalar tune-out wavelength from the matrix elements of the $n'P_{1/2}$ and $n'P_{3/2}$ states come in together via a sum, but only the $n'P_{1/2}$ terms come into the APV analysis. So while allowing a potentially useful estimate of the two tail contributions together, scalar tune-out wavelength measurements alone do not remove the need for an imprecise estimate of the higher-lying states in the APV analysis. In the previous chapter, we discussed a measurement of the vector polarizability through measurements of tune-out wavelengths shifted by carefully controlled changes to the optical polarization. What these measurements contribute is the ability to separate out the $n'P_{1/2}$ and $n'P_{3/2}$ tail contributions due to the J' contributions having different coefficients. Therefore, by combining measurements of scalar and vector tune-out wavelengths it should be possible to determine the $n'P_{1/2}$ and $n'P_{3/2}$ tail contributions individually. The tail contributions are $|t_{1/2}|^2$ and $|t_{3/2}|^2$ for $J' = 1/2$ and $3/2$ respectively, where

$$|t_{J'}|^2 = \sum_{n'>12} |d_{J'}|^2. \quad (5.1)$$

As a reminder, Eqs. (4.12) and (4.13) contain the scalar and vector contributions respectively. Measurement of these two parameters will allow us to separate out the J' dependence.

$$A = \frac{1}{|d_1|^2} \left(3\alpha_c + 3\alpha_{cv}^{(0)} + \sum_{n',J'} |d_{if}|^2 \frac{\omega_{if}}{\omega_{if}^2 - \omega^2} \right) \quad (5.2)$$

and

$$B = \frac{1}{|d_1|^2} \left(3\alpha_{cv}^{(1)} + \sum_{n',J'} |d_{if}|^2 \left(3J' - \frac{7}{2} \right) \frac{\omega}{\omega_{if}^2 - \omega^2} \right) \quad (5.3)$$

The J' dependence in B is through $3J' - \frac{7}{2}$, where it equals 1 for $J' = 3/2$ and -2 for $J' = 1/2$. If we subtract of the discrete matrix elements for $5 < n' \leq 12$ and core contributions from the experimentally measured values of A and B , we can access the tail contributions. Table 1.1 contains discretely measured or calculated matrix elements up to $n' = 12$ in ^{87}Rb , the core polarizability, and the tails. How these contribute to A_{th} and B_{th} explicitly can be found in Table 4.1. Let A' and B' be the remaining tail contributions to A and B respectively after the other terms are removed. Recall that from Section 4.4 we measured $A = 1.66(1)_{Expt}(20)_{HF}$ au and $B = -0.8(7)_{Expt}(2)_{HF}$ au.

$$A' = A - 1.560(9) \text{ au} = 0.1(2) \text{ au} \quad (5.4)$$

$$B' = B - 0.017(9) \text{ au} = -0.8(7) \text{ au} \quad (5.5)$$

We can now determine the J' tails independently through combinations of A' and B' .

$$|t_{1/2}|^2 = \frac{1}{3}|d_{1/2}|^2(A' - B') = 5(4) \text{ au} \quad (5.6)$$

$$|t_{3/2}|^2 = \frac{1}{3}|d_{1/2}|^2(2A' + B') = -4(4) \text{ au} \quad (5.7)$$

The experimental values are reasonably consistent with the theoretical estimates $|t_{1/2}|^2 = 0.022(22) \text{ au}$ and $|t_{3/2}|^2 = 0.075(75) \text{ au}$ within their uncertainties but the experimental uncertainties are currently $200\times$ greater. We can look at the estimated achievable uncertainties to determine how well we can expect to be able to find $|t_{J'}|^2$ when the experimental uncertainty is reduce. We will use the best case estimate of $dB = 0.036 \text{ au}$ shown in Table 4.4 to see what the short term performance improvement might lead to. The uncertainties in the tails with the modest experimental improvements reduce to

$$d|t_{1/2}|^2 = 0.22 \text{ au} \quad (5.8)$$

and

$$d|t_{3/2}|^2 = 0.27 \text{ au.} \quad (5.9)$$

Though the uncertainty is roughly $10\times$ higher than current uncertainty estimate for the $n'P_{1/2}$ tail, no other experimental measurements of the tail components exist to date. Additionally, theoretical estimates for the tail are quite challenging,

so even a low accuracy experimental value for comparison would be useful. Further, we fully expect that many additional improvements will be possible, so that an experimental accuracy relevant to the APV measurements can ultimately be achieved. I will discuss the future tune-out wavelength experiments in Section 5.3 and how they are necessary to fully extract the various contributions, but first I want to go into a little more detail on the incremental improvements to the overall experimental design which were described in Section 4.5 and used in the present analysis.

5.2 Experimental improvements

Our ability to almost arbitrarily set the optical polarization is useful feature not seen in many other experiments, but significant limitations in this technique remain such as the timing difficulties from Section 3.6 and the wavelength dependence of optics outlined in Section 3.7. I want to outline briefly several specific improvements that will overcome many of the challenges mentioned throughout this thesis and bring the experimental uncertainty closer to the current theoretical uncertainty.

5.2.1 Optics

The re-optimization technique outlined in Section 4.4 corrects for the change in polarization estimated at near the 10^{-3} level due to the wavelength dependence of

the various post-polarizer optics in the Stark beam path, whereas we empirically measured the behavior of the Fresnel rhomb and wave plates in an external test rig and saw variations closer to the 10^{-5} level. A reasonable starting point is then to remove the optics with the largest uncontrolled wavelength dependence that were present in this work. The largest such culprit is suspected to be the protected gold mirrors. These mirrors were necessary due to geometric constraints from the overall apparatus superstructure and an underestimation of their overall effect on the experiment during the design phase. A redesign of the optics system for polarizing the light and controlling its orientation at the atoms is thus warranted.

I suggest swapping the locations of the vertical imaging probe and Stark optics with vertical camera such that the camera would image the atoms from below as opposed to imaging from above in the current setup. The output fiber coupler and polarization optics can be mounted on a translatable breadboard pointing straight down into the chamber, which removes the need for any steering mirrors. High load tip/tilt and linear translators are available to give the necessary control over beam steering.

5.2.2 Timing

Another area of the overall experiment with significant room for improvement is in the timing control and stability of the Stark pulses. We designed the control

mechanism for the *in situ* optical polarization to be entirely timing-based. The final tune-out measurement uncertainties at arbitrary polarizations can be sensitive to timing jitters and unknown delays on the scale of nanoseconds.

As I mention in Chapter 4, the parameters A and B can be constrained quite well using only the scalar polarizability result and a single vector tune-out measurement. Choosing $v = 0.5$ as that measurement reduces the sensitivity to timing errors, but it is still desirable to reduce timing instabilities to enable measurements of tune-out wavelengths at additional polarizations. For instance, this would allow a timing-based measurement of the scalar polarization, providing a consistency check for the two methods.

There are a few changes in particular that should lead to much smaller polarization uncertainties. The first is a better pulse generator. Our experiment used an Agilent 81110A, which has a jitter of roughly 8 ns given our experimental parameters. This corresponds to an overall error of nearly 5 pm near the scalar tune-out wavelength where we are most sensitive. Other commercial products are available which should reach the necessary precision. A potential replacement is the Stanford Research Systems DG535 digital delay generator with a jitter of < 100 ps and 5 ps delay resolution, though some additional work may be necessary to ensure the output voltage is stable and accurate. It will quite difficult to fully reduce the timing uncertainty to a level where a measurement of the scalar tune-out wavelength using the polarization control method outlined in this thesis can approach that of our previous measurement, but a more reasonable check on the latter than what we were able to achieve here is still desirable.

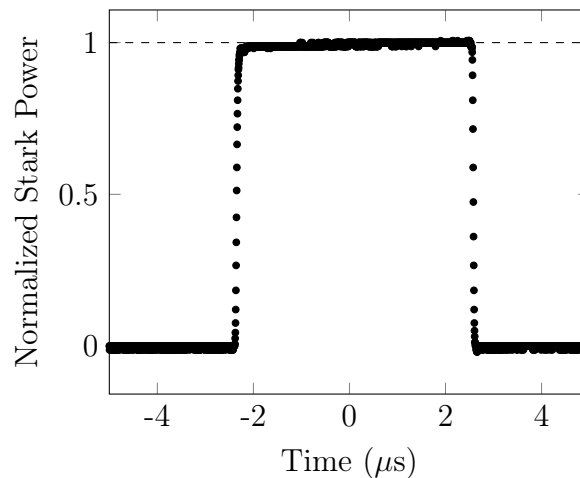


FIGURE 5.1: A slight asymmetry of 3% over the 5 μs Stark beam pulse shown here leads to a 28 ns timing correction. While negligible for $v = 0.5$, it corresponds to a several pm shift in the scalar tune-out wavelength. The need for this correction and thus any uncertainty introduced by it can be reduced through different Stark beam switching optics. The dashed line is included at the mean value to guide the eye.

Another improvement would be to change how the Stark beam amplitude is modulated. Right now, as laid out in Appendix A, we use two acousto-optic modulators (AOMs) in series to switch the beam on and off, but AOMs have several drawbacks. They have a delay in switching, which while stable, is quite large compared to our precision requirement. This delay is as much as 1 μs due to capacitive effects in the AOM and the speed of sound within the AOM crystal. An additional drawback due to the finite speed of sound in the crystal leads to distortions of the pulse shape and a relatively large minimum pulse width. The latter has significant implications for measurement of the polarization purity due to the time dependent bias field. The roughly 120 ns pulse width corresponds to a variation in polarization over the pulse width of 10^{-5} given the 12.8 kHz bias field rotation frequency.

A further limitation on precisely controlled polarizations not near the pole of

the Poincaré sphere is that we observe an asymmetry in the optical pulse shaping likely due to heating in the crystal. This asymmetry can be seen in Fig. 5.1. It leads to a timing correction that could be avoided or at least suppressed significantly through the use of a better switching method. A reasonable choice might be to use a Pockels cell to do the switching. They have switching times on the order of 10 ns which is $6\times$ faster than in our current AOM-based setup. It would be necessary to use an AOM to gate the Pockels cell due to its reduced extinction ratio compared to the current setup.

There is also the possibility of changing the TOP trap rotation period to reduce dependence on timing instabilities. As mentioned in Section 2.4, the choice of frequency is fairly large, needing only fall between where the atomic motion lies and the Larmor frequency, which spans hundreds of Hz to nearly 10 MHz. Slowing the trap down to the single kHz range would decrease the timing sensitivity an order of magnitude in the current setup given the same jitter and error from the electronics. The next section will discuss further changes to the bias rotation frequency which can further benefit the timing precision requirements.

5.2.3 Bias field rotation frequency

In the present setup, a significant limitation on the experimental precision is from atom positional variations. They lead to changes in the total bias field through a nonzero contribution from the linear quadrupole when not at the trap center which makes determining the effective polarization from timing measurements

alone potentially imprecise. We are particularly sensitive to the atoms' position in the z direction for the $v \approx 0.5$ measurement. The linear quadrupole field \mathbf{B}_1 , has a gradient of 30.7 G/cm which quickly leads to a larger than tolerable variation in the bias field. At $dz = 10 \mu\text{m}$, it contributes 30 mG to the total field.

We can calculate $\hat{k} \cdot \hat{b}$ directly and vary the atoms' position to estimate the positional stability's contribution to the polarization uncertainty. We find that at $v \approx 0.5$ set using a $5 \mu\text{s}$ wide pulse, $dz = 10 \mu\text{m}$ leads to $dv = 3 \times 10^{-6}$. This problem is even more exacerbated for the $12 \mu\text{s}$ pulse which we hope to implement to increase the integrated intensity where the uncertainty increases to an intolerable $dv = 2 \times 10^{-5}$.

One solution to the reduce the sensitivity both on the atoms' position and the Stark pulse timing is through the addition of higher-order frequency terms $\sin(n\Omega_1 t)$ to change the bias field's instantaneous angular velocity. It is straightforward to implement using arbitrary function generators without further loss of the integrated intensity of the Stark beam. To maintain the same duty cycle, the higher-order terms are added such that bias field can be slowed down during the Stark pulses and sped up elsewhere. We can work through the simplest case with the addition of a second order frequency term. Recall the ideal normalized rotating bias field from Eq. (2.10), where

$$\frac{\mathbf{B}_0}{B_0} = \sin \Omega_1 t \hat{x} + \cos \Omega_1 t \hat{z}. \quad (5.10)$$

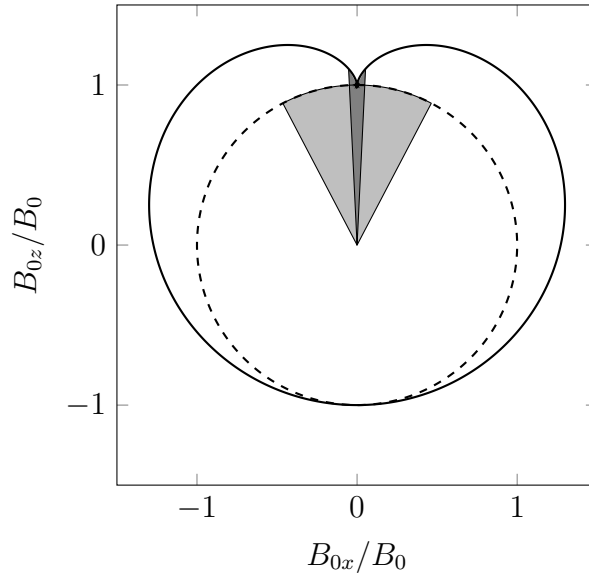


FIGURE 5.2: Example higher order bias field. The dashed line is the current normalized bias field $\mathbf{B}_0 = \sin \Omega_1 t \hat{x} + \cos \Omega_1 t \hat{z}$. The solid line is a possible higher order extension with a $2\Omega_1$ component given by $\mathbf{B}_{\text{new}} = (\sin \Omega_1 t + 0.5 \sin 2\Omega_1 t) \hat{x} - (\cos \Omega_1 t + 0.5 \cos 2\Omega_1 t - 0.5) \hat{z}$. The shaded regions show the areas swept out in a $12 \mu\text{s}$ pulse for the current setup (lighter) and the extension (darker). The integrated physical angle swept out in the extension is $20\times$ smaller than in the current setup, resulting in a decrease in sensitivity to the atoms' position.

The first extension would be to add $2\Omega_1 t$ terms.

$$\frac{\mathbf{B}_{\text{new}}}{B_{\text{new}}} = (\sin \Omega_1 t + 0.5 \sin 2\Omega_1 t) \hat{x} - (\cos \Omega_1 t + 0.5 \cos 2\Omega_1 t - 0.5) \hat{z} \quad (5.11)$$

The magnitude and offset of the second order term are chosen to keep \mathbf{B}_{new} similar enough to the current bias field to avoid adversely affecting the atoms, though actual implementation of any higher-order corrections requires changes to the bias field drive electronics which are currently optimized to operate at 12.8 kHz.

How the positional variations affect the experimental uncertainty scales approximately with the angle swept out during the Stark pulse. A larger angle swept out makes the effective polarization more sensitive to variations in the other field

components by changing the angle of the rotating bias field from what we expect based on the Stark pulse timings. The angle swept out by \mathbf{B}_{new} is a factor of 50 narrower in width for a $5 \mu\text{s}$ wide pulse than it is for \mathbf{B}_0 . At $12 \mu\text{s}$ the difference is a still significant $10\times$ narrower when using the second order terms. This corresponds to a reduction in polarization uncertainty due to $10 \mu\text{m}$ positional variations by a factor of 100 for $12 \mu\text{s}$ wide pulse and the uncertainty is made negligible for $5 \mu\text{s}$ wide pulses.

A comparison with the current bias field is shown in Fig. 5.2. The varying magnitude of \mathbf{B}_{new} limits its usefulness in precisely controlling the optical polarization, but through the use of an arbitrary waveform generator it will be possible to leave the magnitude constant in time while varying only the angular velocity.

The specific changes to the current setup involving any of the possible solutions to the various problems mentioned above as well as any others that have not come up here need to be carefully considered as there is an interplay between the various experimental considerations. Timing and how it relates to the bias field is certainly the largest consideration, and more work is likely needed to extend the models of the full waveguide field and its effect on the polarization before the best path forward can be chosen. It seems likely though that none of the current limitations in the design are insurmountable.

5.3 Higher-lying tune-out wavelengths

This first measurement of a vector tune-out wavelength shows this general technique has promise in accessing difficult to estimate dipole matrix elements, but that more work is certainly needed to impact the likes of the atomic parity violation analysis. Beyond incrementally improving the experimental design of the current setup, it will be necessary to measure higher-lying tune-out wavelengths to further separate and drive down the uncertainties of the various contributions. I will now highlight the work that is to come.

A_{th} and B_{th} from Chapter 4 are calculated at a fixed wavelength, that of the scalar tune-out wavelength near 790 nm. While this is a reasonable approximation for the dynamics near the lowest-lying tune-out wavelengths, there is more to be gained by considering the frequency dependence of the individual terms. The discretely calculated terms are straightforward to consider. The transition energies are well-known through conventional spectroscopy, and the matrix elements are either calculable or accessible through subsequent tune-out wavelength measurements.

We need tune-out wavelength measurements at multiple wavelengths to separate the tail and core contributions specifically. A recent measurement of α_c by Ref. [27] has driven down uncertainty on that term by an order of magnitude, leaving the core-valence correction the other significant contribution to the total uncertainty. Since it comes in at the same level as the tail contributions, it will need to be dealt with. Fortunately, the core and tail contributions have different

frequency dependences, and we will be able to extract the tail contributions $|t_{1/2}|^2$ and $|t_{3/2}|^2$ by exploiting the differing frequency dependences through measurements of several higher-lying tune-out wavelengths. The frequency dependence of core components goes as $\omega_{\text{core}}/(\omega_{\text{core}}^2 - \omega^2)$, where ω_{core} is the frequency of the lowest core excitation. This occurs in ^{87}Rb near $\lambda_{\text{core}} = 94$ nm. The frequency dependence of tail components has a similar form $\omega_{\text{ion}}/(\omega_{\text{ion}}^2 - \omega^2)$ but with ω_{ion} being the valence electron ionization frequency which occurs at $\lambda_{\text{ion}} = 297.8$ nm. These scale differently enough that a measurement near 420 nm allows their separation.

Doing a global fit over several tune-out wavelengths near different states and with different polarization using the tails, core components, and discrete matrix elements as fit parameters yields a more effective result than what is achievable through the singular scalar and vector tune-out wavelength measurements presented here. In Ref. [28], we generated synthetic data using the best current theoretical and experimental values and used our previous experimental uncertainty of 32 fm to estimate future performance. The results showed that additional measurements near the $6P$ states would allow measurement uncertainties of the various contributions to be reduced by as much as an order of magnitude. The tails for example currently have 100% uncertainty, so a reduction to 10% would go a long way in assisting the APV analysis.

While the experimental uncertainty of the data in this thesis is higher by a factor of 20 than our previous scalar tune-out wavelength measurement, I have shown several improvements to the current design informed by the lessons learned

Contribution	$\alpha^{(0)}$ (421.08 nm)	$\alpha^{(0)}$ (423.03 nm)
$5P_{1/2}$	-40.386	-40.910
$6P_{1/2}$	-113.875	50.423
$7P_{1/2}$	0.128	0.125
$8P_{1/2}$	0.024	0.024
$9P_{1/2}$	0.008	0.008
$10P_{1/2}$	0.004	0.004
$11P_{1/2}$	0.002	0.002
$12P_{1/2}$	0.001	0.001
$5P_{3/2}$	-83.181	-84.276
$6P_{3/2}$	228.035	65.371
$7P_{3/2}$	0.391	0.382
$8P_{3/2}$	0.082	0.081
$9P_{3/2}$	0.031	0.030
$10P_{3/2}$	0.015	0.015
$11P_{3/2}$	0.008	0.008
$12P_{3/2}$	0.005	0.005
Other	8.709(93)	8.709(93)
Total	0.001	0.002

TABLE 5.1: Shown here are the scalar polarizability components for the $6P$ scalar tune-out wavelength measurements.

through the pulsed rf spectroscopic measurements and measurements of the polarization purity. When these improvements are implemented, we should see the experimental precision match and possibly exceed that of the scalar result.

There has already been work on tune-out wavelength measurements near higher-lying states. The scalar tune-out wavelengths near 420 nm have been measured before. Herold et al. [34] were able to achieve uncertainties of a few pm with measurements of 421.075(2) nm and 423.018(7) nm for the two tune-out wavelengths. These tune-out wavelength measurements give the ratio of the higher-lying $6P$ matrix elements to $d_{5P_{1/2}}$ much in the same way the 790 nm scalar tune-out wavelength. They were able to improve upon the $6P$ dipole matrix elements with $d_{6P_{1/2}} = 0.3235(9)$ au and $d_{6P_{3/2}} = 0.5230(8)$ au, a factor of 10 better

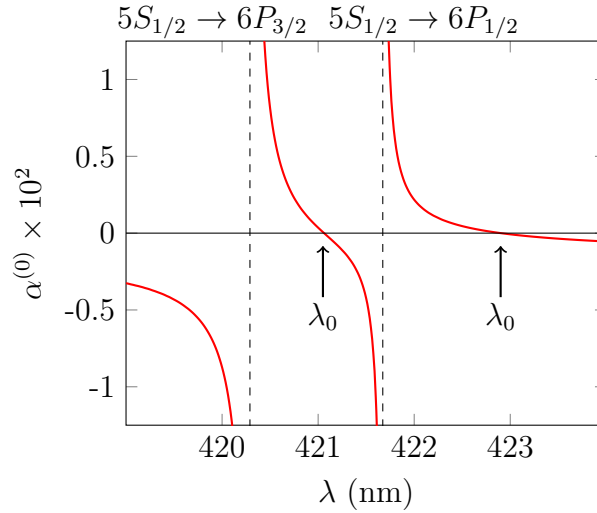


FIGURE 5.3: The scalar polarizability near the $6P$ transitions. There are two nearby tune-out wavelengths due to individual terms cancelling between the $5S_{1/2}$ to $5P_{3/2}$ and $6P_{1/2}$ transitions and again between the $5S_{1/2}$ to $6P_{1/2}$ and $6P_{3/2}$ transitions.

than the best theoretical values [12]. Our apparatus will likely be able to improve further upon this.

One final consideration for the $6P$ measurements is the need to take into account atom loss as we are much nearer to resonance than in the $5P$ measurements.

The scattering rate is expressed as

$$R_s = \frac{\Gamma}{2} \left(\frac{\frac{I}{I_{sat}}}{1 + 4 \left(\frac{\Delta}{\Gamma}\right)^2 + \frac{I}{I_{sat}}} \right), \quad (5.12)$$

where I is the peak intensity given by

$$I = \frac{2P}{\pi w_0^2}, \quad (5.13)$$

Γ is the natural linewidth, I_{sat} is the saturation intensity, and Δ is the detuning.

For a beam waist of $w_0 = 30 \mu\text{m}$. The saturation intensities for the $6P_{1/2}$ and

$6P_{3/2}$ states are 6.3 mW/cm^2 and 3 mW/cm^2 respectively. Using a beam waist of $30 \text{ }\mu\text{m}$ and the $6P_{3/2}$ saturation intensity, we find that approximately 15% of the atoms will be scattered when exposed to a 300 mW Stark beam for 10 ms. There will be a manageable reduction in the interferometer signal, though not large enough to limit the future tune-out wavelength measurements. We therefore find it likely that we can provide useful experimental measurements of higher-lying dipole matrix elements, the various core contributions, and the sum to infinity tails.

Appendix A

Laser system

Previous iterations of the general BEC infrastructure have been described in several theses [5–7]. In those they used an MBR Ti:Sa pumped with a 10 W Coherent Verdi to do laser cooling and trapping, atom manipulation, and imaging. Other lasers at use at various times have included several iterations of homebuilt repump diode lasers, homebuilt and commercial (Toptica DL 100) laser diodes for atom interferometry, and amplified diode lasers for further atomic manipulation.

Due to the frequency sensitivity of tune-out wavelength measurements and requirement of relatively high tuneability as is evident from the body of this work, we decided that the Ti:Sa would be much better suited as the Stark laser. We replaced the Ti:Sa as the main laser in the experiment with a novel amplified diode system described in Section 2.1. This switch had an additional benefit of helping reduce the overall complexity of the laser systems. This appendix goes over the details of this new setup.

A.1 New MOT setup

During the scalar tune-out measurement, we determined that the Ti:SA would be an ideal Stark laser in the experiment with its improved stability and tunability over the diode laser used then [8]. In that experiment, it was necessary to include a narrow bandwidth notch filter (0.25 nm) in the Stark beam path to eliminate unwanted broadband background light present in the beam. The Ti:Sa removes the need for this filter and can also more easily be used in future tune-out measurements near higher-lying P states through frequency doubling or tripling. The Verdi pump laser at the time was also showing its age and suffering significant power degradation. Its inevitable replacement and the rebuild of the optics setup would serve as a convenient time to upgrade the Stark laser.

We had hoped to get through the vector polarizability measurements before making the switch, but in the run up to the vector polarizability experiment, we saw the Verdi pump laser degrade enough to force an early switch of primary MOT laser system. We were lucky enough to obtain a Toptica DL Pro for free through a government surplus program to use as the seed laser for the tapered amplifier (TA). We used a refurbished and modified Sacher Lasertechnik system as the TA. Also on hand from a previous student's dissertation work [74] was a fiber coupled electro-optic modulator (EO) from EOPSPACE. The custom package had low (less than 2dB) insertion loss, with no internal termination, and a low $V_\pi = 1.7$ V. The fiber EO allowed for the removal of our repump laser by using sidebands at the repump detuning of roughly 6.8 GHz. This reduced the total

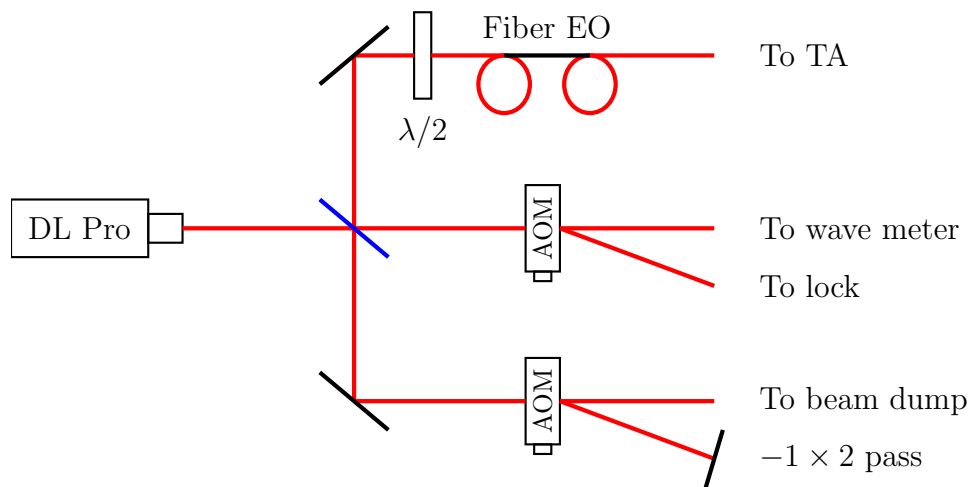


FIGURE A.1: MOT laser AOM configuration. After the TA are additional AOMs for switching the MOT, optical pumping, and imaging.

number of lasers needed in the experiment and beneficially, the number of lasers locked to an atomic transition. More information on how we drive the EO is in the next section.

The acousto-optic modulator (AOM) setup for the primary MOT laser is simplified somewhat from before as well. The double pass AOM used to vary the laser frequency between the MOT, CMOT, and imaging frequencies is now before the TA, so we have significant overhead on optical power. This allows the removal of several pickoff mirrors in very close proximity which are replaced with a beamsplitter. This makes initial alignment and optimization of the double pass much easier. The new AOM setup can be seen in Fig. A.1.

While rebuilding the laser systems we also took the opportunity to move the lasers, with the exception of the TA, to a separate optics table for better isolation from the experiment. The MOT, Stark, and Bragg lasers are all fiber-coupled through polarization maintaining (PM) optical fibers to reduce polarization noise

at their outputs.

A.1.1 Driving the EOM

The use of an electro-optic modulator (EO) to introduce sidebands to the seed laser prior to amplification simplifies the MOT laser system significantly. In order to have adequate repump light during all stages of our experiment we previously needed a combination of a free-space cavity EO generating the necessary sidebands in the two vertical MOT beams and also a locked laser diode. The free-space EO supplemented the repump laser during regular MOT operation. When transitioning to the CMOT, the repump laser was blocked and just light from the EO was used to repopulate the cycling transition. During optical pumping, where the carrier light was tuned far outside of the bandwidth of the free-space EO, the repump laser was unblocked once more. These stages are all now done with just the fiber EO.

Switching of the amplitude and frequency of the rf source driving the EO is handled through solid state analog switches with all outputs tied to a voltage controlled oscillator and adjustable attenuator. Selection is done through a digital demultiplexer which is fed by two digital outputs from our Adwin breakout panel. The four available states are MOT, CMOT, Pumping, and an Off state which is low output / far detuned. There is an additional switch on the control panel for completely shutting down the output as the dynamic range of the adjustable attenuator is only 20 dB. This switch allows manipulation of the output SMA

Stage	Digital 1	Digital 2	Power (mW)	Frequency (MHz)
MOT	High	Low	0.7	6587
cMOT	High	High	1.0	6519
Pumping	Low	High	2.6	6840
Off	Low	Low	0.1	6260

TABLE A.1: EO logic settings. Two Adwin digital outputs are fed into a digital demultiplexer to allow selection of the specific configuration needed for the given cooling stage. Listed are the rf powers and sideband frequencies relative to the carrier.

cable without risk of damaging the drive circuitry. Additionally, to further protect the amplifier, there is a 1 dB attenuator directly connected to the EO such that it more mimics a typical 50Ω load. The fiber EO is an unterminated, capacitive load, so this is done to prevent excessive back reflections damaging the amplifier.

A.2 Stark setup

Key to the vector tune-out wavelength measurements is that the extinction ratio between when the light is pulsed on and when it is off must be better than 10^6 to avoid significant errors in the optical polarization. AOMs typically have an extinction ratio of just 10^3 , so we use two in series. As seen in Fig. A.2 both use the -1 order. This 160 MHz shift must be accounted for in the tune-out wavelength analysis.

For the polarization purity measurements outlined in Chapter 3, it is locked to the D_1 line. Because the atoms are suspended in a magnetic trap, we must account for the ~ 20 MHz Zeeman shift and undo most of the 160 MHz shift from the switching AOMs. We do this by including a double-pass AOM before the lock,

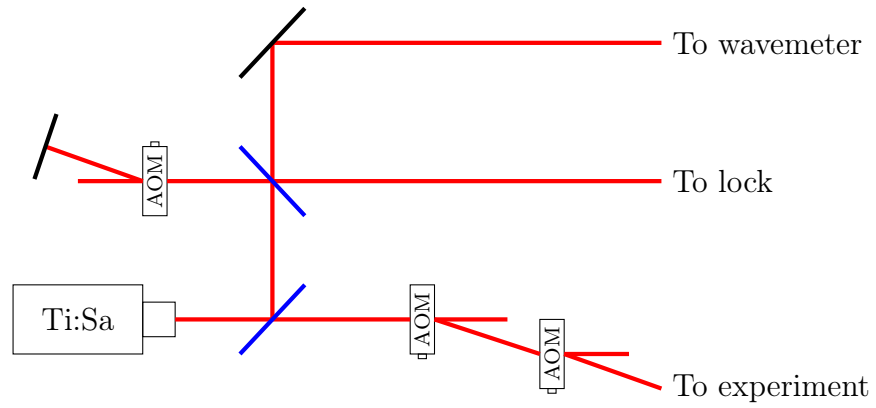


FIGURE A.2: Stark laser AOM configuration.

which allows changing the lock set point without altering the beam alignment. This allows us to be resonant with the m -sublevel of choice. We typically have it resonant with the $5P_{1/2}|2, 2\rangle$ state during the polarization purity measurements.

AOM	Frequency (MHz)	Order	Frequency Modulation (V)
Main 2×	41.95	-1 × 2	MOT: 0.016
Main 2× pass	55.82	-1 × 2	cMOT: 0.75
Main 2× pass	35.98	-1 × 2	Pump: -0.3
Main 2× pass	45.05	-1 × 2	Probe: 0.18
MOT lock	31.89	+1	-
Pump	80	-2	-
Probe	119.16	+1	-
MOT	90.72	-1	-
Stark lock 2× pass	66.69	-1 × 2	2.50
Stark 1	80	-1	-
Stark 2	80	-1	-
Bragg	80	+1	-

TABLE A.2: Here are the AOM values for the experiment. The main double pass, inline with the TA has a tuning rate of 37.8 MHz/V total. The voltages listed for it are controlled via Adwin analog output 1. The Stark lock double pass is set by a dc power supply.

Appendix B

Twitch routines

The following sections describe the settings of many of the experimental parameters for the various measurements involved in measuring a tune-out wavelength. Twitch is our homebuilt compiler for the Adwin realtime computer which controls much of the equipment. The leftmost column is for the duration in ms the particular line is to run or if text is present, the given routine. These routines include other Twitch files run as subroutines, Adwin input triggers such as “sync26” which has Adwin wait for a signal before continuing, and routines run on the lab computer via a separate program called Commander. Examples of the latter include our camera setup scripts which begin each main Twitch file, and various rs232 or GPIB commands to reprogram equipment *in situ* such as the radio-frequency function generator used during rf evaporation. These scripts are contained in a text file titled “evap.txt” which Commander references, and I have included several relevant commands below. The general structure of those commands is the GPIB

channel, the variable to set, and its value. The next columns in the Twitch files are for the digital outputs and the eight analog outputs. If parameters are unchanged from one line of a Twitch routine to the next, " can be used on the later lines instead of repeating the parameter values.

Thanks to improvements by Seth Berl, we now have the ability to comment out lines in Twitch routines. This makes maintaining the correct timing sequences across the various measurements straightforward. The prime example where this comes into play is in the alignment of the Stark beam on the atoms 5 ms after they are split. We need to ensure that the atoms' position is measured at the same point in time as when the beam will be turned on during the tune-out wavelength measurements. All Twitch routines listed here are the same "interferometer.twh" routine with the relevant lines uncommented. This removes the need to maintain and update multiple twitch files for the various measurements

Additional notes are included detailing other manually controlled parameters for the given measurement. These include attenuations set through wave plate adjustments and switching between imaging systems. This appendix ends with a complete list of the experimental parameters and their Adwin and Commander counterparts.

B.1 Full BEC experiments

B.1.1 Tune-out wavelength interferometer

This is the full tune-out wavelength measurement. The atoms and beam are aligned with one another and the interferometer is optimized prior to running this routine. The parameters to change here are in the rs232 L command, where the pulse delay sets the effective optical polarization and the output voltage of the pulse is used to control the intensity of the Stark beam through amplitude modulation of the Stark AOMs. We typically vary the AOMs from full on to off in 5 to 10% increments in a randomized order. In general the voltages used depend on the particular AOM driver and have a nonlinear response. Here they span roughly 0.6 to 1 V.


```
L   generic      6
10  ARM:SOUR     EXT
10  PULS:DEL1    <#>us
10  PULS:WIDT1  5us
10  VOLT1:HIGH  <#>V
10  CHAN:MATH   OFF
10  OUTP1:STAT  ON
```

Notes: Digital J manual override ON (side imaging) - No attenuation in Stark
AOM rf outputs - Beam attenuation HWP at 100° (maximized)

B.1.2 Atom position

This routine is to find the atoms' position in order to align the Stark beam with them. The atoms are imaged 5 ms after they are split. The camera trigger digital "u" is added before splitting as the Apogee camera used in the vertical imaging setup is significantly slower than the PI camera used in the side imaging setup.

Time (ms)	Digitals	V ₁	V ₂	V ₃	V ₄	V ₅	V ₆	V ₇	V ₈
/ Routine									
setupVertCam									
cmot_pump									
loadtrap									
movetrap									
evaporate									
loadguide_ac									
rs232 L									
sync26									
180.04	afv	"	"	"	"	"	"	"	"
270	afvu	"	"	"	"	"	"	"	"
5	afvoe	"	"	"	"	"	0	0	"
Bragg_Split1									
4	fs	0.18	"	"	"	"	"	"	"
0.45	fs	"	-5	0	-5	-5	0	0	-5
probe_apogee									
cleanup									
mot									

```

L generic 6
10 ARM:SOUR EXT
10 PULS:DEL1 <#>us
10 PULS:WIDT1 150ns
10 VOLT1:HIGH 0.6V
10 CHAN:MATH OFF
10 OUTP1:STAT ON

```

Notes: Digital J manual override OFF (vertical imaging) - 16 dB attenuation (6 dB and 10 dB) in Stark AOM rf outputs - Beam attenuation HWP at 142° (minimized)

B.1.3 Beam position

The Stark beam is imaged by running the experiment in the same way we did to find the atoms' position but with a modified probing routine to turn the Stark beam briefly on. Because it is tightly focused in the imaging plane, it is necessary to significantly attenuate the beam.

Time (ms)	Digitals	V_1	V_2	V_3	V_4	V_5	V_6	V_7	V_8
/ Routine									
setupVertCam									
cmot_pump									
loadtrap									
movetrap									
evaporate									
loadguide_ac									
rs232 L									
sync26									
180.04	afv	"	"	"	"	"	"	"	"
270	afvu	"	"	"	"	"	"	"	"
5	afvoe	"	"	"	"	"	0	0	"
probe_stark									
cleanup									
mot									

```

L generic 6
10 ARM:SCOUR EXT
10 PULS:DEL1 <#>us
10 PULS:WIDT1 150us
10 VOLT1:HIGH <#>V
10 CHAN:MATH OFF
10 OUTP1:STAT ON

```

Notes: Digital J manual override OFF (vertical imaging) - 16 dB attenuation (6 dB and 10 dB) in Stark AOM rf outputs - Beam attenuation HWP at 142° (minimized)

B.1.4 Pulsed radio-frequency spectroscopy

This routine is used to measure the time dependence of the TOP trap bias field magnitude. This process is automated. A list of rf frequencies and delay times in a csv file are used to set the corresponding “evap.txt” parameters. Seven different delay times with around 10 frequencies are typically necessary to fit the field components with the required precision. As usual the experimental timings are identical to those used in the tune-out wavelength measurement with the rf turned on during the 20 ms period the Stark beam would be on.

Time (ms)	Digitals	V ₁	V ₂	V ₃	V ₄	V ₅	V ₆	V ₇	V ₈
/ Routine									
setupKinCam									
cmot_pump									
loadtrap									
movetrap									
evaporate									
loadguide_ac									
rs232 H									
rs232 P									
sync26									
180.04	afv	"	"	"	"	"	"	"	"
270	afv	"	"	"	"	"	"	"	"
5	afvoe	"	"	"	"	"	0	0	"
20	afvoemg	"	"	"	"	"	"	0	"
15	afv	"	"	"	"	"	0	0	"
4	fs	0.18	"	"	"	"	"	"	"
0.45	fs	"	-5	0	-5	-5	0	0	-5
probe_kin									
cleanup									
mot									

```

H  generic      3
19 POW:AMP      -4 DB
19 FREQ:CW      ⟨#⟩MHZ
19 OUTP:STAT    ON

```

```

P  generic      6
10 ARM:SOUR     EXT
10 PULS:DEL2    ⟨#⟩us
10 PULS:WIDT2   7.5us
10 VOLT2:HIGH   10V
10 CHAN:MATH    OFF
10 OUTP2:STAT   ON

```

Notes: Digital J manual override ON (side imaging)

B.1.5 Polarization measurement

The polarization measurement routine differs slightly from the others. Due to the longer necessary interaction time, we do not split the atoms here. Instead their position is measured with the atoms at rest, and the Stark beam is aligned to that location. This is a difference in alignment of roughly $125 \mu\text{m}$. We again vary the pulse output amplitude being fed into the Stark AOM amplitude modulation inputs and observe the first minimum in the number of scattered atoms to calibrate the polarization purity.

This routine is also used when optimizing timing, alignment, and wave plate angles when setting the polarization.

Time (ms)	Digitals	V ₁	V ₂	V ₃	V ₄	V ₅	V ₆	V ₇	V ₈
/ Routine									
setupKinCam									
cmot_pump									
loadtrap									
movetrap									
evaporate									
loadguide_ac									
rs232 L									
sync26									
180.04	afv	"	"	"	"	"	"	"	"
270	afv	"	"	"	"	"	"	"	"
5	afvoe	"	"	"	"	"	0	0	"
300	afvoemg	"	"	"	"	"	"	"	"
15	afv	"	"	"	"	"	"	"	"
4	fs	0.18	"	"	"	"	"	"	"
0.45	fs	"	-5	0	-5	-5	0	0	-5
probe_kin									
cleanup									
mot									

```

L generic 6
10 ARM:SOUR EXT
10 PULS:DEL1 <#>us
10 PULS:WIDT1 150us
10 VOLT1:HIGH <#>V
10 CHAN:MATH OFF
10 OUTP1:STAT ON

```

Notes: Digital J manual override ON (side imaging) - 16 dB attenuation (6 dB and 10 dB) in Stark AOM rf outputs - Beam attenuation HWP at 130°

B.2 ADWIN outputs, Subroutines, and Evap.txt

B.2.1 ADWIN outputs

Digitals

- a MOT AOM
- b Pump AOM
- c
- d Probe AOM
- e Stark Shutter
- f Waveguide preamplifier
- g General trigger
- h
- i
- j Vertical/side imaging Low: Vertical High: Side
- k Track Low: Science High: MOT
- l Pumping bias coil
- m Pulse generator trigger
- n
- o Bragg shutter
- p DC quadrupole
- q
- r
- s TA main shutter
- t
- u Camera trigger
- v EOM driver digital
- w EOM driver digital
- x Commander

Analogs

1	TA double pass frequency	31 MHz/V
2	Waveguide bias amplitude	-5 V to +5 V
3	DC quadrupole amplitude	0 V to +10 V
4	Waveguide quad amplitude	-5 V to +5 V
5	Unused	Broken
6	Bragg frequency	
7	Bragg amplitude	
8	AC y coil amplitude	-5 V to +5 V

Digital inputs

24	RS232	Commander
25	60 Hz sync	
26	Waveguide quad sync	

B.2.2 Twitch subroutines**cmot_pump.twh**

Time (ms)	Digitals	V_1	V_2	V_3	V_4	V_5	V_6	V_7	V_8
/ Routine									
1	pksav	0.016	-5	0.22	-5	-5	0	0	-5
10r	pksavw	0.75	"	"	"	"	"	"	"
5	ksavw	"	"	0	"	"	"	"	"
0.3	klsw	"	"	"	"	"	"	"	"
0.35	"	-0.3	"	0	"	"	"	"	"
0.5	klswb	"	"	"	"	"	"	"	"
0.5	klsw	"	"	"	"	"	"	"	"

loadtrap.twh

Time (ms)	Digitals	V_1	V_2	V_3	V_4	V_5	V_6	V_7	V_8
/ Routine									
0.1	pkl	-0.1	-5	0	-5	-5	0	0	-5
15r	"	"	"	3	"	"	"	"	"
50	pakl	"	"	"	"	"	"	"	"
100r	"	"	"	9.9	"	"	"	"	"

probe_stark.twh

Time (ms)	Digitals	V ₁	V ₂	V ₃	V ₄	V ₅	V ₆	V ₇	V ₈
/ Routine									
5	fe	0.21	"	"	"	"	"	0	"
4	fse	"	"	"	"	"	"	"	"
0.5	"	"	-5	0	-5	-5	0	0	-5
0.5	se	"	"	"	"	"	"	"	"
2	sem	"	"	"	"	"	"	"	"
195	av	"	"	"	"	"	"	"	"
5	s	"	"	"	"	"	"	"	"
0.05	"	"	"	"	"	"	"	"	"
100		"	"	"	"	"	"	"	"

cleanup.twh

Time (ms)	Digitals	V ₁	V ₂	V ₃	V ₄	V ₅	V ₆	V ₇	V ₈
/ Routine									
50	"	"	-5	0	-5	-5	0	0	-5
rs232 o									
50	"	"	"	"	"	"	"	"	"
rs232 0									
2000	pksav	0.016	-5	0.22	-5	-5	0	0	-2
2000	ksav	"	"	"	"	"	"	"	"
rs232 Z									

mot.twh

Time (ms)	Digitals	V ₁	V ₂	V ₃	V ₄	V ₅	V ₆	V ₇	V ₈
/ Routine									
60000	pksav	0.016	-5	0.22	-5	-5	0	0	-2

B.2.3 Evap.txt

GPIB devices

10	Pulse generator	HP 8110A
11	Bias 1 function generator	Agilent 33120A
12	Bias 2 function generator	Agilent 33120A
13	Linear quad function generator	Agilent 33120A
19	RF signal generator	Agilent 8648D

Evap.txt

```
% Instructions:
%
% evaporation commands have
% <key> rf <nlines>
% <startf> <stopf> <time_const> <power> <bottom_freq>
%
% generic GPIB commands have
% <key> generic <nlines>
% <device address> <command to send>
%

% Imaging setup

b system 1
  c:/Experiment_Software/Princeton_Instruments/PI_Background.bat

c system 1
  c:/Experiment_Software/Apogee/Apogee_Background.bat

i system 1
  c:/Experiment_Software/Princeton_Instruments/PI_Kinetics.bat

e system 1
  c:/Experiment_Software/Apogee/Apogee_Kinetics.bat

% rf Function Generator
```

% Evaporation

f rf 1

8.0 0.045 2.75 0 2.075

% Evaporation

h rf 3

90 30 6 3.5 0.0

30 15 3 3.5 0.0

15 12 1.5 3.5 0.0

% RF spectroscopy

H generic 3

19 POW:AMPL -4 DB

19 FREQ:CW 14.5 MHZ

19 OUTP:STAT ON

o generic 1

19 OUTP:STAT OFF

% Function Generators

A generic 1

11 PHASE:ADJ 0 DEG

B generic 1

12 PHASE:ADJ 90 DEG

C generic 1

13 PHASE:ADJ 315 DEG

% Pulse Generator

% Stark AOMs - Output 1

L generic 6

10 ARM:SOUR EXT

10 PULS:DEL1 50.68us

10 PULS:WIDT1 150ns

10 VOLT1:HIGH 0.95V

10 CHAN:MATH OFF

10 OUTP1:STAT ON

% Evaporation - Output 2

N generic 7

```
10 ARM:SOUR IMM
10 PULS:PER2 1ms
10 PULS:DEL2 0ms
10 PULS:WIDT2 995us
10 VOLT2:HIGH 10V
10 CHAN:MATH OFF
10 OUTP2:STAT ON
```

% RF spectroscopy - Output 2

P generic 6

```
10 ARM:SOUR EXT
10 PULS:DEL2 15us
10 PULS:WIDT2 7.5us
10 VOLT2:HIGH 10V
10 CHAN:MATH OFF
10 OUTP2:STAT ON
```

O generic 3

```
10 OUTP1:STAT OFF
10 OUTP2:STAT OFF
10 CHAN:MATH OFF
```

Bibliography

- [1] A. Ashkin, J. M. Dziedzic, J. E. Bjorkholm, and S. Chu. Observation of a single-beam gradient force optical trap for dielectric particles. *Optics Letters*, 11(5):288–290, May 1986.
- [2] I. E. Dzyaloshinskii, E. M. Lifshitz, and Lev P. Pitaevskii. Reviews of Topical Problems: General Theory of Van Der Waals’ Forces. *Soviet Physics Uspekhi*, 4(2):153–176, February 1961.
- [3] M. S. Safronova, Carl J. Williams, and Charles W. Clark. Optimizing the fast rydberg quantum gate. *Phys. Rev. A*, 67:040303, Apr 2003.
- [4] Y.B. Zeldovich. Parity nonconservation in electron scattering and in other effects in the first order of the weak interaction coupling constant. *Zh. Eksp. Teor. Fiz.*, 36, 1959.
- [5] Jessica Reeves. *An Atom Waveguide For Interferometry with a Bose-Einstein Condensate of ^{87}Rb* . PhD thesis, University of Virginia, 2006.
- [6] John Burke. *Improvements and applications of a guided wave Bose-Einstein condensate interferometer*. PhD thesis, University of Virginia, 2010.
- [7] Robert Leonard. *High precision measurement of the D-line tune-out wavelength in ^{87}Rb using a Bose-Einstein condensate interferometer*. PhD thesis, University of Virginia, 2015.
- [8] R. H. Leonard, A. J. Fallon, C. A. Sackett, and M. S. Safronova. High-precision measurements of the ^{87}Rb D-line tune-out wavelength. *Phys. Rev. A*, 92:052501, Nov 2015.
- [9] U. Volz and H. Schmoranze. Precision lifetime measurements on alkali atoms and on helium by beam–gas–laser spectroscopy. *Physica Scripta.*, T65:48–56, 1996.
- [10] J E. Simsarian, LA Orozco, G Sprouse, and W Z. Zhao. Lifetime measurements of the 7P levels of atomic francium. *Physical Review A*, 57, 04 1998.
- [11] R. F. Gutterres, C. Amiot, A. Fioretti, et al. Determination of the ^{87}Rb 5P state dipole matrix element and radiative lifetime from the photoassociation spectroscopy of the Rb_2 $0_g^-(P_{3/2})$ long-range state. *Phys. Rev. A*, 66:024502, Aug 2002.
- [12] Bindiya Arora, M. S. Safronova, and Charles W. Clark. Tune-out wavelengths of alkali-metal atoms and their applications. *Phys. Rev. A*, 84:043401, Oct 2011.

- [13] S. G. Porsev, K. Beloy, and A. Derevianko. Precision determination of weak charge of ^{133}Cs from atomic parity violation. *Phys. Rev. D*, 82:036008, Aug 2010.
- [14] V. A. Dzuba, J. C. Berengut, V. V. Flambaum, and B. Roberts. Revisiting parity nonconservation in cesium. *Phys. Rev. Lett.*, 109:203003, Nov 2012.
- [15] George Toh, Amy Damitz, Carol E. Tanner, W. R. Johnson, and D. S. Elliott. Determination of the scalar and vector polarizabilities of the cesium $6s^2S_{1/2} \rightarrow 7s^2S_{1/2}$ transition and implications for atomic parity nonconservation. *Phys. Rev. Lett.*, 123:073002, Aug 2019.
- [16] Sheldon L. Glashow. Partial-symmetries of weak interactions. *Nuclear Physics*, 22(4):579 – 588, 1961.
- [17] C. S. Wood, S. C. Bennett, D. Cho, et al. Measurement of parity nonconservation and an anapole moment in cesium. *Science*, 275(5307):1759–1763, 1997.
- [18] P. L. Anthony, R. G. Arnold, C. Arroyo, et al. Precision measurement of the weak mixing angle in m oller scattering. *Phys. Rev. Lett.*, 95:081601, Aug 2005.
- [19] D. Androi c, D. S. Armstrong, A. Asaturyan, et al. Precision measurement of the weak charge of the proton. *Nature*, 557(7704):207–211, 2018.
- [20] M. Tanabashi, K. Hagiwara, K. Hikasa, et al. Review of particle physics. *Phys. Rev. D*, 98:030001, Aug 2018.
- [21] J. Stark. Beobachtungen  ber den effekt des elektrischen feldes auf spektrallinien. i. quereffekt. *Annalen der Physik*, 348(7):965–982, 1914.
- [22] William F. Holmgren, Melissa C. Revelle, Vincent P.A. Lonij, and Alexander D. Cronin. Absolute and ratio measurements of the polarizability of Na, K, and Rb with an atom interferometer. May 2010.
- [23] Maxwell D. Gregoire, Ivan Hromada, William F. Holmgren, Raisa Trubko, and Alexander D. Cronin. Measurements of the ground-state polarizabilities of Cs, Rb, and K using atom interferometry. *Phys. Rev. A*, 92:052513, Nov 2015.
- [24] B. Deissler, K. J. Hughes, J. H. T. Burke, and C. A. Sackett. Measurement of the ac stark shift with a guided matter-wave interferometer. *Phys. Rev. A*, 77:031604, Mar 2008.
- [25] A. Kramida, Yu. Ralchenko, J. Reader, and and NIST ASD Team. NIST Atomic Spectra Database (ver. 5.7.1), [Online]. Available: <https://physics.nist.gov/asd> [2019, December 2]. National Institute of Standards and Technology, Gaithersburg, MD., 2019.
- [26] W.R. Johnson, Dietmar Kolb, and K.-N. Huang. Electric-dipole, quadrupole, and magnetic-dipole susceptibilities and shielding factors for closed-shell ions of the He, Ne, Ar, Ni (Cu+), Kr, Pb, and Xe isoelectronic sequences. *Atomic Data and Nuclear Data Tables*, 28(2):333 – 340, 1983.
- [27] S. J. Berl, C. A. Sackett, T. F. Gallagher, and J. Nunkaew. Core polarizability of rubidium using spectroscopy of the ng to nh, ni rydberg transitions. 2020.

- [28] Adam Fallon and Charles Sackett. Obtaining atomic matrix elements from vector tune-out wavelengths using atom interferometry. *Atoms*, 4(2), 2016.
- [29] P. Schneeweiss F. L. Kien and A. Rauschenbeutel. *Eur. Phys. J. D*, 67(92), 2013.
- [30] P. S. Jessen I. H. Deutsch. Quantum control and measurement of atomic spins in polarization spectroscopy. *Optics Communications*, 283:681–694, 2010.
- [31] Daniel A. Steck. Rubidium 87 D line data. revision 2.2.1, 21 November 2019.
- [32] Felix Schmidt, Daniel Mayer, Michael Hohmann, et al. Precision measurement of the ^{87}Rb tune-out wavelength in the hyperfine ground state $F = 1$ at 790 nm. *Phys. Rev. A*, 93:022507, Feb 2016.
- [33] William F. Holmgren, Raisa Trubko, Ivan Hromada, and Alexander D. Cronin. Measurement of a wavelength of light for which the energy shift for an atom vanishes. *Phys. Rev. Lett.*, 109:243004, Dec 2012.
- [34] C. D. Herold, V. D. Vaidya, X. Li, et al. Precision measurement of transition matrix elements via light shift cancellation. *Phys. Rev. Lett.*, 109:243003, Dec 2012.
- [35] M. S. Safronova and U. I. Safronova. Critically evaluated theoretical energies, lifetimes, hyperfine constants, and multipole polarizabilities in ^{87}Rb . *Phys. Rev. A*, 83:052508, May 2011.
- [36] L. J. LeBlanc and J. H. Thywissen. Species-specific optical lattices. *Phys. Rev. A*, 75:053612, May 2007.
- [37] J. Catani, G. Barontini, G. Lamporesi, et al. Entropy exchange in a mixture of ultracold atoms. *Phys. Rev. Lett.*, 103:140401, Sep 2009.
- [38] G. Lamporesi, J. Catani, G. Barontini, et al. Scattering in mixed dimensions with ultracold gases. *Phys. Rev. Lett.*, 104:153202, Apr 2010.
- [39] Philipp Schneeweiss, Fam Le Kien, and Arno Rauschenbeutel. Nanofiber-based atom trap created by combining fictitious and real magnetic fields. *New Journal of Physics*, 16(1):013014, jan 2014.
- [40] Raisa Trubko, James Greenberg, Michael T. St. Germaine, et al. Atom interferometer gyroscope with spin-dependent phase shifts induced by light near a tune-out wavelength. *Phys. Rev. Lett.*, 114:140404, Apr 2015.
- [41] William D. Phillips. Nobel lecture: Laser cooling and trapping of neutral atoms. *Rev. Mod. Phys.*, 70:721–741, Jul 1998.
- [42] T.W. Hänsch and A.L. Schawlow. Cooling of gases by laser radiation. *Optics Communications*, 13(1):68 – 69, 1975.
- [43] Christopher C. Davis. *Lasers and Electro-Optics: Fundamentals and Engineering*. 1996.
- [44] V. Bolpasi and W. von Klitzing. Double-pass tapered amplifier diode laser with an output power of 1 W for an injection power of only 200 μW . *Review of Scientific Instruments*, 81(11):113108, 2010.

- [45] V. M. Valenzuela, L. Hernández, and E. Gomez. High power rapidly tunable system for laser cooling. *Review of Scientific Instruments*, 83(1):015111, 2012.
- [46] C. E. Rogers and P. L. Gould. Nanosecond pulse shaping at 780 nm with fiber-based electro-optical modulators and a double-pass tapered amplifier. *Opt. Express*, 24(3):2596–2606, Feb 2016.
- [47] P. D. Lett, W. D. Phillips, S. L. Rolston, et al. Optical molasses. *J. Opt. Soc. Am. B*, 6(11):2084–2107, Nov 1989.
- [48] Alan L. Migdall, John V. Prodan, William D. Phillips, Thomas H. Bergeman, and Harold J. Metcalf. First observation of magnetically trapped neutral atoms. *Phys. Rev. Lett.*, 54:2596–2599, Jun 1985.
- [49] Naoto Masuhara, John M. Doyle, Jon C. Sandberg, et al. Evaporative cooling of spin-polarized atomic hydrogen. *Phys. Rev. Lett.*, 61:935–938, Aug 1988.
- [50] E. Majorana. Atomi orientati in campo magnetico variabile. *Il Nuovo Cimento*, 9:43–50, February 1932.
- [51] J. M. Reeves, O. Garcia, B. Deissler, et al. Time-orbiting potential trap for bose-einstein condensate interferometry. *Phys. Rev. A*, 72:051605, Nov 2005.
- [52] David E. Pritchard. Cooling neutral atoms in a magnetic trap for precision spectroscopy. *Phys. Rev. Lett.*, 51:1336–1339, Oct 1983.
- [53] K. B. Davis, M. O. Mewes, M. R. Andrews, et al. Bose-einstein condensation in a gas of sodium atoms. *Phys. Rev. Lett.*, 75:3969–3973, Nov 1995.
- [54] J. H. T. Burke, B. Deissler, K. J. Hughes, and C. A. Sackett. Confinement effects in a guided-wave atom interferometer with millimeter-scale arm separation. *Phys. Rev. A*, 78:023619, Aug 2008.
- [55] Peter J. Martin, Bruce G. Oldaker, Andrew H. Miklich, and David E. Pritchard. Bragg scattering of atoms from a standing light wave. *Phys. Rev. Lett.*, 60:515–518, Feb 1988.
- [56] K. J. Hughes, B. Deissler, J. H. T. Burke, and C. A. Sackett. High-fidelity manipulation of a bose-einstein condensate using an optical standing wave. *Phys. Rev. A*, 76:035601, Sep 2007.
- [57] M. Lintz J. Guéna and M.-A. Bouchiat. Atomic parity violation: principles, recent results, present motivations. *Mod. Phys. Lett. A*, 20:375–389, 2005.
- [58] T. E. Chupp, P. Fierlinger, M. J. Ramsey-Musolf, and J. T. Singh. Electric dipole moments of atoms, molecules, nuclei, and particles. *Rev. Mod. Phys.*, 91:015001, Jan 2019.
- [59] M. S. Safronova, D. Budker, D. DeMille, et al. Search for new physics with atoms and molecules. *Rev. Mod. Phys.*, 90:025008, Jun 2018.
- [60] S. G. Crane, S. J. Brice, A. Goldschmidt, et al. Parity violation observed in the beta decay of magnetically trapped ^{82}Rb atoms. *Phys. Rev. Lett.*, 86:2967–2970, Apr 2001.

- [61] A S Arnold. Adaptable-radius, time-orbiting magnetic ring trap for Bose-Einstein condensates. *J. Phys. B: At. Mol. Opt. Phys.*, 37:L29, 2004.
- [62] S Gupta, K W Murch, K L Moore, T P Purdy, and D M Stamper-Kurn. Bose-Einstein condensation in a circular waveguide. *Phys. Rev. Lett.*, 95:143201, 2005.
- [63] A. J. Fallon and C. A. Sackett. Precise control of magnetic fields and optical polarization in a time-orbiting potential trap. *Submitted*, 2020.
- [64] Schott Advanced Optics. Stress in optical glass. Technical Report TIE-27, SCHOTT AG, 2019.
- [65] R A Chipman. *Handbook of Optics*, volume I, chapter 15. McGraw-Hill, New York, third edition, 2010.
- [66] Y Takubo, N Takeda, J H Huang, K Muroo, and M Yamamoto. Precise measurement of the extinction ratio of a polarization analyser. *Meas. Sci. Technol.*, 9:20–23, 1998.
- [67] J. M. Bennett. A critical evaluation of rhomb-type quarterwave retarders. *App. Opt.*, 9:2123–, 1970.
- [68] Christopher J Foot. *Atomic physics*. Oxford master series in atomic, optical and laser physics. Oxford University Press, Oxford, 2007.
- [69] Rudolf Grimm, Matthias Weidemüller, and Yurii B. Ovchinnikov. Optical Dipole Traps for Neutral Atoms. *Advances in Atomic Molecular and Optical Physics*, 42:95–170, January 2000.
- [70] Bahaa E A Saleh and Malvin Carl Teich. *Fundamentals of photonics; 2nd ed.* Wiley series in pure and applied optics. Wiley, New York, NY, 2007.
- [71] Thorlabs protected gold coating. Technical report, Thorlabs, Inc.
- [72] Thorlabs protected gold coating (phase). Technical report, Thorlabs, Inc.
- [73] S Bize, Y Sortais, M. S Santos, et al. High-accuracy measurement of the ^{87}Rb ground state hyperfine splitting in an atomic fountain. *Europhysics Letters (EPL)*, 45(5):558–564, mar 1999.
- [74] Eun Oh. *Asymmetric splitting of Bose-Einstein condensate*. PhD thesis, University of Virginia, 2014.